

AD-A049 302

AIR FORCE GEOPHYSICS LAB HANSCOM AFB MASS  
INFRARED FLUORESCENCE OF ELECTRON IRRADIATED CO SUB 2 IN THE PR--ETC(U)  
SEP 77 R E MURPHY, F H COOK, G E CALEDONIA

F/G 7/4

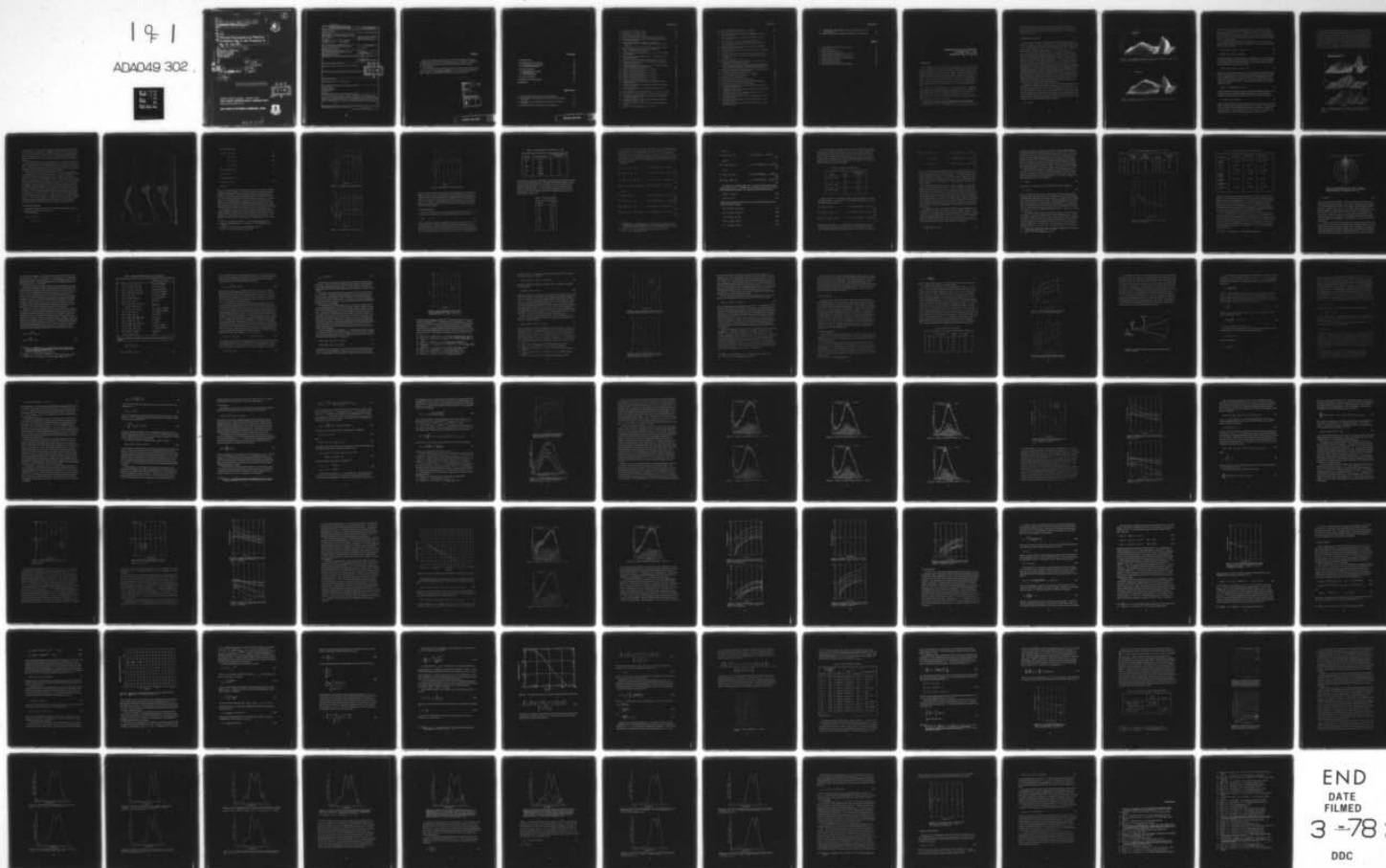
UNCLASSIFIED

AFGL-TR-77-0205

NL

191

ADAD49 302



END  
DATE  
FILMED  
3 -78  
DDC

2

AD A 0 4 9 3 0 2

AFGL-TR-77-0205, AFGL-ERP-609  
ENVIRONMENTAL RESEARCH PAPERS, NO. 609



Infrared Fluorescence of Electron  
Irradiated CO<sub>2</sub> in the Presence of  
N<sub>2</sub>, Ar, and He.

RANDALL E. / MURPHY,  
FLOYD H. / COOK,  
G.E. / CALEDONIA  
B.D. / GREEN

sub

AD No. DDC FILE COPY

15 September 1977

16 2310  
S99QAXH  
17 GH  
I004

61102F

12 96p.

Approved for public release; distribution unlimited.

DDC  
RECEIVED  
FEB 2 1978  
B

OPTICAL PHYSICS DIVISION PROJECT 2310  
AIR FORCE GEOPHYSICS LABORATORY  
HANSCOM AFB, MASSACHUSETTS 01731

AIR FORCE SYSTEMS COMMAND, USAF



1473  
409 578

13

Unclassified

SECURITY CLASSIFICATION OF THIS PAGE (When Data Entered)

REPORT DOCUMENTATION PAGE		READ INSTRUCTIONS BEFORE COMPLETING FORM
1. REPORT NUMBER AFGL-TR-77-0205	2. GOVT ACCESSION NO.	3. REPORT'S CATALOG NUMBER
4. TITLE (and Subtitle) INFRARED FLUORESCENCE OF ELECTRON IRRADIATED CO <sub>2</sub> IN THE PRESENCE OF N <sub>2</sub> , Ar, AND He		5. TYPE OF REPORT & PERIOD COVERED
7. AUTHOR(s) Randall E. Murphy G. E. Caledonia* Floyd H. Cook B. D. Green*		6. PERFORMING ORG. REPORT NUMBER ERP, No. 609
9. PERFORMING ORGANIZATION NAME AND ADDRESS Air Force Geophysics Laboratory (OPR-1) Hanscom Air Force Base Massachusetts 01731		8. CONTRACT OR GRANT NUMBER(s)
11. CONTROLLING OFFICE NAME AND ADDRESS Air Force Geophysics Laboratory (OPR-1) Hanscom Air Force Base Massachusetts 01731		10. PROGRAM ELEMENT, PROJECT, TASK AREA & WORK UNIT NUMBERS 2310-G4-01
14. MONITORING AGENCY NAME & ADDRESS (if different from Controlling Office)		12. REPORT DATE 15 September 1977
		13. NUMBER OF PAGES 96
		15. SECURITY CLASS. (of this report) Unclassified
16. DISTRIBUTION STATEMENT (of this Report) Approved for public release; distribution unlimited.		15a. DECLASSIFICATION/DOWNGRADING SCHEDULE
17. DISTRIBUTION STATEMENT (of the abstract entered in Block 20, if different from Report)		
18. SUPPLEMENTARY NOTES *Physical Sciences Inc., Woburn, MA.		
19. KEY WORDS (Continue on reverse side if necessary and identify by block number) Fluorescence Electron irradiated Carbon dioxide Infrared		
20. ABSTRACT (Continue on reverse side if necessary and identify by block number) A series of measurements of the time dependent infrared fluorescence histories of electron irradiated mixtures of CO <sub>2</sub> /X (X = Ar, He, N <sub>2</sub> ) have been performed. Fundamental band CO and CO <sub>2</sub> (ν) band radiation observed in these studies have been analyzed in some detail and rate constants for the processes CO(ν) + CO <sub>2</sub> → CO(ν - 1) + CO <sub>2</sub> <sup>*</sup> , ν ≤ 12 have been determined from the data. yields L <sub>2</sub> or = nu		

DDC  
RECEIVED  
FEB 2 1978  
B

DD FORM 1 JAN 73 1473 EDITION OF 1 NOV 65 IS OBSOLETE

Unclassified  
SECURITY CLASSIFICATION OF THIS PAGE (When Data Entered)

## Preface

We wish to thank Mr. James Rogers of AFGL for his generous assistance, including the use of his numerous computer programs. In addition, we would like to acknowledge the support of the Defense Nuclear Agency and in particular, Dr. Charles Blank.

This work was partially supported by the Defense Nuclear Agency (Atmospheric Effects Division) Subtask S99QAX-HI004-W. U. 07, as part of the LABCED program. Support was also derived from Air Force Project 2310-G4-01.

62704H

ACCESSION for	
NTIS	White Section <input checked="" type="checkbox"/>
DDC	Buff Section <input type="checkbox"/>
UNANNOUNCED	<input type="checkbox"/>
JUSTIFICATION	
BY	
DISTRIBUTION/AVAILABILITY CODES	
Dist.	AVAIL. and/or SPECIAL
A	



## Contents

1. INTRODUCTION	9
2. PRELIMINARY DATA ANALYSIS	10
2.1 Electron/Molecule Reactions	14
2.2 Ion Molecule Reactions	18
3. CO DATA ANALYSIS	36
3.1 Irradiated Gas Properties	36
3.2 Data Reduction	44
3.3 Data Interpretation	65
4. CO <sub>2</sub> DATA ANALYSIS	69
5. SUMMARY AND CONCLUSIONS	93
REFERENCES	95

## Illustrations

1. Time Dependent Fluorescence in an N <sub>2</sub> /CO <sub>2</sub> Mixture	11
2. Fluorescence in an N <sub>2</sub> /CO <sub>2</sub> Mixture vs Reverse Time in Steps of 0.1 msec	11
3. Fluorescence in X/CO <sub>2</sub> Mixtures vs Reverse Time in Steps of 0.1 msec	13
4. Fluorescence at Beam Termination in X/CO <sub>2</sub> Mixtures	15

## Illustrations

5. Ionization Cross Sections for $N_2$	17
6. Ionization Cross Sections for $CO_2$	17
7. Dissociation Cross Section for $N_2$	18
8. Electron Stopping Power vs Electron Energy for He, $N_2$ , Ar	25
9. Normalized Contour Plot of Volume Energy Deposition Rate in a Thick $N_2$ Gas Target	27
10. Room Temperature Rate Constants for the Reactions $CO(v) + CO_2 \rightarrow CO(v-1) + CO_2(\nu_3)$ and $CO(v) + N_2 \rightarrow CO(v-1) + N_2(v=1)$	32
11. Rate Constants for Vibration to Translation Deactivation of CO	34
12. Room Temperature Rate Constants for the Reaction $CO(v) + CO(0) \rightarrow CO(v-1) + CO(1)$	34
13. Electron Beam Half Current Radius at $L = 16$ cm, vs Gas Target Line Density	38
14. Electron Beam Irradiated Volume in a 16 cm Chamber vs Gas Target Line Density	38
15. Schematic of Beam Current Distribution Within Field of View	39
16. Predicted Einstein Coefficients for the Fundamental and First Overtone Bands of CO	47
17. Normalized Intensity at Times of $t = 3, 4, 5$ and $6$ msec in Order of Decreasing Intensity, Respectively	47
18. Synthetic and Measured Spectra at $t = 2.6$ msec	49
19. Synthetic and Measured Spectra at $t = 3.8$ msec	49
20. Synthetic and Measured Spectra at $t = 5.0$ msec	50
21. Synthetic and Experimental Spectra at $t = 6.2$ msec	50
22. Synthetic and Measured Spectra at $t = 7.0$ msec	51
23. Synthetic and Experimental Data at $t = 8.2$ msec	51
24. Deduced Relative Vibrational Population Distribution at Three Different Times	52
25. Deduced Time Histories of the Relative Populations of the First Five Levels of CO	53
26. Deduced Time Histories of the Relative Populations of Levels $v = 6-12$ of CO	53
27. $CO(v)$ Vibrational Relaxation Rate for $P_{CO_2} = 1/4$ torr, $I = 0.9$ mA	56
28. Measured Rate Constants for $CO(v) + CO_2 \rightarrow CO(v-1) + CO_2(\nu_3)$	57
29. Comparison of Measured and Computed Vibrational Population Time Histories for $v = 1-5$	58
30. Comparison of Measured and Computed Vibrational Population Time Histories for $v = 6-12$	58
31. Comparison of Measured and Predicted CO Vibrational Energy Decay	60
32. Synthetic and Measured Spectra at $t = 0.6$ msec	61

## Illustrations

33. Synthetic and Measured Spectra at $t = 1.6$ msec	61
34. Synthetic and Measured Spectra at $t = 2.4$ msec	62
35. Deduced Time Histories of the Relative Populations of the First Five Levels of CO	63
36. Deduced Time Histories of the Relative Populations of Levels $v = 6-12$ of CO	63
37. Relative Rates for Creation of Vibrationally Excited CO	64
38. Comparison of Measured and Computed Vibrational Population Time Histories for $v = 1-5$	64
39. Comparison of Measured and Computed Vibrational Population Time Histories for $v = 6-11$	65
40. Estimated Relative $\text{CO}(v)$ Creation Rates Due to $\text{CO}(A^1\pi) \rightarrow \text{CO}(X^1\Sigma)$ Transitions	68
41. Comparison of Predicted and Observed $\text{CO}_2(\nu_3)$ Relaxation Times	71
42. Fractional Transmission as a Function of Absorbing Gas Line Strength	75
43. Voigt Lineshapes for $a = 0$ and $a = 0.25$	77
44. Total Transmitted Intensity as a Function of $\text{CO}_2$ Pressure for Doppler and Lorentz Broadened Lines	80
45. Fraction of Total Unattenuated Band Intensity Transmitted for the Six Strongest Transitions for Doppler Lines, and for the Lorentz Broadened 626 Fundamental as a Function of $\text{CO}_2$ Pressure	82
46. Relative Contributions of Individual Bands to the Total Transmitted Radiation as a Function of $\text{CO}_2$ Pressure	82
47. Normalized Experimental Spectrum at $t = 2.6$ msec	84
48. Normalized Experimental Spectrum at $t = 2.6$ msec	84
49. Predicted $\text{CO}_2(\nu_3)$ Band Intensity	85
50. Predicted Transmitted $\text{CO}_2(\nu_3)$ Band Intensity	85
51. Predicted and Measured $\text{CO}_2(\nu_3)$ Band Transmitted Intensity	86
52. Predicted $\text{CO}_2(\nu_3)$ Band Transmitted Intensity	86
53. Predicted and Measured $\text{CO}_2(\nu_3)$ Band Transmitted Intensity of Doppler Broadened Lines	87
54. Comparison of Three Sets of Doppler Predictions for $\text{CO}_2\nu_3$ Band Radiation at 0.25 torr $\text{CO}_2$	88
55. Comparison of Three Sets of Doppler Predictions for $\text{CO}_2(\nu_3)$ Band Radiation at 1.00 torr of $\text{CO}_2$	89
56. Predicted Transmitted Intensity of $\text{CO}_2(\nu_3)$ Radiation for Lorentz Broadened Lines	90
57. Predicted Transmitted Intensity of $\text{CO}_2(\nu_3)$ Radiation for Lorentz Broadened Lines	90
58. Predicted Transmitted Intensity of $\text{CO}_2(\nu_3)$ Radiation for Lorentz Broadened Lines	91

## Illustrations

59. Predicted Transmitted Intensity of $\text{CO}_2(\nu_3)$ Radiation for Lorentz Broadened Lines	91
60. Relative Peak $\text{CO}_2(\nu_3)$ Population and Intensity vs $\text{CO}_2$ Pressure	93

## Tables

1. Ion Production Per Ion Pair $\text{N}_2/\text{CO}_2 = 100$	19
2. Ionization Energies	19
3. Species Production/Ion Pair	22
4. Electron Degradation Properties - $V = 32$ kV	25
5. Electron Beam Gas Interaction Parameters	26
6. Neutral Chemical Kinetics in $\text{N}_2/\text{CO}_2$ Mixtures	29
7. Beam Growth Parameters	37
8. $\text{CO}_2(\nu_3)$ Spectral Properties	78
9. Fractional Transmission of 626 Fundamental	81



## Infrared Fluorescence of Electron Irradiated CO<sub>2</sub> in the Presence of N<sub>2</sub>, Ar, and He

### 1. INTRODUCTION

The LABCEDE facility at the Air Force Geophysics Laboratory (AFGL) is used to observe the fluorescence behavior of electron irradiated gases. In this experiment a constant pressure, continuously flowing gas is irradiated by a pulsed, collimated electron beam of known current and voltage. As the electron beam passes through the gas, the beam electrons undergo collisions with the gas molecules which result in beam energy loss and spreading. Some fraction of the energy lost by the electron beam will, either directly or indirectly, appear as fluorescence in the gas. In the LABCEDE experiment, this fluorescence is observed through a window with the optical axis of the detection system at right angles to the beam axis.

For the case of infrared fluorescence, the primary diagnostic is a Michelson interferometer whose signal is channeled through a modified lock-in amplifier.<sup>1</sup> The interferometer is operated in a mode providing time resolved spectra, as previously described,<sup>2</sup> thus, high spectral resolution infrared histories of the fluorescing gas, both during and after electron beam excitation, can be developed.

(Received for publication 6 September 1977)

1. Cook, F.H., and Murphy, R.E. (1976) A Synchronous Signal Processing Technique for Repetitive Arbitrary Waveforms, AFCRL-TR-76-0035.
2. Murphy, R.E., Cook, F.H., and Sakai, H. (1975) J. Opt. Soc. Amer. 65:600.

Preliminary observations of this type in electron-irradiated gas mixtures of  $\text{CO}_2/\text{N}_2$  exhibited spectra typical of highly vibrationally excited CO, a species not present in the ambient gas mixture. The remainder of this text is devoted to an analysis of these results.

## 2. PRELIMINARY DATA ANALYSIS

Preliminary measurements of the infrared fluorescence resulting from the electron irradiation of  $\text{N}_2/\text{CO}_2$  mixtures were performed utilizing a two liter, gold-coated, integrating sphere in order to maximize the output intensity. Typical conditions for the measurements were  $P_{\text{N}_2} = 50 - 100$  torr,  $P_{\text{CO}_2} = 0.5 - 2.0$  torr, beam voltage  $V = 32-50$  kV, beam current  $I = 0.6-3$  mA, beam pulse time  $\tau_p = 2.5 - 5.0$  msec, and a beam duty cycle of  $\sim 20$  percent. A typical measurement of the observed time dependent fluorescence is shown in Figures 1 and 2. In Figure 1, the observed time dependent infrared fluorescence of a typical case is shown over the wavenumber range of  $1700-2500 \text{ cm}^{-1}$ . The spectral resolution of this data is  $\approx 10 \text{ cm}^{-1}$ . Note that the data shown is raw detector signal and has not been corrected for detector response and system transmission losses. The two dominant spectral features in this wavenumber region are the  $\text{CO}_2(\nu_3)$  band between  $2300-2400 \text{ cm}^{-1}$ , and what is apparently fluorescence from the fundamental band of highly vibrationally excited CO in the wavenumber range of  $1750-2200 \text{ cm}^{-1}$ . In the particular case shown, the electron beam pulse duration was 4.6 msec and it can be seen that the  $\text{CO}_2(\nu_3)$  intensity continues to rise in that time span whereas that of CO appears to approach "steady state" within 1-2 msec. After beam termination the fluorescence decays, the CO decays more rapidly than the  $\text{CO}_2$ . This can be seen best in Figure 2 where the same data is plotted in reverse time in order to more prominently exhibit the decay behavior.

In general, the data shown in Figures 1 and 2 are typical of observations made over the range of conditions considered. In particular for all cases (a) the CO intensity is of the same order as that of the  $\text{CO}_2(\nu_3)$  band even though  $\text{CO}_2$  is present in the ambient gas and CO is not, (b) the CO fluorescence reaches steady state more rapidly than  $\text{CO}_2$ , and (c) the peak CO intensity is independent of  $\text{CO}_2$  concentration. Furthermore, in all cases the CO is highly vibrationally excited. It can be shown that for a Boltzmann distribution, the vibrational temperature  $T_v$  may be deduced from the observed spectra by the relationship

$$T_v = V_{\text{max}} \bar{T} \quad (1)$$

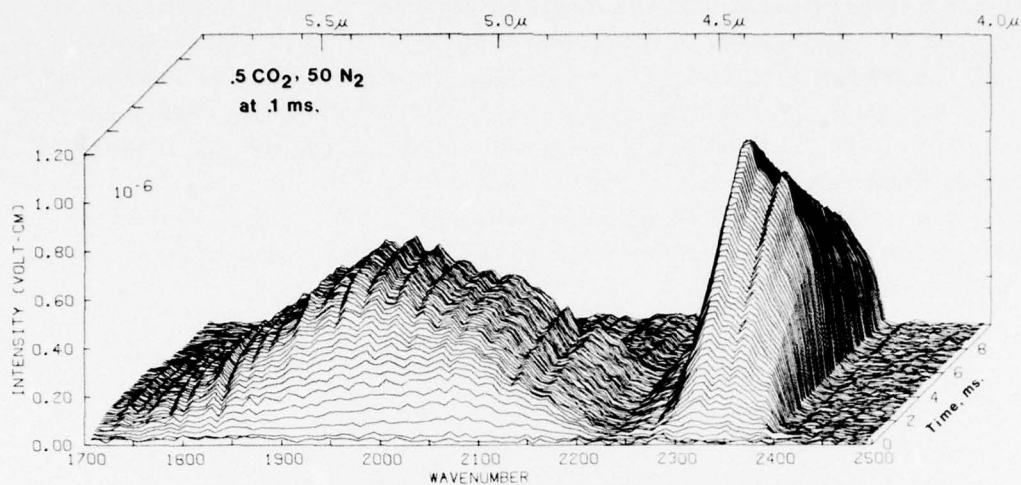


Figure 1. Time Dependent Fluorescence in an  $\text{N}_2/\text{CO}_2$  Mixture. Pressure listed in torr. Beam conditions  $v = 32 \text{ kV}$ ,  $I = 0.6 \text{ mA}$

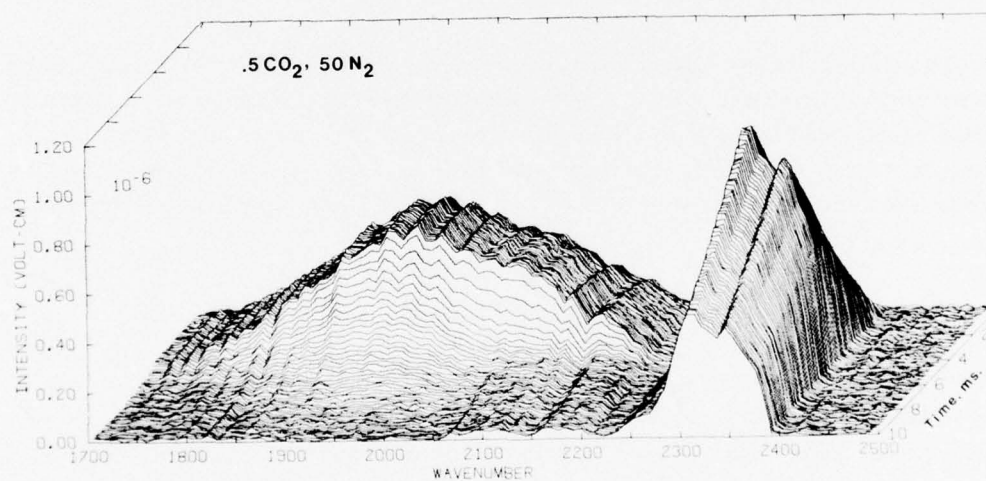
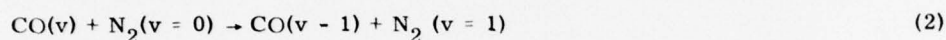


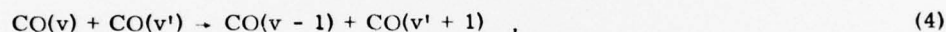
Figure 2. Fluorescence in an  $\text{N}_2/\text{CO}_2$  Mixture vs Reverse Time in Steps of 0.1 msec. Conditions as in Figure 1

where  $\bar{T}$  is the characteristic vibrational temperature,  $\approx 3100^\circ\text{K}$  for CO, and  $V_{\text{max}}$  is the vibrational level at which the intensity is highest. For the spectra shown in Figures 1 and 2,  $V_{\text{max}} \approx 6$ , and thus, if the CO vibrational distribution were Boltzmann, the observed spectra would correspond to a vibrational temperature of  $\approx 19,000^\circ\text{K}$ . This is to be compared with the gas translational temperature which is nominally ambient.

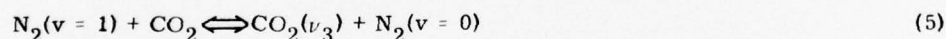
In principal data such as that shown in Figures 1 and 2, it can provide a significant amount of kinetic information. In particular, rate constants for the vibrational exchange processes.



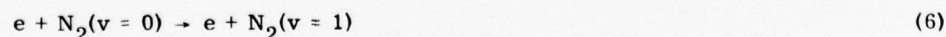
could be determined for a wide range of CO vibrational levels from the CO fluorescence decay observed after beam termination. Such analyses would unfortunately be complicated if the CO vibrational densities were sufficiently high so that intramode vibrational exchange processes, that is,



played a role in the relaxation processes. In any event once the manifold of decay rates were determined, the CO fluorescence observed during electron irradiation could be analyzed in order to specify the vibrational level dependent production/excitation rates for CO(v). Furthermore, for the cases considered, the  $\text{CO}_2(\nu_3)$  mode will be equilibrated with  $\text{N}_2(v = 1)$  through the rapid intermode vibrational exchange reaction



which is nearly thermo-neutral. Thus if the  $\text{CO}_2(\nu_3)$  vibrational temperature can be determined, the nitrogen vibrational temperature will also be specified. Nitrogen is vibrationally excited directly by beam electrons (and secondaries)



and thus a determination of the  $\text{N}_2$  vibrational temperature could lead to a determination of the global rate constant for reaction (6). In particular, it would be desirable to determine what fraction of the beam energy is converted to vibrationally excited nitrogen. (As will be shown later, such an analysis is complicated by the fact that the  $\text{CO}_2$  radiation within the test chamber is optically thick).



The kinetic interpretation of this data will of course be complicated by the fact that there are three vibrationally excited species present,  $N_2$ , CO, and  $CO_2$ , which may interact with each other. Therefore, in order to simplify the vibrational phenomenology as well as to more readily elucidate the CO production mechanism, fluorescence measurements were performed in electron irradiated mixtures of Ar/ $CO_2$  and He/ $CO_2$ . These measurements were performed for the same beam conditions, pressures and  $CO_2$  diluency as the measurement in the  $N_2/CO_2$  mixture. A comparison of the observed time dependent spectra in the three cases is shown in Figure 3 while a comparison of the spectra at one time is

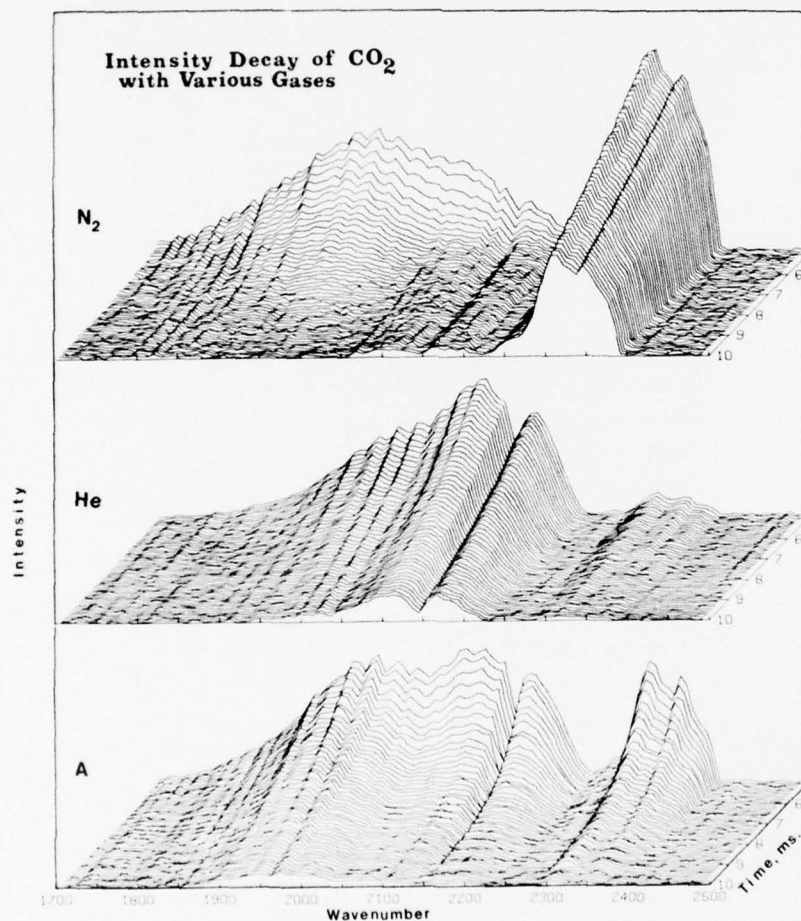


Figure 3. Fluorescence in X/ $CO_2$  Mixtures vs Reverse Time in Steps of 0.1 msec.  $P_X = 50$  torr,  $P_{CO_2} = 0.5$  torr. Beam conditions as in Figure 1

shown in Figure 4. As can be seen, highly vibrationally excited CO is observed in all three cases, although the CO vibrational population distributions vary from case to case. Note that the  $\text{CO}_2(\nu_3)$  radiation decreases more rapidly in the He and Ar mixtures than in  $\text{N}_2$ . This is because the vibrationally excited nitrogen acts as an excitation source for  $\text{CO}_2(\nu_3)$ , thus effectively increasing its apparent lifetime.

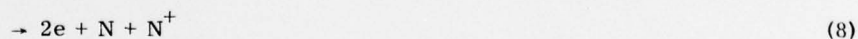
The observations in Ar and He are quite useful. In particular, they demonstrate that the production of vibrationally excited CO is not related to the presence of  $\text{N}_2$ . Furthermore, the rate constants for vibrational relaxation of CO by  $\text{CO}_2$  may be more readily deduced from the Ar/ $\text{CO}_2$  and He/ $\text{CO}_2$  data. These results could then be used in interpreting the  $\text{N}_2/\text{CO}_2$  observations.

Before any such analyses can be performed, however, the kinetic behavior occurring within the test chamber while the beam is on must be diagnosed. As the electron beam propagates through the gas it loses energy, slows down and spreads. The degree of spreading and energy loss is determined by the thickness, that is, gas number density times length, of the gas target. The lost beam energy is transferred to the gas causing molecular excitation, dissociation, ionization, and heating. Through such phenomena, species not originally present in the gas are created and these can effect, as well as produce, the resulting fluorescence histories. Furthermore, since the beam spreads and slows down, the electron excitation rates are spatially nonuniform whereas the fluorescence observations are integrated over a two-liter volume. Lastly, species created by the electron-beam can interact with each other, or with ambient species, to produce additional products. The electron/ion kinetics of a typical case is considered below in order to determine typical electron beam species production rates and the ultimate, gaseous products resulting from electron irradiation of  $\text{N}_2/\text{CO}_2$  mixtures.

## 2.1 Electron/Molecule Reactions

Neglecting excitation processes, the dominant electron-neutral reactions in irradiated  $\text{N}_2/\text{CO}_2$  mixtures are as follows:

(1) Ionization of  $\text{N}_2$



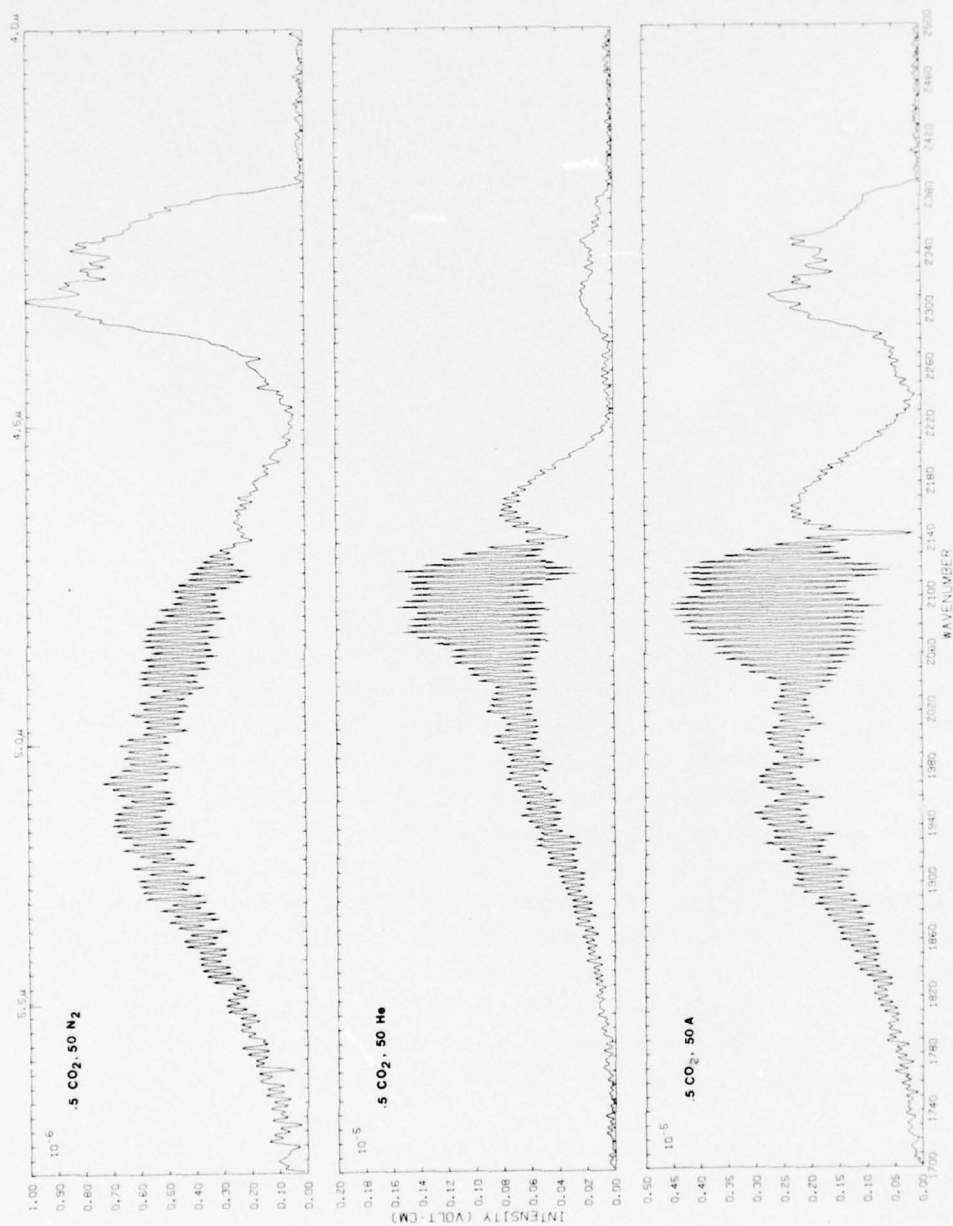
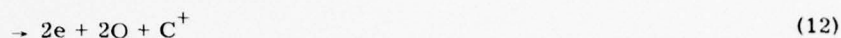
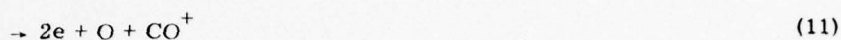
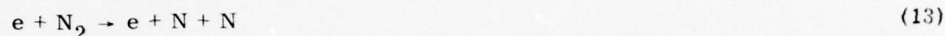


Figure 4. Fluorescence at Beam Termination in X/CO<sub>2</sub> Mixtures. Pressures listed in torr. Beam conditions as in Figure 1

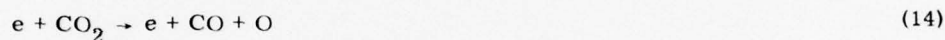
(2) Ionization of  $\text{CO}_2$



(3) Dissociation of  $\text{N}_2$



(4) Dissociation of  $\text{CO}_2$



(5) Etc ...

The cross sections for the first three of these processes are shown as a function of electron energy in Figures 5-7. The data of Figure 5 are taken from the work of Rapp and co-workers,<sup>3,4</sup> and that of Figure 6 from Crowe and McConkey.<sup>5</sup> The data of Figure 7 represents the difference between the total  $\text{N}_2$  dissociation cross section reported by Winters<sup>6</sup> and the dissociative ionization cross section of Rapp et al.<sup>4</sup> Little information is available on the direct dissociation of  $\text{CO}_2$ . This process has been dropped from the analysis inasmuch as the mixture ratio under consideration is  $\text{N}_2/\text{CO}_2$  of 100/1, and the  $\text{CO}_2$  dissociation cross section is anticipated to be less than that for ionization except at the lowest electron energies.

It is difficult to use these cross sections directly to calculate the various species production rates inasmuch as such production occurs through an electron cascade, and thus the effective rate involves an integral over the electron energy distribution. The average electron energy required to create an ion pair, has, however, been measured for a number of gases including  $\text{N}_2$ ; thus, the fractional

3. Rapp, D., and Englander-Golden, P. (1965) J. Chem. Phys. 43:1464.
4. Rapp, D., Englander-Golden, P. and Briglia, D. (1965) J. Chem. Phys. 42:4081.
5. Crowe, A., and McConkey, J.W. (1974) J. Phys. B7:349.
6. Winters, H.F. (1966) J. Chem. Phys. 44:1472.



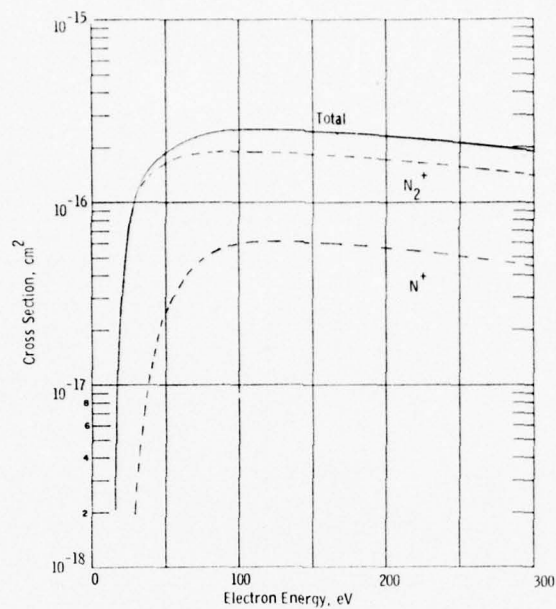


Figure 5. Ionization Cross Sections for  $N_2$

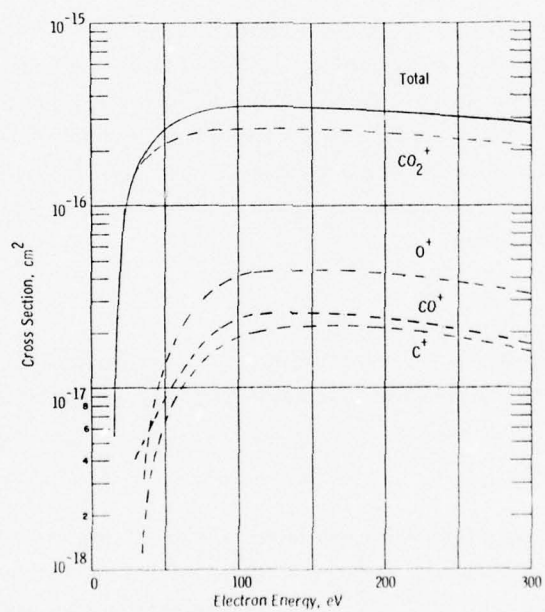


Figure 6. Ionization Cross Sections for  $CO_2$

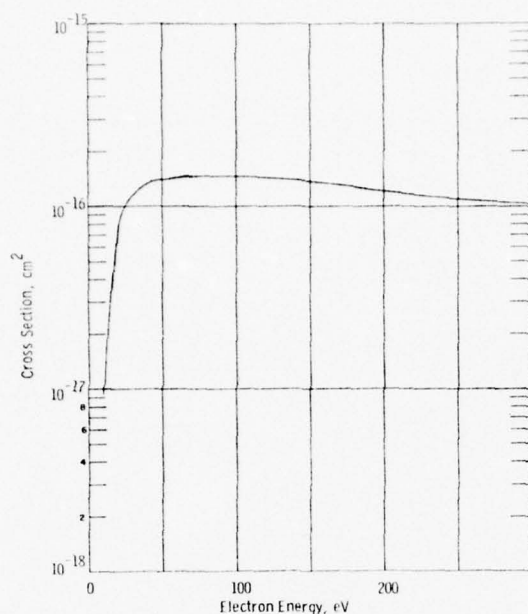


Figure 7. Dissociation Cross Section for  $N_2$

species created per ion pair can be estimated by ratioing the cross sections of the individual process to that for  $N_2$  ionization. This has been done at an electron energy of 100 eV, which is well above the threshold energy for the reactions considered. The results of this analysis are presented in Table 1 for the case of an  $N_2/CO_2$  ratio of 100. As would be anticipated, the dominant ions are  $N_2^+$  and  $N^+$ ; however, several other trace ions are created and these could play an important role in the further analysis.

## 2.2 Ion Molecule Reactions

The ions created by direct electron/molecule collisions will ultimately recombine with slow secondary electrons via rapid two body mechanisms such as



Such recombination reactions typically have rate constants of order  $10^{-7} \text{ cm}^3/\text{sec}$  at thermal energies. However, since the electron/ion concentrations in the gas will generally be less than  $10^{12}/\text{cm}^3$ , the characteristic time for ion destruction will be greater than  $10 \mu\text{sec}$ . As will be shown, a number of ion/molecule reactions will occur in the gas on time scales much shorter than  $10 \mu\text{sec}$ . The net effect of

Table 1. Ion Production Per Ion Pair  $N_2/CO_2 = 100$

Species	Fraction/Ion Pair	Additional Reaction Products
$N_2^+$	$\sim 0.75$	-
$N^+$	$\sim 0.24$	N
$CO_2^+$	$\sim 0.01$	-
$O^+$	0.0017	CO
$CO^+$	0.0010	O
$C^+$	0.00075	2O

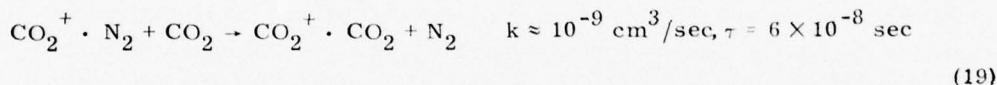
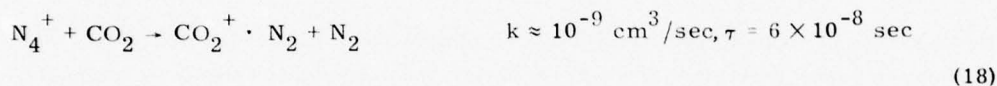
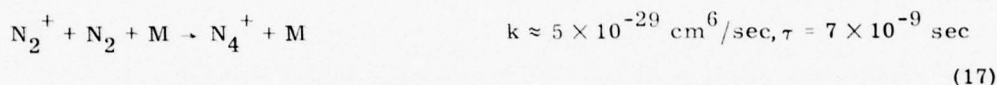
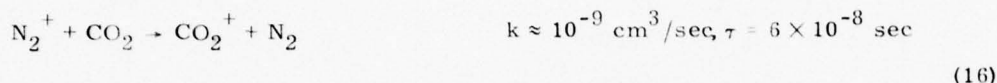
these reactions is that species with higher ionization energies will charge transfer to those of lower ionization energy. A listing of the ionization energies of species of interest is given in Table 2. As can be seen,  $CO_2$  has the lowest ionization energy of the four test gases of interest and thus, if the ion/molecule reaction rates are sufficiently rapid,  $CO_2^+$  will become the dominant positive ion in all these mixtures. (This would not be the case if a significant amount of  $O_2$  were created while the beam is on.)

Table 2. Ionization Energies

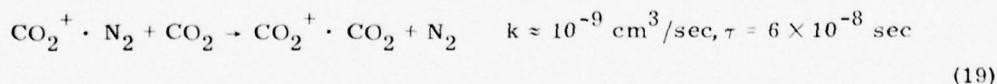
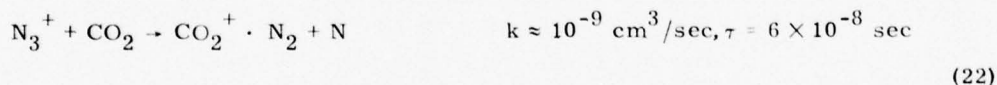
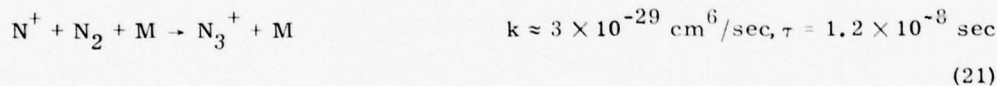
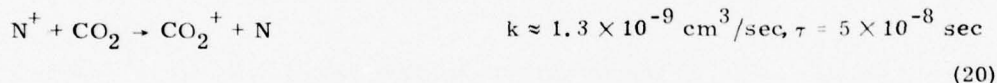
Species	$I$ , eV
$He^+$	25.58
$Ar^+$	15.76
$N_2^+$	15.58
$N^+$	14.55
$CO^+$	14.01
$CO_2^+$	13.77
$O^+$	13.62
$O_2^+$	12.20
$C^+$	11.27

The mechanisms by which this charge exchange occurs can produce additional neutral species and are discussed below. The rate constants used in this discussion are taken for the most part from<sup>7-9</sup> other sources, and the characteristic reaction times listed are for the case of  $P_{N_2} = 50$  torr,  $P_{CO_2} = 0.5$  torr. (These characteristic times scale inversely with pressure or pressure squared for binary and tertiary reactions respectively.) The primary reaction mechanisms for each beam produced ion are:

(1)  $N_2^+$



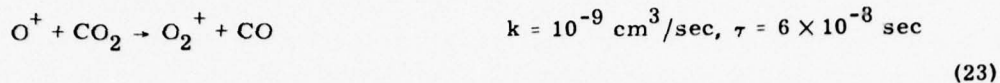
(2)  $N^+$



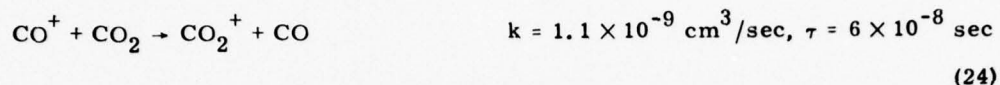
7. Fehsenfeld, F.C., Schmeltekopf, A.L., Dunkin, D.B., and Ferguson, F.E. (1969) Compilation of Reaction Rate Constants Measured in the ESSA Flowing Afterglow System to August 1969, ESSA Technical Report ERL 135-AL3.
8. Ferguson, E.E. (1973) Atom. Dat. and Nucl. Dat. Tables 12:159.
9. Good, A. (1975) Chem. Rev. 75:561.



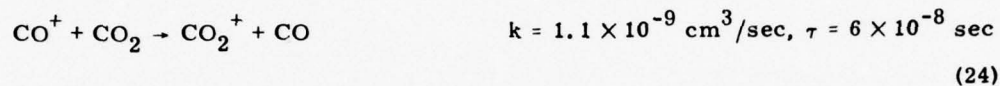
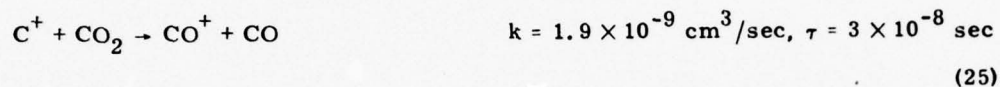
(3)  $O^+$



(4)  $CO^+$



(5)  $C^+$



As can be seen, with the exception of  $O^+$ , all directly produced ionic species charge transfer to  $CO_2^+$ . Ultimately, the two terminal ions  $CO_2^+$  and  $O_2^+$  recombine producing neutral species. The appropriate reaction mechanisms are



and therefore the ultimate conversion of ionic to neutral species may be represented by the global reactions

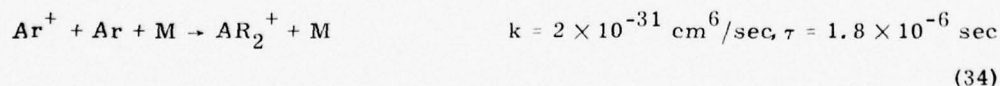
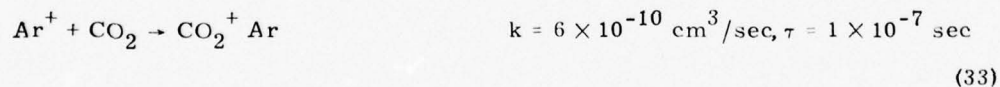


From consideration of the global reactions (28)-(32), the fractional ionization levels of Table 1, and the dissociation cross section of  $N_2$  shown in Figure 7, the total production of neutrals per ion pair may be specified. These are listed in Table 3. From the analysis above, species such as C, NO, CN, and  $O_2$  are not created (except possibly in trace quantities), through the sequence of electron or ion reactions occurring in the gas. Furthermore, the dominant source of CO production, reaction (26), has been identified.

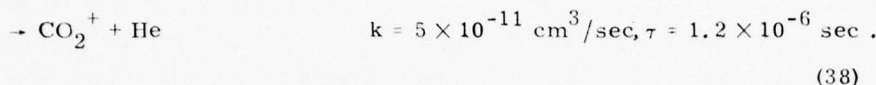
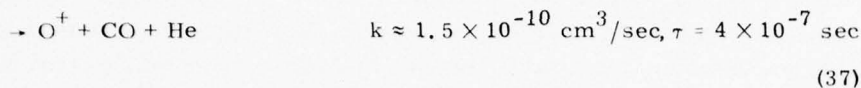
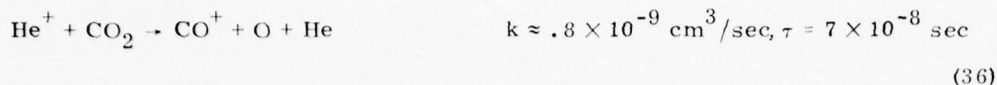
Table 3. Species Production/Ion Pair

Mixture	Species	Production Per Ion Pair
$N_2/CO_2 = 100$	N	1.6
	O	1.0
	CO	1.0
$Ar/CO_2 = 100$	O	1.0
	CO	1.0
$He/CO_2 = 100$	O	2.1
	CO	2.1

Similar, although less complicated, analysis can be provided for the  $Ar/CO_2$  and  $He/CO_2$  mixtures. In the case of Ar, the dominant ion produced is  $Ar^+$  and the relevant reaction sequence is



and thus each  $Ar^+$  produces a  $CO_2^+$  which upon recombination produces one CO molecule and one oxygen atom per ion pair. The case of Helium is somewhat more complicated because the reaction between  $He^+$  and  $CO_2$  has three branches



The  $\text{CO}^+$  created will charge exchange to  $\text{CO}_2$  via reaction (24); however, the  $\text{O}^+$  will form the terminal ion  $\text{O}_2^+$  via reaction (23). The net species production rates from this sequence of reactions is listed in Table 3. It is to be noted that, unlike the  $\text{N}_2/\text{CO}_2$  and  $\text{Ar}/\text{CO}_2$  mixtures, more than half of the CO created in  $\text{He}/\text{CO}_2$  mixtures is the result of charge exchange reactions. The recombination reaction (26) is, however, the only mechanism for CO formation which is common to all three mixtures.

It is evident that in all three mixtures, significant quantities of CO and free radicals are created by the electron beam radiation. Although it has been found that electron and ion reactions occur on a very short time scale — and thus will only take place while the beam is on — reactions between neutral species can occur on longer time scales. Furthermore, the concentration of beam-produced neutral species with the chamber can increase from pulse to pulse. Indeed, although the e-beam pulse duration is  $\leq 5$  msec the gas residence time within the test chamber has been measured to be 10-15 sec for the cases shown in Figures 1-4. Thus the concentration of beam-produced species could build up to sufficiently large levels in the test chamber so that they could effect the relaxation behavior of the observed fluorescence.

To provide an estimate of this effect the amount of energy supplied to the gas by the electron beam, and the gas volume to which this energy is supplied, must be specified. As mentioned earlier the energy deposition is gas specific, spatially nonuniform, and will depend upon the thickness of the target. Beam energy degradation is generally defined in terms of the electron stopping power,  $1/\rho \text{ dE/dx}$ , which is a function of beam voltage. The total energy lost per electron by a beam propagating a distance  $l$  through a target of density  $\rho$  is defined by

$$\Delta E = \int_0^l \rho \left( \frac{1}{\rho} \text{ dE/dx} \right) dx \quad (39)$$

where the fact that beam voltage decreases with increasing propagation distance is implicitly included in the evaluation of the integral. Values of  $1/\rho \, dE/dx$  for a beam voltage of 32 keV are listed in Table 4 for the gases of interest. Also listed are gas molecular weights, the effective range over which a beam with initial energy of 32 keV would be dissipated and the average number of eV required to produce an ion pair in the gas. The listed values of range and electron stopping power were taken from the tabulation of Berger and Seltzer,<sup>10</sup> and the energies per ion pair were taken from the work of Whyte.<sup>11</sup> The variation in beam stopping power with beam voltage is also shown in Figure 8 for the gases  $N_2$ , He, and Ar.

Such tabulations are sufficient to calculate the energy transfer and ion creation rates for the cases of interest. The integrating sphere used in the measurements has a diameter of  $\approx 16$  cm and thus  $\Delta E$  may be determined from Eq. (39) using the electron stopping powers plotted in Figure 8. The power supplied to the gas when the beam is on, is then defined by

$$P = I\Delta E \quad (40)$$

and the rate for creation of ion pairs within the test chamber is defined by

$$\dot{X}^+ = P/we \quad (41)$$

where  $e$  is the unit electron charge. Furthermore, the total energy supplied to the gas per pulse and number of ion pairs created per pulse may be determined by multiplying Eqs. (40) and (41) by the pulse duration  $\tau_p$ . Finally one must evaluate the total energy transferred, and ion pairs created, during the gas residence time within the test chamber. These quantities may be determined from Eq. (40) and (41) by multiplying by the product of the gas residence time  $\tau_R$  and the beam duty cycle  $\eta$ . These quantities are listed in Table 5 for the three mixtures of interest. The parameters used in evaluating these quantities were  $I = 0.6$  mA,  $\tau_p = 4.6$  msec,  $\tau_R = 10$  sec and  $\eta = 0.2$ .

The quantities listed in Table 5 are essentially integrals of the total energy and number of ion pairs created within the two liter integrating sphere. It would be valuable to determine the volume of gas, within the sphere, which is irradiated by the beam so that the local densities of beam produced species could be defined. This determination is complicated by the fact that the beam energy deposition is spatially nonuniform. For example the Ar and  $N_2$  mixtures may be considered as optically thick; while the electron range, as tabulated in Table 4, being 28 cm. A

10. Berger, M.J., and Seltzer, S.M. (1964) Tables of Energy Losses and Ranges of Electrons and Positrons, NASA SP-3012.

11. Whyte, G.N. (1963) Radiation Res. 18:255.



Table 4. Electron Degradation Properties - V = 32 kV

Gas	Molecular Weight gm/mole	Stopping Power MeV-cm <sup>2</sup> /gm	Range gm/cm <sup>2</sup>	Energy Per Ion Pair eV
He	4	9.1	$2.0 \times 10^{-3}$	41.9
N <sub>2</sub>	28	8.1	$2.1 \times 10^{-3}$	34.4
Ar	40	6.2	$3.0 \times 10^{-3}$	26.1
CO <sub>2</sub>	44	8.1	$2.2 \times 10^{-3}$	--

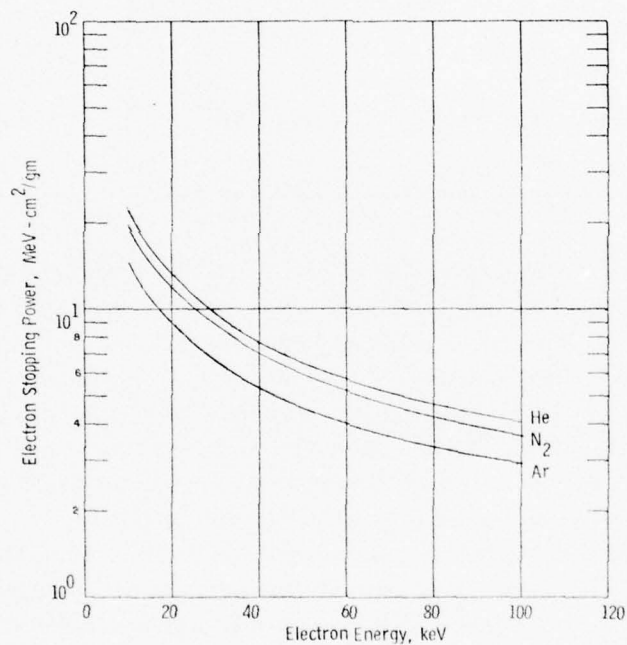


Figure 8. Electron Stopping Power vs Electron Energy for He, N<sub>2</sub>, Ar

Table 5. Electron Beam Gas Interaction Parameters

Gas Mixture	50 torr He- 0.5 torr CO <sub>2</sub>	50 torr N <sub>2</sub> - 0.5 torr CO <sub>2</sub>	50 torr Ar- 0.5 torr CO <sub>2</sub>
Density, gms/cc	$1.2 \times 10^{-5}$	$7.5 \times 10^{-5}$	$1.08 \times 10^{-4}$
$\Delta E$ , eV	$1.8 \times 10^3$	$1.1 \times 10^4$	$1.1 \times 10^4$
P watts	1.1	6.6	6.6
$\dot{X}^+$ , sec <sup>-1</sup>	$1.6 \times 10^{17}$	$1.2 \times 10^{18}$	$1.6 \times 10^{18}$
Energy/ Pulse Joules	$5.1 \times 10^{-3}$	$3 \times 10^{-2}$	$3 \times 10^{-2}$
Ion Pairs/ Pulse	$7.4 \times 10^{14}$	$5.5 \times 10^{15}$	$7.4 \times 10^{15}$
Energy in $\tau_R$ Joules	2.2	13.2	13.2
Ion Pairs in $\tau_R$	$3.2 \times 10^{17}$	$2.4 \times 10^{18}$	$3.2 \times 10^{18}$

measurement of the volume energy distribution rate in a thick target is shown in Figure 9, as excerpted from Cohn and Caledonia.<sup>12</sup> As can be seen both the axial and radial variation of the deposition rate is quite significant over the cloud length. Indeed it can be seen that variations of over an order of magnitude in local ion pair creation rates and energy deposition, will occur within the test chamber. Although the helium mix may be considered a thin target, the energy deposition in this case will also vary significantly over the length of the integrating sphere (thin target behavior will be discussed in more detail later in the text).

Thus, considerable effort would be required in order to define the pulse-to-pulse beam energy deposition. An approximate estimate can be provided for the long time build up of beam-produced species and energy because of diffusive effects. A typical value of the diffusion coefficient for species such as CO diffusing in N<sub>2</sub> or Ar at pressures of 50 torr would be  $\approx 3 \text{ cm}^2/\text{sec}$ . Atomic species, or species in a helium carrier gas would exhibit even larger diffusion coefficients. The characteristic distance L in which species will diffuse in a time t may be approximated by the relationship

12. Cohn, A., and Caledonia, G. (1970) J. Appl. Phys. 41:3767.

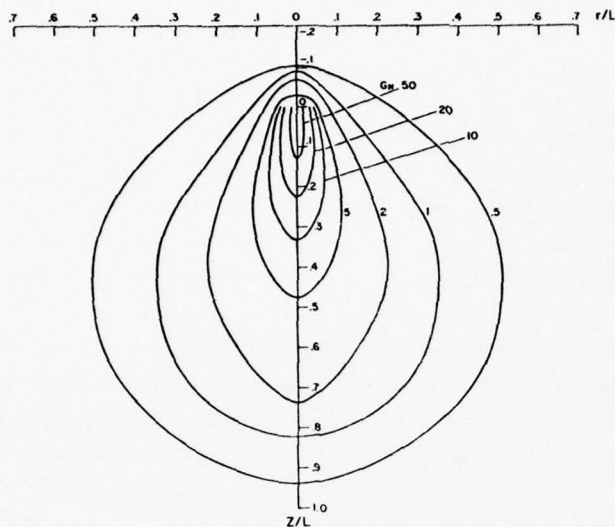


Figure 9. Normalized Contour Plot of Volume Energy Deposition Rate in a Thick  $N_2$  Gas Target.  $L$  is the electron practical range. (excerpted from ref. 12)

$$L \approx (Dt)^{1/2} \quad (42)$$

where  $D$  is the diffusion coefficient. For the gas residence time of 10 sec, this characteristic dimension would be  $\approx 5.5$  cm, which is comparable to the 8 cm radius of the integrating sphere. Thus, to first order the volume of beam - effected gas may be estimated to be  $10^3$   $\text{cm}^3$ . From Table 5, that would imply that the average number of ion pairs produced per  $\text{cm}^3$  during the gas residence time would be  $\approx 3.2 \times 10^{14}$ ,  $2.4 \times 10^{15}$ , and  $3.2 \times 10^{15}$  for the He,  $N_2$ , and Ar mixtures, respectively. Furthermore, the energy imparted to the gas by the beam would cause an increase in gas temperature. The estimated gas temperature increase over the residence time would be 40, 160 and  $240^\circ\text{K}$  for the He,  $N_2$ , and Ar mixes, respectively.

It should be remembered that these estimates are crude and could be off by a factor of two or more because of uncertainties in the definition of the volume of gas affected by the beam and in the gas residence time. Nonetheless, these perturbations are large and most probably would play a role in the kinetics controlling the observed vibrational fluorescence. Specifically from Table 3, it can be seen that for each ion pair formed at least one oxygen atom and CO molecule are produced

and, in the case of nitrogen, 1.6 nitrogen atoms are also produced. Since it has been shown that  $3 \times 10^{14} - 3 \times 10^{15}$  ion pairs are produced per  $\text{cm}^3$  during the gas residence time, then at least that many O, CO and, depending on mixture, N will ultimately be produced. These concentrations are to be compared to the initial  $\text{CO}_2$  concentration of  $1.6 \times 10^{16}/\text{cm}^3$ .

The actual concentration of beam produced neutral species need not increase to such high concentrations inasmuch as neutral species chemical reactions will occur within the test chamber. These chemical reactions could lead to the recombination of beam produced neutral species or alternately to the creation of new species. Thus, the neutral chemistry occurring within the chamber must be modeled in order to determine the average composition of the electron irradiated gas within the chamber. The dominant neutral kinetic mechanisms occurring in a mixture of  $\text{N}_2/\text{CO}_2$  dosed with O, N, and CO are listed in Table 6. The rate constants for these reactions were taken from Garvin and Hampson<sup>13</sup> with the exceptions of reactions (d) and (h) which were deduced from the studies of Inn<sup>14</sup> and Slinger et al,<sup>15</sup> and from Rawlins and Kaufman,<sup>16</sup> respectively.

Reaction (h) of Table 6 is perhaps the most crucial reaction in the sequence. For example, if the reaction between nitrogen atoms and  $\text{CO}_2$  were rapid, then an additional CO molecule could be produced for every nitrogen atom created while the electron beam is on. Furthermore alternate reaction paths, which would ultimately create species such as CN, might be possible. Fortunately, while this analysis was in progress, Rawlins and Kaufmann<sup>16</sup> published a timely study on the reaction of  $\text{CO}_2$  with active nitrogen. In this work, it was found that the dominant reaction between nitrogen atoms and  $\text{CO}_2$  occurred in a several step mechanism involving an excited electronic state of nitrogen,  $\text{N}_2^*$ . The general reaction sequence proposed by Rawlins and Kaufmann to describe their observations is



13. Garvin, D., and Hampson, R. F., editors (1974) Chemical kinetics data survey VII, Tables of Rate and Photochemical Data for Modeling at the Stratosphere (Revised), NBSIR 74-430.

14. Inn, E. C. Y. (1974) J. Chem. Phys. 61:1589.

15. Slinger, T. G., Wood, B. J., and Black, G. (1972) J. Chem. Phys. 57:233.

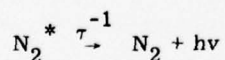
16. Rawlins, W. T., and Kaufman, F. (1976) J. Chem. Phys. 64:1128.



Table 6. Neutral Chemical Kinetics in  $N_2/CO_2$  Mixtures

	$k$ ( $cm^3/sec$ or $cm^6/sec$ )
(a) $O + O + N_2 \rightarrow O_2 + N_2$	$4.8 \times 10^{-33} (300/T)$
(b) $O + N + N_2 \rightarrow NO + N_2$	$1.8 \times 10^{-31} T^{-1/2}$
(c) $O + O_2 + N_2 \rightarrow O_3 + N_2$	$1.05 \times 10^{-34} e^{510/T}$
(d) $O + CO + N_2 \rightarrow CO_2 + N_2$	$0.8 \times 10^{-33} e^{-1780/T^*}$
(e) $O + O_3 \rightarrow 2O_2$	$1.9 \times 10^{-11} e^{-2300/T}$
(f) $N + N + M \rightarrow N_2 + M$	$8.3 \times 10^{-34} e^{500/T}$
(g) $N + NO \rightarrow N_2 + O$	$2.7 \times 10^{-11}$
(h) $N + N + CO_2 \rightarrow CO + N_2 + O$ $N + CO_2 \rightarrow NO + CO$	$\left\{ \begin{array}{l} \text{see text} \end{array} \right.$
(i) $O_3 + N_2 \rightarrow O + O_2 + N_2$	$6.6 \times 10^{-10} e^{-11,400/T}$
(j) $N + O_2 \rightarrow NO + O$	$1.1 \times 10^{-14} T e^{-3150/T}$
(k) $N + O_3 \rightarrow NO + O_2$	$5.7 \times 10^{-13}$
(l) $O + NO + N_2 \rightarrow NO_2 + N_2$	$4.2 \times 10^{-33}$
(m) $O + NO_2 \rightarrow NO + O_2$	$9.1 \times 10^{-12}$
(n) $O + NO_2 + N_2 \rightarrow NO_3 + N_2$	$1. \times 10^{-31}$
(o) $O_3 + NO \rightarrow NO_2 + O_2$	$9 \times 10^{-13} e^{-1200/T}$
(p) $O_3 + NO_2 \rightarrow NO_3 + O_2$	$1.1 \times 10^{-13} e^{-2450/T}$
(q) $N + NO_2 \rightarrow 2NO (?)$	$1.85 \times 10^{-11}$
(r) $NO + NO_3 \rightarrow 2NO_2$	$\sim 10^{-11}$

\*This rate is based on the authors interpretation of studies presented in refs. 14 and 15.

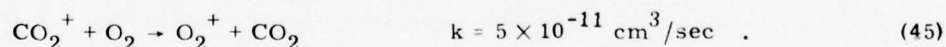


where, for the present case, M represents  $N_2$  and  $CO_2$ . (This sequence of reactions is further complicated in that  $N_2^*$  may be produced in several different vibrational states each of which has a different quenching constant.) The reaction sequence (43) may be represented by the global reaction



where the rate constant  $k_{44}$  is a function of the ratio of  $N_2$  to  $CO_2$ . It may be determined from the work of Whyte,<sup>11</sup> that a value  $k_{44} = 4 \times 10^{-33} \text{ cm}^6/\text{sec}$  is appropriate for the conditions of the present analysis. Thus the only important neutral reaction occurring in the test chamber which involves  $CO_2$  is a relatively slow three body process. From examination of Table 6 it can be seen that the same is true regarding reactions involving CO.

E. Lee of AFGL has exercised the reaction scheme of Table 6 in order to determine the final neutral species products produced in the test chamber. His calculation included pulsed source terms for O, CO, and N as per the beam duty cycle. It was found that on time scales less than 1 sec the oxygen atom concentration approaches "steady state" and the two dominant species increasing in time without significant loss are CO and  $O_2$ . At larger times, species such as NO and  $O_3$  begin to play a role in the kinetics. It will be recalled that  $O_2$  was not considered as a collision partner in the previously discussed analysis of the ionic kinetics. If sufficient  $O_2$  is present in the chamber,  $O_2^+$  will become the dominant ion and the production of vibrationally excited CO via electron ion recombination, reaction (26), would cease. The primary initial ions created by the beam, such as  $N_2^+$  and  $N^+$  will not preferentially form  $O_2^+$  over  $CO_2^+$  unless the  $O_2$  concentration exceeds that of  $CO_2$ . This is because the rate constants for charge exchange to  $CO_2$  are typically larger than these for charge exchange to  $O_2$ . However, the  $CO_2^+$  itself will directly charge exchange to  $O_2$  via the reaction



Thus when the  $O_2$  concentration is sufficiently large so that reaction (45) will occur more rapidly than electron-ion recombination, the dominant positive ion will be  $O_2^+$  rather than  $CO_2^+$ . The characteristic time for recombination is estimated to be 10  $\mu\text{sec}$  and thus the condition for  $O_2^+$  to become the dominant ion becomes

$$5 \times 10^{-11} N_{O_2} > 10^5 \quad (46)$$

or

$$N_{O_2} > 2 \times 10^{15}/\text{cm}^3 \quad . \quad (47)$$

It can be seen from reference to Table 5 that the density of oxygen molecules listed above is of the same order of magnitude as that predicted to build up within the chamber during the gas residence time. Thus the production mechanism for vibrationally excited CO will be partially effected by the presence of beam-produced species.

The arguments presented here for  $N_2/\text{CO}_2$  mixtures will also be true for the  $\text{Ar}/\text{CO}_2$  mixture. The neutral reaction mechanism in the latter mixtures will be the same as that listed in Table 6 with the exception of the reactions involving N and  $N_2$ . In the case of the  $\text{He}/\text{CO}_2$  mixture, CO and  $O_2$  will again be the dominant beam produced neutrals; however, the  $O_2$  concentration will not be sufficiently high to effect the  $\text{CO}_2^+$  concentration.

The conclusion of the kinetic analysis is that, over the gas residence time of 10 sec, significant quantities of electron beam produced neutral species will build up in the test chamber for the gas and electron beam conditions typical of the data base. These beam produced species will be dominantly  $O_2$  and CO with traces of O,  $O_3$  and in the case of the nitrogen mix, NO and  $\text{NO}_2$ . Indeed the predicted concentrations of CO and  $O_2$  for the  $N_2$  and Ar mixes are within 10-20 percent of the initial  $\text{CO}_2$  concentrations (this of course implies that the  $\text{CO}_2$  concentration has decreased by this much). Furthermore, significant increases in gas temperature have also been predicted. These phenomena effectively preclude the determination of any kinetic data from the observed CO fluorescence histories; however, the analysis developed may be used to define the experimental conditions required in order to take viable data.

Before proceeding with this definition, it is worthwhile reviewing the available rate constant data base for the kinetic mechanisms of interest in order to ascertain the maximum acceptable levels of beam produced species within the test chamber. The basic kinetic mechanisms to be studied are



The available room temperature rate constants for these two slightly endothermic processes are shown in Figure 10. The rate constants for processes (2) and (3) for  $v = 1$  are well defined. The value shown in Figure 10 for  $N_2$  is representative

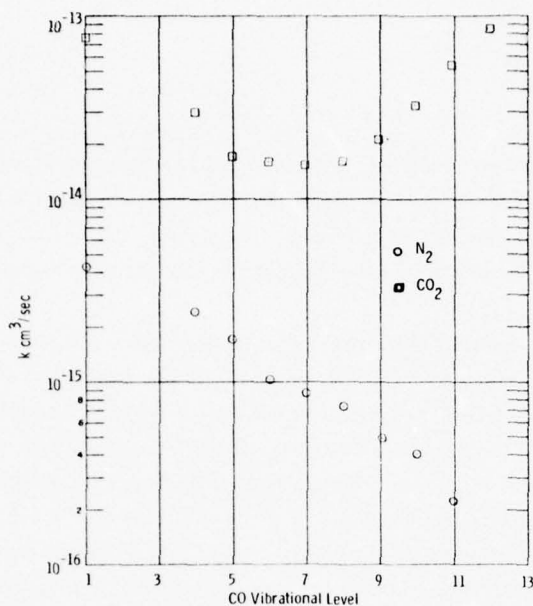


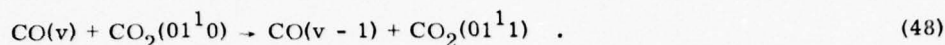
Figure 10. Room Temperature Rate Constants for the Reactions  $\text{CO}(v) + \text{CO}_2 \rightarrow \text{CO}(v-1) + \text{CO}_2(v_3)$  and  $\text{CO}(v) + \text{N}_2 \rightarrow \text{CO}(v-1) + \text{N}_2(v=1)$

of measurements provided in references<sup>17-19</sup> and the value shown for  $\text{CO}_2$  is as reported in references.<sup>20-23</sup> The data shown for vibrational levels  $\geq 4$  for both  $\text{N}_2$  and  $\text{CO}_2$  are taken from the work of Hancock and Smith.<sup>24</sup> No measurements are available for  $v = 2, 3$ . Note the decreasing rate constant with increasing vibrational level is an expected behavior since the anharmonicity of the CO molecule is such that the endothermicity of reactions (2) and (3) increases with increasing vibrational level. The observed increasing rate constant for process (3) at

17. Green, W.H., and Hancock, J.K. (1973) IEEE J. Quantum Electr. QE-9:50.
18. Starr, D.F., Hancock, J.K., and Green, W.H. (1974) J. Chem. Phys. 61:5421.
19. Zittel, P.F., and Moore, C.B. (1972) Appl. Phys. Letters 21:81.
20. Rosser, W.A., Jr., Sharma, R.D., and Gerry, E.T. (1971) J. Chem. Phys. 54:1196.
21. Stephenson, J.C., and Moore, C.B. (1972) J. Chem. Phys. 56:1295.
22. Miller, D.J., and Millikan, R.C. (1974) Chem. Phys. 6:317.
23. Starr, D.F., and Hancock, J.K. (1975) J. Chem. Phys. 63:4730.
24. Hancock, G., and Smith, I.W.M. (1971) Appl. Opt. 10:1827.



vibrational levels  $\geq 7$  is surprising and it has been postulated<sup>24</sup> to occur because of a contribution from the reaction

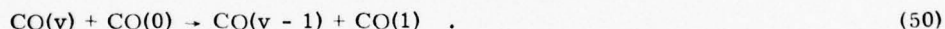


The other mechanism involving CO and the test gases is vibration to translation (V-T) deactivation



where M can be  $\text{N}_2$ ,  $\text{CO}_2$ , Ar or He. The vibrational level dependent rate constants for process (49) have been measured only for helium and are shown in Figure 11. The rate constant for  $v = 1$  is from the work of Miller and Millikan<sup>25</sup> while those for  $v = 9 - 13$  are from Hancock and Smith.<sup>24</sup> Also shown is a theoretical prediction for the rate constant for process (49) with  $\text{M} = \text{N}_2$ . This prediction, taken from,<sup>26</sup> is based upon SSH Theory<sup>27</sup> and is representative of the expected behavior and magnitude of the V-T rates for  $\text{M} = \text{CO}_2$ , Ar. Note - from a comparison of the data in Figures 10 and 11 - it can be seen that CO V-T deactivation by He will be competitive with CO VV exchange to  $\text{CO}_2$  in 100:1 mixtures of He- $\text{CO}_2$ . On the other hand, V-T collisions with  $\text{N}_2$ ,  $\text{CO}_2$  and Ar will be unimportant.

The dominant beam produced neutral species will be vibrationally cold CO which can react with vibrationally excited CO via the intramode vibration to vibration (V-V) exchange reaction



Process (50) does not decrease the number of vibrational quanta, but rather rearranges the distribution of quanta, and thus can effect the relaxation of individual vibrational levels. Several<sup>24, 28, 29</sup> measurements of the room temperature rate constants for process (50) are shown in Figure 12 and they can be seen to be in agreement to within a factor of two. The rate constant for  $v = 1$  is not shown since it corresponds to a null reaction. The maximum concentration of cold CO which can be allowed in the system may be deduced by comparing the rate constants of

25. Miller, D.J., and Millikan, R.C. (1970) J. Chem. Phys. 53:3354.

26. Center, R.E., and Caledonia, G.E. (1971) Appl. Opt. 10:1795.

27. Schwartz, R.N., Slawsky, Z., and Herzfeld, K.F. (1952) J. Chem. Phys. 20:1591.

28. Liu, Y.S., McFarlane, R.A., and Wolga, G.J. (1975) J. Chem. Phys. 63:228.

29. Fushiki, Y., and Tsuchiya, S. (1974) Jap. J. Appl. Phys. 13:1043.

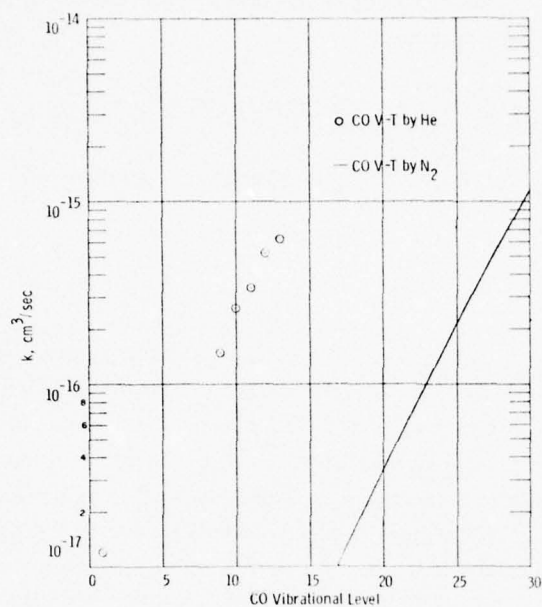


Figure 11. Rate Constants for Vibration to Translation Deactivation of CO (○ ref. 24, — ref. 26)

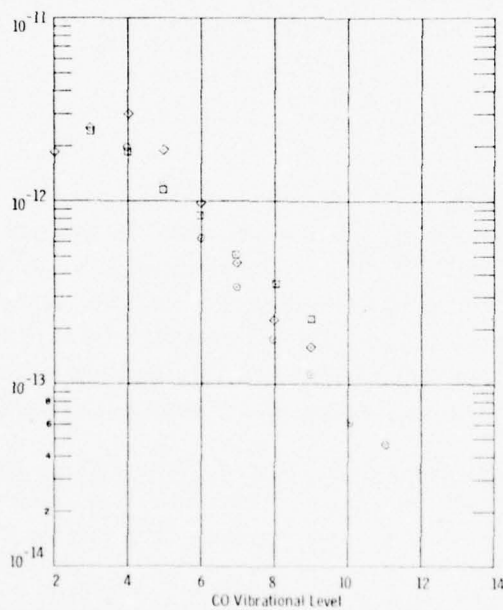
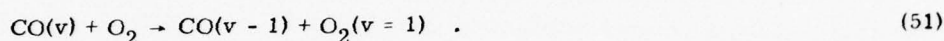


Figure 12. Room Temperature Rate Constants for the Reaction  $\text{CO}(v) + \text{CO}(0) \rightarrow \text{CO}(v-1) + \text{CO}(1)$  (○ ref. 24, □ ref. 28, ◇ ref. 29)

process (50), Figure 12, with those for reactions (2) and (3), Figure 10. For example, if it is required that reaction (50) have no more than a 10 percent effect on the relaxation of any vibrational level then it is required that  $[CO] \lesssim 10^{-3} [CO_2]$  or  $10^{-4} [N_2]$ . For a 1 percent effect, the CO concentration would have to be an order of magnitude smaller than those listed above. As a numerical example, for the Ar/CO<sub>2</sub> mix considered earlier the CO<sub>2</sub> concentration was  $1.6 \times 10^{16}/\text{cm}^3$  and thus — if it is desired that cold CO contribute less than 10 percent to the observed relaxation of any vibrational level — the CO concentration must be less than  $1.6 \times 10^{13}/\text{cm}^3$ . This CO density is two orders of magnitude lower than the predicted density of the preliminary measurements.

The only other diatomic molecule created in large quantities by the electron beam is O<sub>2</sub>. This species may react with CO via the V-V exchange reaction



The room temperature rate constant for process (51),  $v = 1$ , has been found<sup>24, 30</sup> to have the low value of  $6 \times 10^{-17} \text{ cm}^3/\text{sec}$ . However, since the reaction is exothermic, the rate constant is expected to increase with increasing CO vibrational level; that is, the exothermicity decreases with increasing  $v$  and thus the reaction approaches energy resonance. Indeed Hancock and Smith<sup>24</sup> have determined the rate constants for process (51),  $v = 12, 13$ , to be  $3.1 \times 10^{-14}$  and  $4.4 \times 10^{-14} \text{ cm}^3/\text{sec}$ , respectively. However, these rate constants are still lower than the respective values for CO<sub>2</sub>, and thus, since the concentration of beam produced O<sub>2</sub> must be less than one half that of CO, the previous limits specified for the CO concentration will be more than ample in precluding any undesired relaxation due to reaction (51).

The last consideration is to the possible V-T deactivation of CO by oxygen and nitrogen atoms. Little kinetic information is available on these processes. Center<sup>31</sup> has measured the rate constant for V-T deactivation of CO ( $v = 1$ ) by O-atoms at high temperatures. An extrapolation of his results to room temperature would result in a rate constant of  $10^{-15} \text{ cm}^3/\text{sec}$ . It would be expected that this rate constant would increase with increasing vibrational level, perhaps being a few orders of magnitude larger by  $v = 13$ . Since the oxygen atom concentration will perforce be less than or equal to the CO concentration, the previously defined CO density limit would also seem to be sufficient to rule out any significant vibrational relaxation resulting from the presence of oxygen atoms.

30. Miller, D.J., and Millikan, R.C. (1974) Chem. Phys. Letters 27:10.

31. Center, R.E. (1973) J. Chem. Phys. 58:5230.

In conclusion, it was found that the experimental conditions have to be reconfigured to reduce the concentration of beam produced species within the test chamber by at least two orders of magnitude. This could be achieved in a number of ways (a) decrease the gas residence time, (b) decrease the beam duty cycle, (c) work with thin rather than thick gas targets, and (d) decrease the beam current. Several of these steps were taken simultaneously in order to develop a new data base which would provide the desired kinetic information. The analysis of this data is described in the next two sections.

### 3. CO DATA ANALYSIS

A number of steps were taken in order to attain the desired experimental operating conditions. The most prominent of these were the removal of the gold coated integrating sphere, which had provided the limiting impedance to the gas flow, and the opening of a secondary pumping port. A flow meter was also added to the system, in order to better determine the gas residence time, and alcohol/dry ice traps were implemented to reduce test gas impurities. A series of runs were then performed in "thin target" mixtures of Ar/CO<sub>2</sub>, this mixture being considered the most straightforward to analyze based upon the considerations discussed in Section 2. Fluorescence measurements, with optical resolution of 10 cm<sup>-1</sup>, were performed for an argon pressure of 9 torr and nominal CO<sub>2</sub> pressures of 0.1, 0.25, 0.5, and 1.0 torr respectively. The beam conditions were: current of 0.3 to 0.9 mA, voltage of 30 kV, and pulse time of 2.4 msec with a duty cycle of  $\approx 10$  percent. The gas pumping rate within the test chamber was measured to be five standard liters/min.

#### 3.1 Irradiated Gas Properties

The distribution of beam-produced species for one of these cases,  $P_{\text{CO}_2} = 1/4$  torr and  $I = 0.9$  mA, will be worked out in detail in order to demonstrate that local concentrations of cold CO are sufficiently low so as not to interfere with the CO vibrational relaxation.

R. Center<sup>32</sup> has studied the growth behavior of a well collimated electron beam as a function of target thickness. His observation, for the case of thin N<sub>2</sub> and Ar targets, was that the beam current distribution was apparently Gaussian about the beam axis. Center<sup>32</sup> defined a parameter  $\theta_{1/2}$ , which is the angle, as measured from beam origin, at which one half of the total beam current is encompassed. He found that this quantity could be adequately represented by a relationship of the form

32. Center, R.E. (1970) Phys. Fluids 13:79.



$$\theta_{1/2} = \frac{A(Nl)^{3/2}}{1 + B(Nl)} \quad (52)$$

where  $N$  is gas number density,  $l$  is the distance from beam origin and the quantities  $A$  and  $B$  are both gas and beam voltage specific.

The values of the quantities  $A$  and  $B$ , as determined by Center, are shown in Table 7. These values have been used to predict the expected half-beam radius at the end of the test chamber, which has a length of 16 cm. These predictions are shown in Figure 13, where an initial beam radius of 0.05 cm has been applied. The vertical dashes in Figure 13 represent the largest line densities for which Center made measurements. As can be seen the beam radius is largest at low voltages and high line densities,  $Nl$ , and the beam grows more rapidly in Ar than in  $N_2$ . (Note that the radii shown can be scaled to other positions in the test chamber by dividing by 16 cm and multiplying by the appropriate length.) The total volume within the test chamber irradiated in a single pulse has been estimated, to first order, by assuming the beam growth to be linear (this is an overestimate). The resulting volume predictions for the cases of Figure 13 are shown in Figure 14. (It is to be remembered that this is only the volume in which one half the beam current is located.) As can be seen at low voltages and moderate line densities, these volumes can be several hundred  $\text{cm}^3$ . In comparison, the thick target "diffusion" volume estimated in Section 2.2 was only one thousand  $\text{cm}^3$ . One important distinction between the two cases is, however, that in the case of a thin target, only a small portion of the beam energy is deposited in the irradiated volume.

Table 7. Beam Growth Parameters

Gas	Beam Voltage kV	$A \times 10^{28}$ $\text{cm}^3$	$B \times 10^{18}$ $\text{cm}^2$
$N_2$	20	4.00	2.94
$N_2$	40	1.00	1.43
$N_2$	100	0.262	0.87
Ar	40	2.36	2.08
Ar	100	0.58	1.19

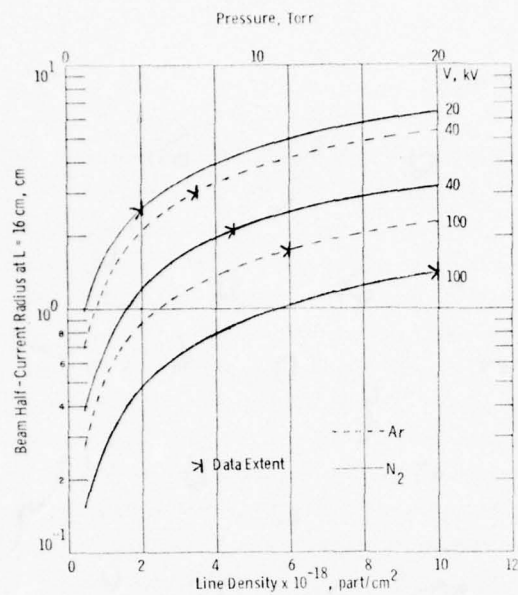


Figure 13. Electron Beam Half Current Radius at  $L = 16$  cm, vs Gas Target Line Density

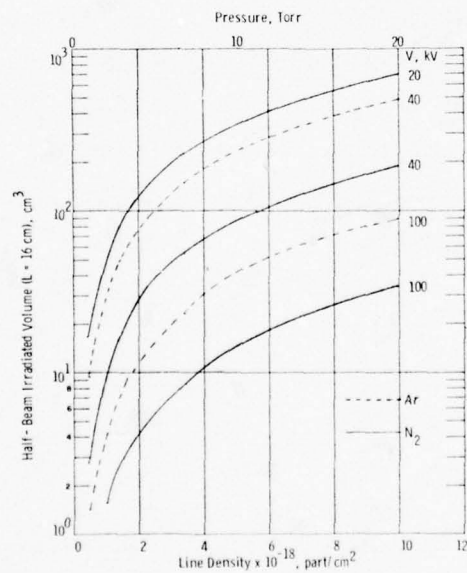


Figure 14. Electron Beam Irradiated Volume in a 16 cm Chamber vs Gas Target Line Density

An extrapolation of Center's measurements may be used to estimate the beam dimensions for the case of interest, corresponding to a beam voltage of 30 kV and a dominantly argon mix. The appropriate extrapolated constants for a beam voltage of 30 kV are  $A = 4 \times 10^{-28} \text{ cm}^3$  and  $B = 2.7 \times 10^{-18} \text{ cm}^2$ . The interferometer is situated approximately 30 cm from the test chamber window and has a circular field of view of radius 4.1 cm at chamber center. The center of the field of view is situated 8 cm downstream of the electron beam entrance and thus will encompass the beam over a distance from 4-12 cm downstream of the beam origin. The half beam radius,  $r_{1/2}$ , as defined by Eq. (52) and a target number density of  $3 \times 10^{17}/\text{cm}^3$ , will vary significantly across the field of view, having values of 0.5, 1.6, and 3.06 cm at distances of 4, 8, and 12 cm respectively. This beam growth is shown schematically in Figure 15 where the quantities  $r_{1/2}$  and  $2r_{1/2}$  are displayed from beam origin to the end of the field of view. It can be shown from Figure 15 that approximately 90 percent of the beam current distribution between 3.9 and 12.2 cm will fall within the field of view.

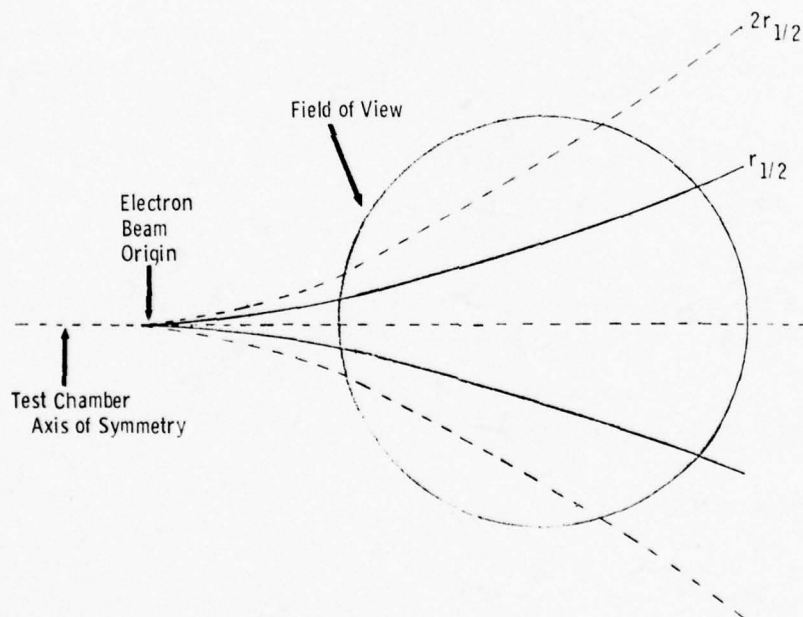


Figure 15. Schematic of Beam Current Distribution Within Field of View. Scale 1:1

Now that the beam current distribution is defined spatially, local beam species production rates may be defined. These will, of course, vary across the field of view and numerical examples will only be provided for  $l = 8$  cm, corresponding to the center of the field of view. The local ion pair creation rate per unit volume  $\alpha$  is defined by

$$\alpha = \frac{i \rho (1/\rho \, dE/dx)}{e w} \quad (53)$$

where  $\rho$  is the gas density of  $2 \times 10^{-5}$  gm/cm<sup>3</sup>,  $1/\rho \, dE/dx$  is the beam stopping power, 6.5 MeV - cm<sup>2</sup>/gm for 30 kV electrons in Ar (see Figure 8),  $w$  is the average energy required to produce an ion pair, 26.1 eV for argon,  $e$  is the unit electron charge, and  $i$  is the local current density. The local current density will be highest near the beam axis and may be defined there by

$$i = \frac{I/2}{\pi r_{1/2}^2} \quad (54)$$

where  $I$  is the total beam current, which is 0.9 mA. Combining Eqs. (53) and (54) and evaluating results in

$$\alpha = \frac{0.45 \times 10^{16}}{r_{1/2}^2}, \quad \text{cm}^{-3} - \text{sec}^{-1} \quad (55)$$

or  $\alpha = 1.76 \times 10^{15} \text{ cm}^{-3} - \text{sec}^{-1}$  at  $l = 8$  cm.

The steady state electron density is determined from the competition between the production rate  $\alpha$  and the electron recombination reaction



and may be defined by

$$n_e = \left( \frac{\alpha}{k_r} \right)^{1/2} \quad (56)$$



The rate constant  $k_r$  has been measured<sup>33, 34</sup> to be  $4 \times 10^{-7}$  cm<sup>3</sup>/sec at room temperature and may be expected to scale with electron temperature as  $T_e^{-1/2}$ . Thus, to define the electron density one must estimate the average steady state energy of secondary electrons produced by the beam. It has been shown<sup>35</sup> that the average steady state energy of electrons in N<sub>2</sub> is  $\approx 0.1$  eV. Similar modeling<sup>36</sup> for Ar at a pressure of 1 atmosphere has shown that the average secondary electron energy is  $\approx 3$  eV. This high energy is undoubtedly a result of the fact that there are no low energy,  $<10$  eV, inelastic electron-neutral processes in Ar. It is anticipated that the presence of CO<sub>2</sub> in the Ar mixture will drive the average electron energy to 0.1 eV, as predicted for N<sub>2</sub>. Thus, the appropriate electron-ion recombination rate constant to be used in Eq. (56) is estimated to be  $2.5 \times 10^{-7}$  cm<sup>3</sup>/sec. The average electron density at the center of the field of view is then

$$n_e = 0.85 \times 10^{11} / \text{cm}^3 \quad (57)$$

and the characteristic time for electron decay upon beam termination is

$$\tau_r = (k_r n_e)^{-1} = 48 \mu\text{sec} \quad (58)$$

This characteristic time is much larger than the pressure-scaled characteristic times for the ionic reactions discussed in Section 2, thus ensuring that CO<sub>2</sub><sup>+</sup> is indeed the dominant positive ion.

Lastly, the total number of CO molecules/cm<sup>3</sup> created at the center of the field of view during a beam pulse is defined as

$$[\text{CO}]_{\text{max}} = \alpha \tau_p \quad (59)$$

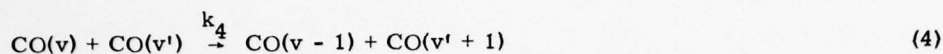
which for a pulse time of 2.4 msec has the value of  $4.2 \times 10^{12} / \text{cm}^3$ . This density corresponds to the largest possible concentration of vibrationally excited CO molecules (at  $l = 8$  cm) at any one time. (Equation (59) represents an upper bound on the concentration of vibrationally excited CO both because reaction (26) need not be 100 percent efficient in producing excited CO and also because some degree of CO vibrational relaxation will occur while the beam is on.) This maximum concentration is sufficiently low so that vibrational exchange reactions between excited CO molecules, that is

33. Weller, C.S., and Biondi, M.A. (1967) Phys. Rev. Letters 19:59.

34. Gutcheck, R.A., and Zipf, E.C. (1973) J. Geophys. Res. 78:5429.

35. Suhre, D.R., and Verdeyen, J.T. (1976) J. Appl. Phys. 47:4484.

36. Elliot, C.J., and Greene, A.E. (1976) J. Appl. Phys. 47:2946.



may be neglected. These reactions can have large rate constants when both  $v$  and  $v'$  are large. For example, it is estimated<sup>26</sup> that  $k_4 \approx 1 \times 10^{-10} \text{ cm}^3/\text{sec}$  for  $v = v' = 10$ . However, as will be shown, less than one twentieth of the excited CO molecules reside in level ten and thus the characteristic time for reaction (4)  $v = v' = 10$  is  $> 50 \text{ msec}$ . This is to be compared to the radiative decay time for this level which is  $4 \text{ msec}$ .

All the values quoted above have been for a distance of  $8 \text{ cm}$  downstream of the beam and are representative of the average gas properties within the field of view. There can, however, be a significant variation in these quantities across the field of view. For example, the values of  $\alpha$  will vary nonlinearly between  $1.8 \times 10^{16} - 4.8 \times 10^{14}$  over the range of  $l = 4 - 12 \text{ cm}$ . However, since the fluorescence measurements are integrated over the field of view, these variations will be unimportant as long as beam-produced species, such as vibrationally cold CO, do not play a role in the vibrational relaxation phenomenology. It remains then to determine the local concentrations of beam produced species which build up during the gas residence time.

The gas flow within the test chamber is somewhat complicated. The test chamber is cylindrical with length of  $16 \text{ cm}$  and radius of  $10 \text{ cm}$ . The electron beam is injected along the cylinder axis; however, the gas flow is not coaxial. Gas is injected from a port on the cylinder sidewall situated  $5.5 \text{ cm}$  from the beam origin, or alternately,  $2.5 \text{ cm}$  from the center of the field of view. There is a secondary pumping source at the beam origin; however, the primary pumping source is near the rear of the chamber on the same cylinder sidewall as the gas injection port. Thus gas flowing downstream need not remain on axis and, therefore, gas irradiated by one pulse may no longer be within the radius of the field of view when the beam is pulsed again. Furthermore, the quasistagnant gas between the beam origin and the gas injection port is not expected to flow within the field of view. These statements cannot be firmed up without a detailed fluid dynamical analysis which is beyond the scope of the present effort.

For purposes of calculation, it will be assumed that the gas residence time may be defined in terms of the time it takes to traverse the field of view at the average gas velocity. This latter quantity may be deduced to be  $25 \text{ cm/sec}$  from the known flow rate of  $5 \text{ st. liters/min}$ , and thus the time to traverse the field of view is  $0.33 \text{ sec}$ . During this time the beam would be pulsed 13 times and therefore, on the average, gas within the field of view will have been irradiated by seven pulses. The number of CO molecules created in one pulse, over a length  $l$ , is defined by

$$CO_{tot} = \frac{\rho(1/\rho \, dE/dx) I \ell \tau_p}{e w} \quad (60)$$

or for the present case with a pulse time of 2.4 msec, current of 0.9 mA, and length of 8.2 cm

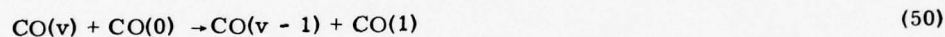
$$CO_{tot} = 5 \times 10^{14} \quad (61)$$

Thus, the total number of cold CO molecules within the field of view at one time will be  $3.5 \times 10^{15}$ . Neglecting diffusion, one half of these CO molecules would be within the gas volume defined by

$$v = \int_{3.9}^{12.2} \pi r_{1/2}^2 d\ell \approx 110 \text{ cm}^3 \quad (62)$$

where Eq. (52) has been applied. Thus, the average concentration of cold CO within the beam half current volume is  $1.6 \times 10^{13}/\text{cm}^3$ . The total beam irradiated volume, defined by the contour  $2 r_{1/2}$ , is  $440 \text{ cm}^3$  and the average cold CO concentration in this region would be  $0.8 \times 10^{13}/\text{cm}^3$ .

This density of cold CO is sufficiently large so that the reaction



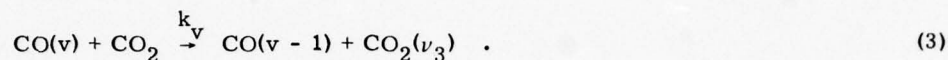
could contribute a 10 percent effect to the relaxation of individual vibrational levels of CO (see the discussion in Section 2) and is somewhat larger than desirable. However, given the uncertainty in the test chamber flow properties and the neglect of diffusion effects (the characteristic diffusion length being 2 cm in 0.3 sec), the estimated cold CO concentration is most probably an upper bound. A test of the effect of cold CO could be provided by observing the relaxation behavior of two cases having the same experimental conditions, but with beam currents differing by a factor of  $\sim 3$ . Such a test has not been performed during the present reporting period.

The last quantity to be determined is the temperature increase in the gas caused by beam heating. The average energy added per  $\text{cm}^3$  during the gas residence time is specified by the product of the average cold CO concentration and the energy required to create an ion pair,  $w$ . The average energy added in the beam irradiated volume is then  $3.3 \times 10^{-5} \text{ J/cm}^3$  which could result in a  $3^\circ\text{K}$  increase in gas temperature. The temperature increase within the half beam

irradiated volume, the hottest portion of the gas, would be 6°K. These minimal temperature increases should have no effect on the data analysis.

### 3.2 Data Reduction

Although the predicted cold CO concentration is marginal, the data should be sufficient to allow determination of the rate constants for the process



The raw data is fluorescent radiation arising from the fundamental vibration/rotation band of CO. The first step in the data analysis is to deduce the time dependent vibrational population histories from these spectra. Since the vibrational distributions are nonBoltzman, this step requires an iterative comparison between the data and artificially generated spectra. Such comparisons can be greatly simplified through the use of nonlinear regression analysis, which can essentially provide the equivalent of a least squares curve fit to the data.

This technique involves the generation of a set of "basis functions"  $\xi_v(\nu)$ , where  $\nu$  is wavenumber, which are essentially the spectra arising from the individual vibrational transitions,  $v \rightarrow v-1$ . These spectra, having been properly convoluted over the optical detection system slit function, may be related to the observed intensity at any wavenumber by the relation

$$I_p(\nu) = \sum_v n_v \xi_v(\nu) \quad (63)$$

where the quantities  $n_v$  are proportional to the CO population in level  $v$ . Given the data  $I(\nu)$  and the functions  $\xi_v(\nu)$ , defined over some wavenumber interval, the quantities  $n_v$  may be determined by requiring that the square of the differences  $(I_p(\nu) - I(\nu))$  be minimized. A computer code has been developed to perform this task which takes the data and basis functions as input and provides the relative vibrational populations as output.

A computer code also was developed to generate the basis functions, which are a function of both temperature and the system slit function. The intensity of an individual vibrational/rotational transition of a diatomic molecule with zero angular momentum, such as CO, is defined by the relationship<sup>37</sup>

37. Herzberg, G. (1951) Molecular Spectra and Molecular Structure I. Spectra of Diatomic Molecules, 2nd edition, D. Van Nostrand Co., New York.



$$I_{J \rightarrow J \pm 1}^{v \rightarrow v-1} = \frac{hc \nu_{v \rightarrow v-1, J \rightarrow J \pm 1}^4 S_{J \rightarrow J \pm 1} A_{v \rightarrow v-1}}{(2J+1) \nu_{v \rightarrow v-1}^3} N_{v, J} \quad (64)$$

where the vibration/rotation interaction factor has been taken to be unity. In Eq. (64)  $h$  is Planck's constant,  $c$  is the speed of light,  $S_{J \rightarrow J \pm 1}$  is the Hönl - London factor,  $A_{v \rightarrow v-1}$  is the Einstein coefficient,  $J$  is the rotational quantum number,  $\nu_{v \rightarrow v-1, J \rightarrow J \pm 1}$  is the line center wavenumber of the transition,  $\nu_{v \rightarrow v-1}$  is the wavenumber of the band origin, and  $N_{v, J}$  is the population of the radiating state. The quantity  $N_{v, J}$  may be rewritten<sup>37</sup>

$$N_{v, J} = N_v \frac{hc B_v}{kT} (2J+1) \exp(-F(v, J) hc/kT) \quad (65)$$

where  $B_v$  is the rotational constant for vibrational level  $v$ , defined as

$$B_v = B_e - \alpha_e (v + 1/2) \quad (66)$$

and

$$F(v, J) = J(J+1) B_v - D_e J^2 (J+1)^2 \quad (67)$$

The various line and band origin wavenumbers in Eq. (64) may be determined from the definition of the energy of a given  $v, J$  state,<sup>37</sup> that is,

$$E_{v, J} = w_e (v + 1/2) - w_e x_e (v + 1/2)^2 + w_e y_e (v + 1/2)^3 + B_v J(J+1) - D_e J^2 (J+1)^2 \quad (68)$$

Finally, the Hönl - London factors are defined as<sup>37</sup>

$$\begin{aligned} S_{J \rightarrow J-1} &= J & \text{R branch} \\ S_{J \rightarrow J+1} &= J+1 & \text{P branch} \end{aligned} \quad (69)$$

The intensity of a given  $v, J \rightarrow v-1, J \pm 1$  transition per vibrationally excited molecule, that is,  $I_{J \rightarrow J \pm 1}^{v \rightarrow v-1} / N_v$ , may be defined from Eqs. (64)-(69) once the Einstein coefficients are defined. Predictions for the Einstein coefficients for the

CO fundamental and first overtone bands as performed by Young and Eachus<sup>38</sup> and by Docken<sup>39</sup> are shown in Figure 16. As can be seen, the difference between the two predictions is small and the results of Docken<sup>39</sup> have been used in the present analysis. It is of interest to note that the results of Figure 16 are closely approximated by the relationship

$$A_{v \rightarrow v-1} = VA_{10} \left( \frac{w_e - 2v w_e x_e}{w_e - 2w_e x_e} \right)^3 \quad (70)$$

The line intensities were evaluated utilizing the most accurate definition of the spectroscopic constants of CO available.<sup>40</sup> The values used, in  $\text{cm}^{-1}$ , are  $w_e = 2169.812$ ,  $w_e x_e = 13.289$ ,  $w_e y_e = 1.059 \times 10^{-2}$ ,  $B_e = 1.93127$ ,  $\alpha_e = 1.7459 \times 10^{-2}$ , and  $D_e = 5.6268 \times 10^{-6}$ . The intensities were integrated over the system slit function  $g(\nu, \nu')$  in order to define the basis functions  $\xi_v(\nu)$ . Since the transitions are at discrete points, the integral becomes a sum defined by

$$\xi_v(\nu) = \frac{1}{n_v} \sum_J g(\nu, \nu_{v \rightarrow v-1, J \rightarrow J \pm 1}) I_{J \rightarrow J \pm 1}^{v \rightarrow v-1}(\nu_{v \rightarrow v-1, J \rightarrow J \pm 1}) \quad (71)$$

The slit function for the system interferometer was a sinc function defined by

$$g(\nu, \nu') = \frac{0.82\Delta\nu}{\pi(\nu - \nu')} \sin \left( \frac{\pi(\nu - \nu')}{0.82\Delta\nu} \right) \quad (72)$$

where  $\Delta\nu$  is the data spectral resolution of  $10 \text{ cm}^{-1}$ .

The basis functions  $\xi_v(\nu)$  were generated for a temperature of  $300^\circ\text{K}$  and used to fit the data. Typical data for the case  $\text{PCO}_2 = 1/4 \text{ torr}$ ,  $I = 0.9 \text{ mA}$  are shown in Figure 17. These spectra were taken after beam termination at times of 3, 4, 5 and 6 msec in order of decreasing intensity, respectively. For purposes of reference, it is noted that the  $v = 1 \rightarrow 0$  band origin is at  $2143 \text{ cm}^{-1}$  and the  $v = 10 \rightarrow 9$  band origin is at  $1900 \text{ cm}^{-1}$ . It can be seen that the data is quite noisy. The signal to noise ratio is particularly bad below  $1850 \text{ cm}^{-1}$ , corresponding to the spectral region of decreasing detector response. Thus, although spectral data is available over the band region of the first 14 vibrational levels of CO, only 11 - 12 vibrational levels are sufficiently well defined to allow evaluation of their population densities.

38. Young, L.A., and Eachus, W.J. (1966) *J. Chem. Phys.* 44:4195.

39. Docking, K.K. (1976) Unpublished results.

40. Schiffner, G., and Klement, E. (1975) *Appl. Phys.* 6:199.

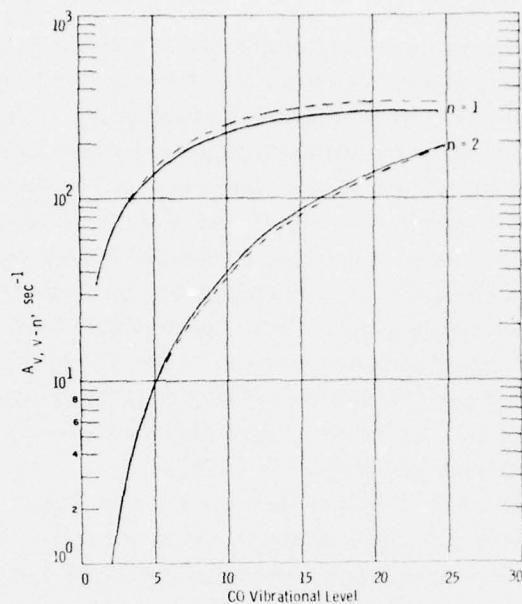


Figure 16. Predicted Einstein Coefficients for the Fundamental and First Overtone Bands of CO (— ref. 38, ---- ref. 39)

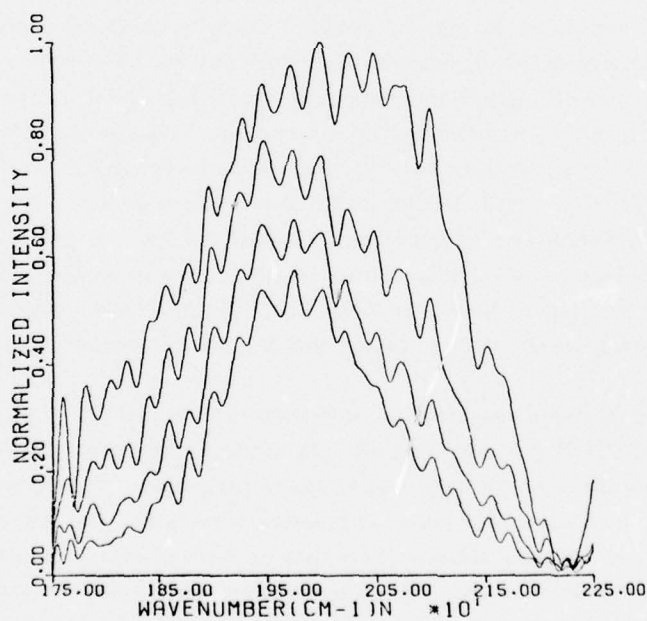


Figure 17. Normalized Intensity at Times of  $t = 3, 4, 5$  and  $6$  msec in Order of Decreasing Intensity, Respectively.  $P_{CO_2} = 1/4$  torr,  $I = 0.9$  mA

Curve fits of the data were first performed in steps of 0.4 msec between the time interval of 2.6-8.2 msec. The beam is off during this time scale and, therefore, the data may be interpreted in terms of reaction (3). Typical comparison between the data and curve fits at different times are shown in Figures 18-23. The sequence of curves at the bottom of each figure are the individual basis functions and indicate the contribution of each vibrational level to the total intensity. As can be seen, the comparison between data and prediction is quite reasonable. In particular, the predicted spectra in the region of the lowest vibrational levels is in very close conjunction with the data. This is particularly true in Figures 18 and 19 which exhibit the largest densities of the  $v = 1$  and 2 levels. The intensity slope in the region  $2120\text{--}2220\text{ cm}^{-1}$  is due predominantly to the R branches of  $v = 2 \rightarrow 1$  and  $v = 1 \rightarrow 0$  transitions, and the good agreement between data and prediction confirm that the CO rotational temperature is  $\approx 300^\circ\text{K}$ .

The comparison between data and prediction is not as good in the lower wavenumber region,  $\leq 1900\text{ cm}^{-1}$ , although the curve fit envelopes the data fluctuations quite well. Severe noise fluctuations are evident in all the data below  $\approx 1840\text{ cm}^{-1}$ . Any errors in the magnitude of the basis functions in this wavenumber region tend to propagate to higher wavenumbers because of the large overlap between the basis functions. An attempt to improve the fits by truncating the data at  $1840\text{ cm}^{-1}$  failed. The reason for this is that the magnitude of the basis functions in this region are overestimated by the fit, because there is an actual contribution to the intensity in this region due to higher vibrational levels. The effect of this overestimate propagates to higher wavenumbers causing an underestimate of the magnitude of the basis functions centered in that region. It has been found that the curve fitting technique is quite accurate if the band spectra is closed, that is, if the intensity decays to zero at both high and low wavenumber edges of the band. Unfortunately, the noise level is sufficiently high in the low wavenumber range of interest to preclude a reasonable extrapolation to zero intensity. In any event, it is felt that the population densities of the first 12 vibrational levels of CO can be well determined from the curve fits and that the densities of higher levels are minimal.

It can be seen from examination of Figures 18-23 that the high and low vibrational levels of CO decay more rapidly than those at the center, that is, with increasing time the spectra collapses towards its center. This behavior is manifested in Figure 24 where the deduced relative vibrational population distribution is shown at three different times. Note that there is a total population inversion in the region of levels 5-9 and that the populations of levels 7-9 vary only slightly. On the other hand, significant decreases in the population of higher and lower levels can be observed. The time dependent histories of the relative vibrational populations



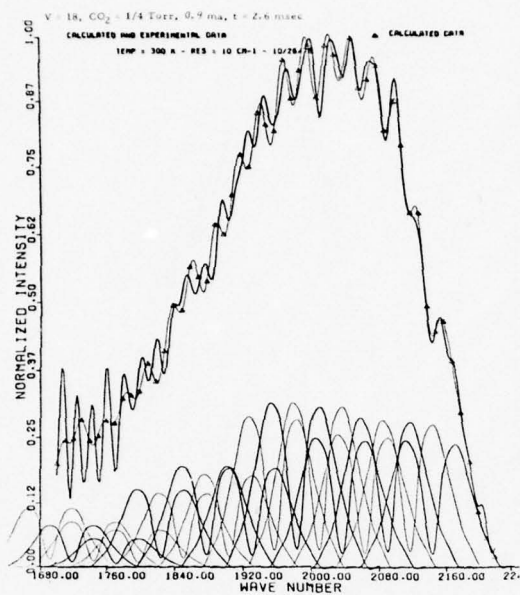


Figure 18. Synthetic and Measured Spectra at  $t = 2.6$  msec

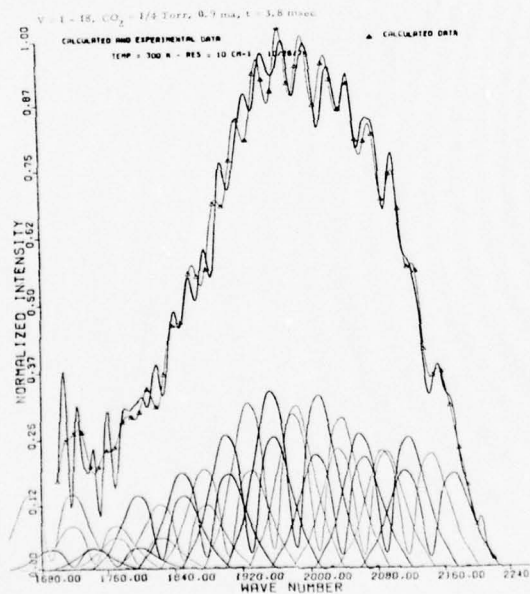


Figure 19. Synthetic and Measured Spectra at  $t = 3.8$  msec

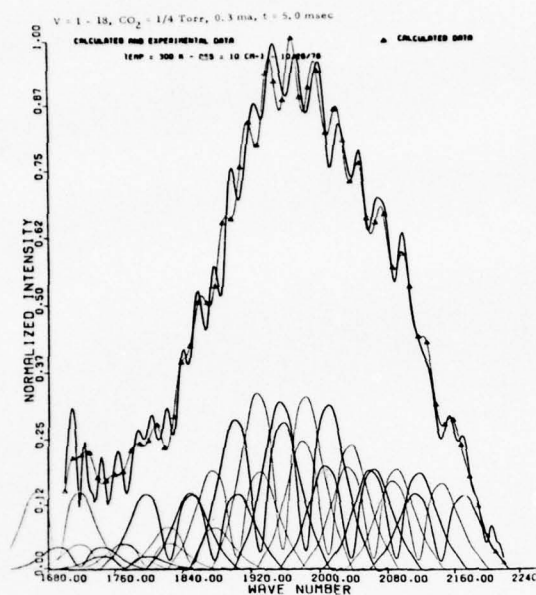


Figure 20. Synthetic and Measured Spectra at  $t = 5.0$  msec

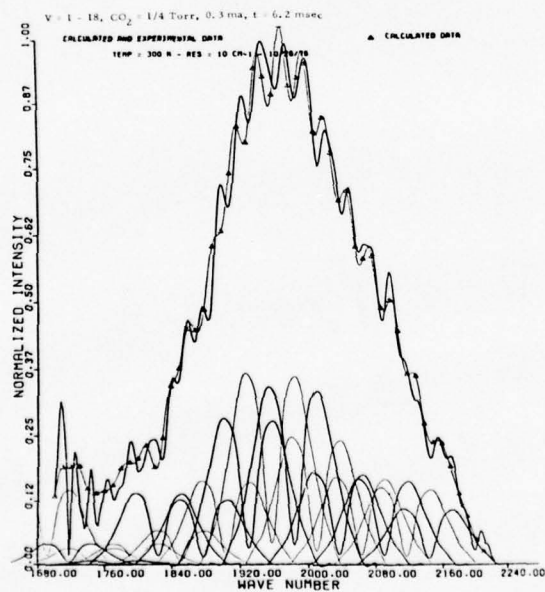


Figure 21. Synthetic and Experimental Spectra at  $t = 6.2$  msec

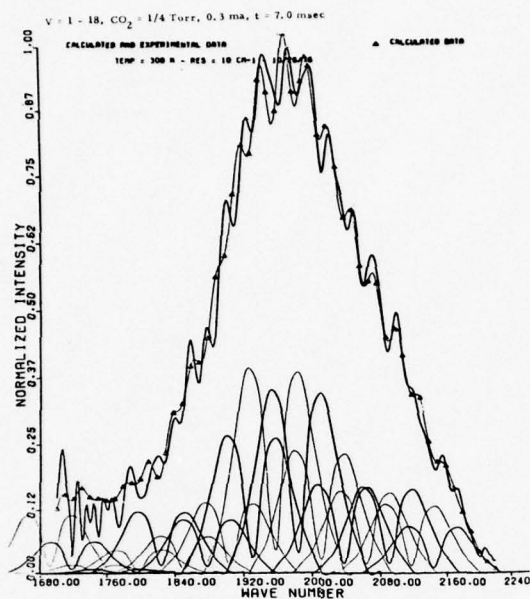


Figure 22. Synthetic and Measured Spectra at  $t = 7.0$  msec

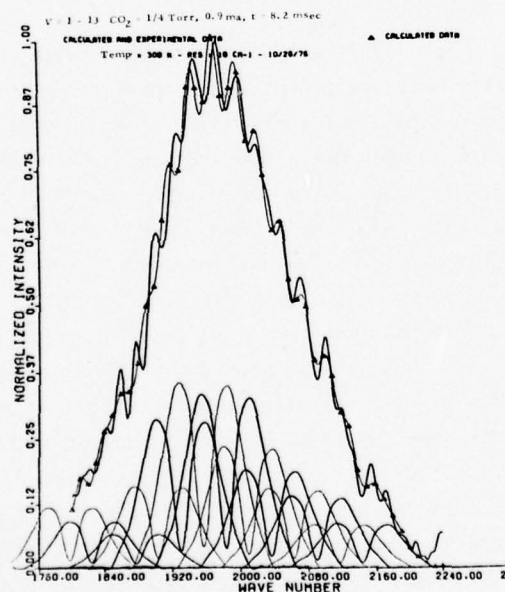


Figure 23. Synthetic and Experimental Data at  $t = 8.2$  msec

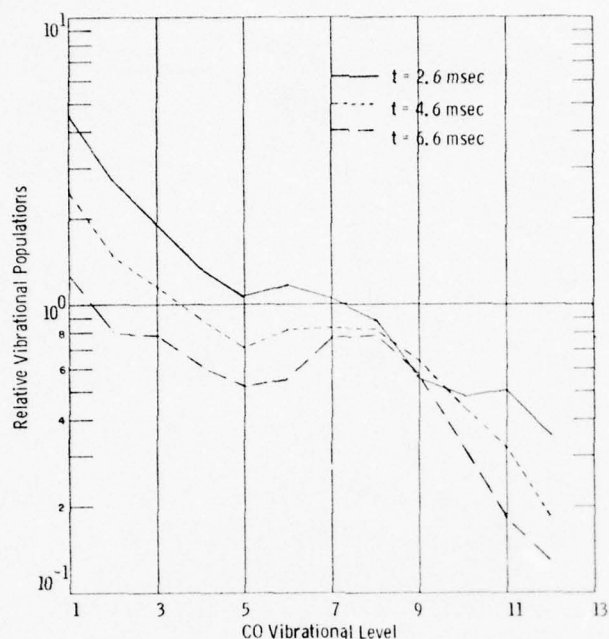


Figure 24. Deduced Relative Vibrational Population Distribution at Three Different Times.

$P_{CO_2} = 1/4$  torr,  $I = 0.9$  mA

are shown in Figures 25 and 26. These densities were deduced at time intervals of 0.4 msec and have been arbitrarily connected by straight lines. As can be seen in Figure 25, the first five levels of CO relax smoothly, exponentially to first order, with the fluctuations at the longer times due most probably to the lower signal to noise ratio (S/N) as observed in Figures 22 and 23. The time histories for vibrational levels 6-12, as shown in Figure 26, are more complicated. Considering first the highest vibrational levels, it can be seen that the observed vibrational relaxation times decrease with increasing vibrational level for levels  $v = 10-12$ . The results for level 12 are marginal since the band origin for the  $v = 12 \rightarrow 11$  transition is at  $1846 \text{ cm}^{-1}$ , or about the point where the signal to noise fluctuations become quite large, and it is felt that the populations for this level, for times  $\geq 6$  msec, are misleading and should be ignored. The behavior of level 9 is quite distinct from that of levels 10-12, and in fact the population of this level actually increases over the time interval 2.6-5.0 msec. Furthermore, the concentration of levels 7 and 8 remain relatively constant over the time interval shown (and beyond) although the population of level 6 drops by a factor of two.



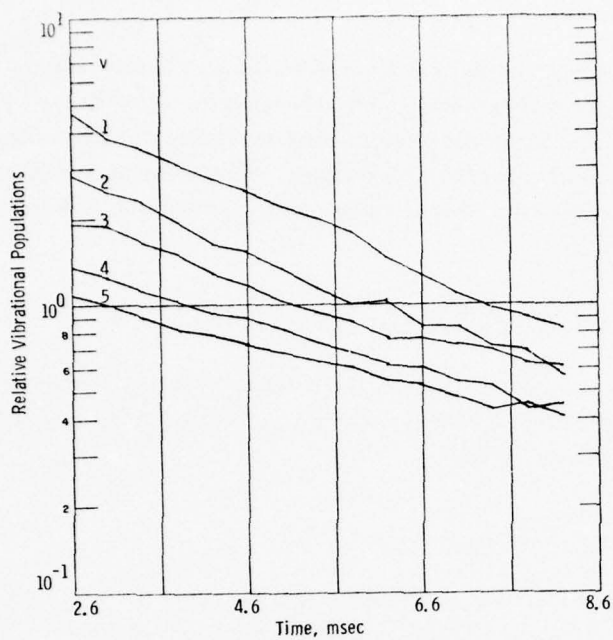


Figure 25. Deduced Time Histories of the Relative Populations of the First Five Levels of CO.  $P_{\text{CO}_2} = 1/4$  torr,  $I = 0.9$  mA

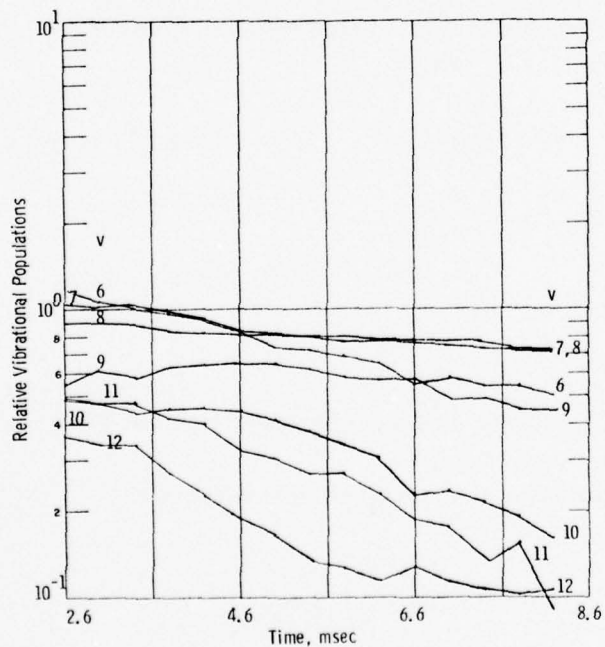


Figure 26. Deduced Time Histories of the Relative Populations of Levels  $v = 6-12$  of CO.  $P_{\text{CO}_2} = 1/4$  torr,  $I = 0.9$  mA

These observations imply that levels 7-9 act as a bottleneck for efficient relaxation of vibrationally excited CO in this system. This behavior can best be interpreted through an analysis of the kinetic mechanisms controlling the relaxation phenomena. In the absence of intramode vibrational exchange collisions — that is, processes (4) — the master equations for relaxation of vibrationally excited CO may be written as

$$dn_v/dt = R_{v+1} n_{v+1} - R_v n_v + A_{v+2 \rightarrow v} n_{v+2} - A_{v \rightarrow v-2} n_v \quad (73)$$

for  $v = 1 \rightarrow v_{\max}$ . In Eq. (73),  $n_v$  is the relative population of level  $v$ ,  $A_{v+2 \rightarrow v}$  is the Einstein coefficient for first overtone radiative transitions, as shown in Figure 16, and  $R_v$  is defined as

$$R_v = k_v(\text{CO}_2) + A_{v \rightarrow v-1} \quad (74)$$

where  $k_v$  is the rate constant for reaction (3),  $(\text{CO}_2)$  is the  $\text{CO}_2$  number density in particles/ $\text{cm}^3$ , and  $A_{v \rightarrow v-1}$  is the Einstein coefficient for fundamental band radiative transitions. The unknown quantities in Eq. (73) are the  $k_v$ 's and the derivatives,  $dn_v/dt$ . In theory, the derivatives could be determined from the predicted time variation in  $n_v$ ; however, in practice this technique is not tractable because of the uncertainties in the predicted  $n_v$ 's. Therefore, Eq. (73) has been used in its time integral form which may be written

$$n_v(t_2) - n_v(t_1) = a_{v+1} R_{v+1} - a_v R_v + A_{v+2 \rightarrow 2} a_{v+2} - A_{v \rightarrow v-2} a_v \quad (75)$$

where

$$a_v = \int_{t_1}^{t_2} n_v dt \quad (76)$$

Since the values of  $a_v$  can be determined directly from the data, the quantities  $R_v$  may be deduced from Eq. (75).

This determination can be simplified by the fact that

$$\sum_{v=1}^{\infty} (n_v(t_2) - n_v(t_1)) = -a_1 R_1 - A_{2 \rightarrow 0} a_2 \quad (77)$$

which can be shown directly from Eq. (75). Equation (77) simply states that the decrease in the population of vibrationally excited CO can only occur through vibrational deactivation of level 1 and first overtone radiation from level 2 (radiation from higher overtones being negligible). Once the quantity  $R_1$  is defined, the remaining  $R_v$ 's can be determined through the relationship

$$\sum_{v=1}^{n-1} (n_v(t_2) - n_v(t_1)) = -a_1 R_1 - A_{2,0} a_2 + a_n R_n + A_{n+1 \rightarrow n-1} a_{n+1} \quad (78)$$

The complication in using Eqs. (77) and (78) is that the system of equations is not closed; that is, relaxation data is only available for levels  $v \leq 12$  and level 12 itself is not defined very accurately. Although the behavior of levels higher than 12 will not effect the determination of  $R_1$ , since

$$n_{12}(t_1) - n_{12}(t_2) \ll n_1(t_1) - n_1(t_2) \quad (79)$$

it will affect the determination of  $R_v$  for large  $v$ , inasmuch as these will be a small difference between two large numbers. Therefore, the values for  $R_v$  determined at higher levels,  $v \geq 9$ , must be considered as lower bounds.

The values of  $R_v$  as determined from the data of Figures 25 and 26 and Eqs. (77) and (78), are shown in Figure 27. The values shown for  $R_{12}$  has been deduced directly from the observed decay of that level. Also shown for comparison are the values of the Einstein coefficient  $A_{v \rightarrow v-1}$ . The  $R_v$ 's shown have been evaluated for three different time intervals, as shown. The largest time interval is to be preferred inasmuch as this case will minimize the effect of uncertainties in the data. Similar results are obtained if  $t_1$  is taken to be 3 msec. It would appear from the data of Figure 27 that one unique set of  $R_v$ 's is consistent with the relaxation observations. (The differences in the  $R_v$ 's determined at different time intervals are only pronounced at large  $v$  and these are most affected by small variations, as discussed earlier.)

It is also evident from Figure 27 that the rate constants  $k_v$  cannot be determined with any accuracy for levels  $v = 8, 9$ . This is because  $R_v \approx A_{v \rightarrow v-1}$  for these levels and the rate constant  $k_v$  is proportional to the difference between  $R_v$  and  $A_{v \rightarrow v-1}$  (see Eq. (74)). Furthermore, the  $R_v$ 's for levels  $v = 7$  and 10-12 are all within a factor of two of the respective values of  $A_{v \rightarrow v-1}$ . Coupling this observation with the fact that the values shown for  $R_v$  at the higher levels are lower bounds — because the effect of levels higher than  $v = 12$  has not been included in the analysis — it is clear, that the uncertainty in the rate constants for these levels will also be high.

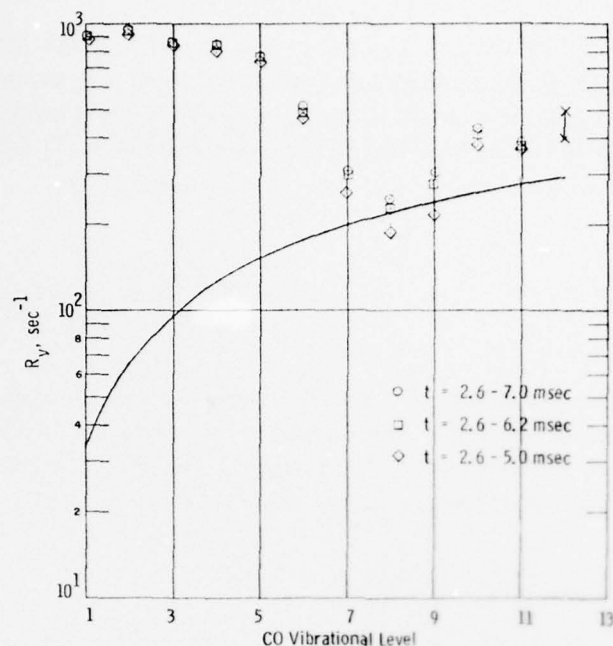


Figure 27. CO(v) Vibrational Relaxation Rate for  $P_{\text{CO}_2} = 1/4$  torr,  $I = 0.9$  mA. —,  $A_{v \rightarrow v-1}$ ; x, lower bound from data

The nominal  $\text{CO}_2$  pressure for this case is  $1/4$  torr; however, it is uncertain to  $\approx 50$  percent. The exact  $\text{CO}_2$  pressure has been determined from the data by setting  $k_1$  equal to its known value as shown in Figure 10. The  $\text{CO}_2$  pressure determined in this manner was  $1/3$  torr. This pressure and the measured values of  $R_v$  were then used to evaluate  $k_v$  through use of Eq. (74). These results are shown in Figure 28 for the three time intervals used. Also shown are the results of Hancock and Smith.<sup>24</sup> As can be seen, there is a large scatter in the rate constants  $v \geq 7$ , while those for  $v < 7$  appear well defined. The rate constants for  $v < 7$  are considered to be reasonably accurate; however, they tend to be a factor of 2-3 larger than the rate constants as determined by Hancock and Smith.<sup>24</sup> On the other hand, the rate constants for  $v \geq 7$  are smaller than those of Hancock and Smith, as would be expected inasmuch as they are lower bounds. The cause of the difference between the rate constants for  $v = 4-6$  as determined in this analysis and Hancock and Smith is not understood. However, the present analysis is most accurate at low vibrational levels whereas that of Hancock and Smith is most accurate at high vibrational levels. Furthermore, although it is recognized that the presence of cold CO could cause an overestimate of the rate constants, it is unlikely



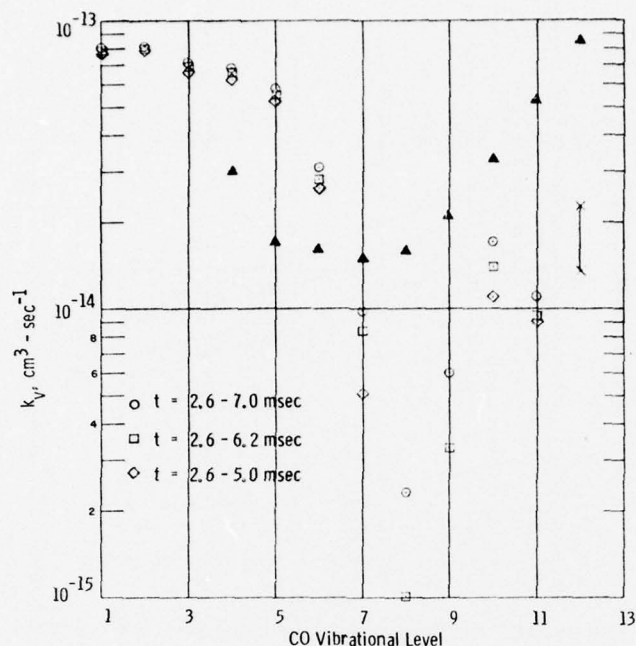


Figure 28. Measured Rate Constants for  $\text{CO}(v) + \text{CO}_2 \rightarrow \text{CO}(v-1) + \text{CO}_2(v_3)$  ○, □, ◇ : present analysis; Δ : ref. 24

that this effect could cause differences of factors of 2-3. Nonetheless, it is clear that additional cases must be reduced in order to check the consistency of the present results.

Two internal consistency checks have been performed. The first was a comparison of the measured vibrational population time histories with those predicted by solution of the differential Eq. (73), using the deduced values of  $R_v$ . The solution of these equations is also complicated by closure effects inasmuch as the population of levels  $v = 13$  and  $14$  — which are unknown — are needed for the evaluation of the differential equation for the population of  $v = 12$ . This complication has been circumvented by solving the equations for  $v = 1-11$  taking the population history of  $v = 12$  as known from the data (the effect of  $v = 13$  first overtone decay to  $v = 11$  is neglected). Furthermore, the population of  $v = 12$  was taken to continue to decay exponentially beyond  $t = 5.5$  msec inasmuch as the curve fit results are suspect at the longer times. (The value of  $R_{12}$ , as determined by this exponential decay, is  $450 \text{ sec}^{-1}$ .)

The comparison between predicted and measured time histories for the first five vibrational levels is shown in Figure 29 and can be seen to be quite good. The comparison for levels  $v = 6-11$  is shown in Figure 30. Also shown in this figure is

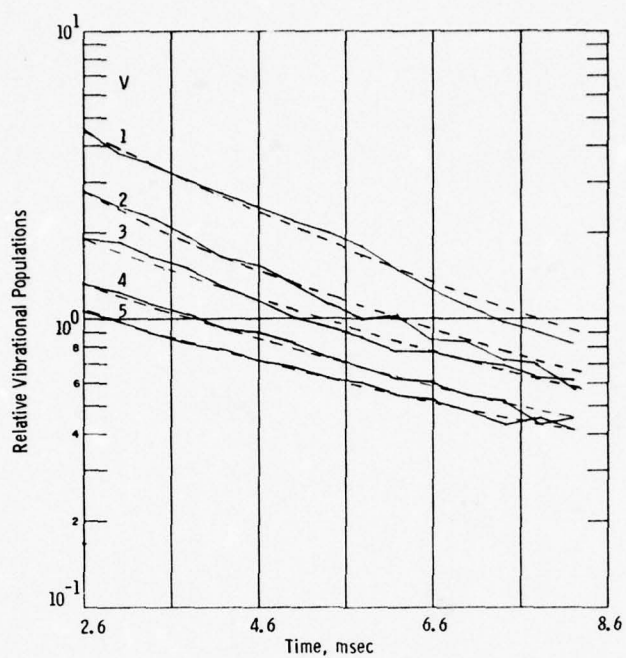


Figure 29. Comparison of Measured and Computed Vibrational Population Time Histories for  $v = 1-5$ .  
— data, --- prediction

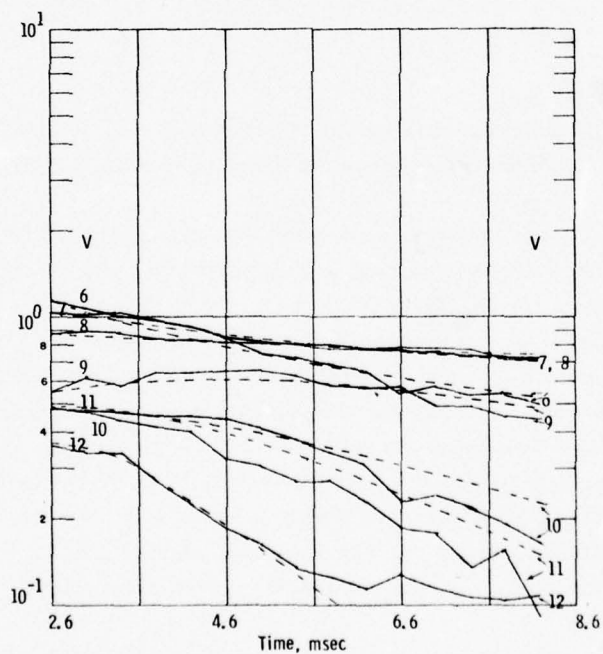


Figure 30. Comparison of Measured and Computed Vibrational Population Time Histories for  $v = 6-12$ .  
— data, --- prediction

the assumed time history of level  $v = 12$  used in the calculations. Once again the comparison between prediction and data is excellent for levels  $v = 6-9$ , with all the salient features of the data being exhibited in the predictions. The predicted time histories for levels  $v = 10-11$  decay somewhat more slowly than the data implying that  $R_{11}$  and  $R_{12}$  are somewhat higher than deduced in the prior analysis. The overall good comparison with the time dependent observations suggests that the kinetic mechanism used in interpreting the data was appropriate.

The second check involved the total vibrational energy decay in CO. The total radiation from the fundamental band is, to first order, linearly proportional to the vibrational energy content of the molecule. Therefore the experimental spectra were integrated over the spectral range of  $1760-2240\text{ cm}^{-1}$ , and this time dependent fundamental band radiation was compared to the predicted decay in vibrational energy as determined from the computer solution of Eq. (73). This comparison is shown in Figure 31 and is seen to be quite reasonable. The somewhat more rapid decay observed in the data at long times is expected inasmuch as the decay rates for higher levels were underestimated. This good comparison suggests that no serious errors developed when the experimental spectra were converted to vibrational populations.

Although it is not clear why the present measurements differ from those of Hancock and Smith,<sup>24</sup> the total single quantum deactivation rates occurring in the existing gas mix have been measured. These may then be used to analyze the fluorescence data taken while the beam was on,  $t = 0-2.4$  msec, in order to determine the production rates for vibrationally excited CO. Typical beam-on spectra along with curve fit artificial spectra are shown in Figures 32-34. These data and fits are very similar to those discussed earlier. The spectra at the lowest times are quite noisy and the curve fit predictions for  $t \leq 0.6$  msec must be considered as crude estimates. These curve fits were performed in steps of 0.2 msec for times between 0.4-2.4 msec, and the resulting relative vibrational populations are shown in Figures 35 and 36. Also shown for comparison are the previously determined vibrational populations shortly after beam termination. As can be seen in Figure 35, the populations of levels 1-5 increase monotonically while the beam is on, with populations decreasing with increasing vibrational level. The transition to vibrational decay, upon beam termination, occurs smoothly. Perhaps the most striking behavior is seen in the population histories of levels 6-12, shown in Figure 36. Here it can be seen that the population for level  $v = 9$  is less than that for  $v = 10-12$  at early times. However, near beam termination, the population of  $v = 9$  continues to increase while those of the higher levels go through a maximum.

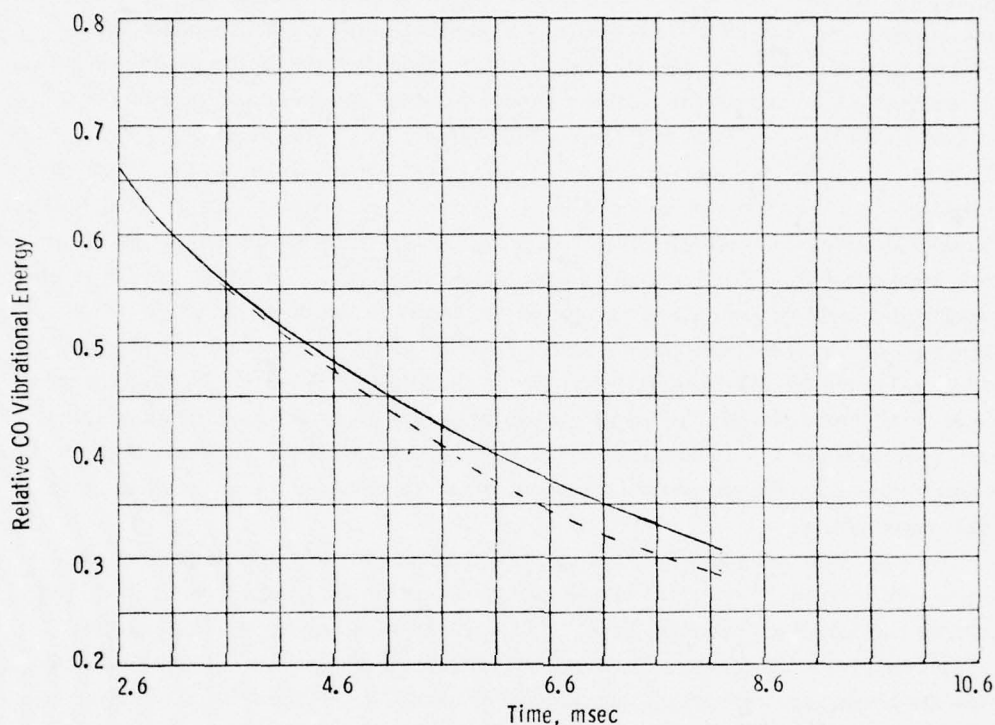


Figure 31. Comparison of Measured and Predicted CO Vibrational Energy Decay

These population histories may be analyzed in a manner similar to that used earlier for the vibrational decay data. The governing set of differential equations are

$$dn_v/dt = R_e(v) + R_{v+1} n_{v+1} - R_v n_v + A_{v+2 \rightarrow v} n_{v+2} - A_{v \rightarrow v-2} n_v \quad (80)$$

where  $R_e(v)$  is the relative rate for creation of CO molecules in vibrational level  $v$  (this rate is only relative inasmuch as the  $n_v$  are relative vibrational populations). Once again the integral form of Eq. (80) is used, that is,

$$n_v(t) = R_e(v) t + a_{v+1} R_{v+1} - a_v R_v + A_{v+2 \rightarrow v} a_{v+2} - A_{v \rightarrow v-2} a_v \quad (81)$$

where the quantities  $a_v$  are as defined in Eq. (76). Inasmuch as the quantities  $R_v$ ,  $a_v$  and  $n_v$  are known, the Eqs. (81) may be evaluated directly to determine  $R_e(v)$ .



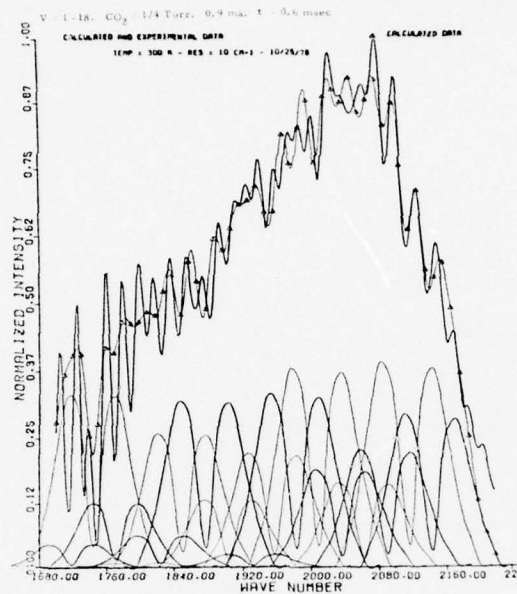


Figure 32. Synthetic and Measured Spectra at  $t = 0.6$  msec

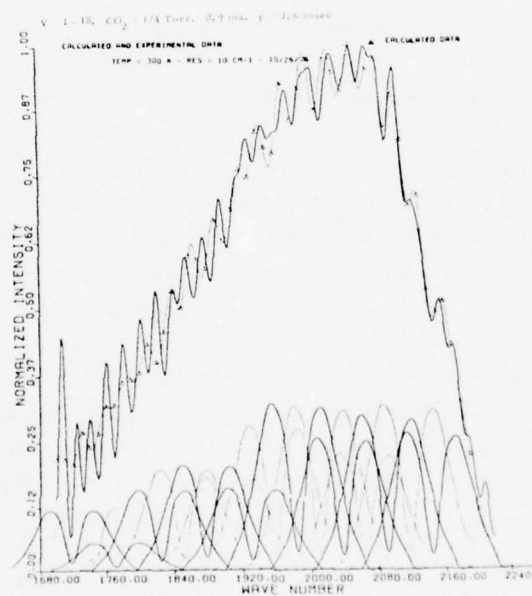


Figure 33. Synthetic and Measured Spectra at  $t = 1.6$  msec

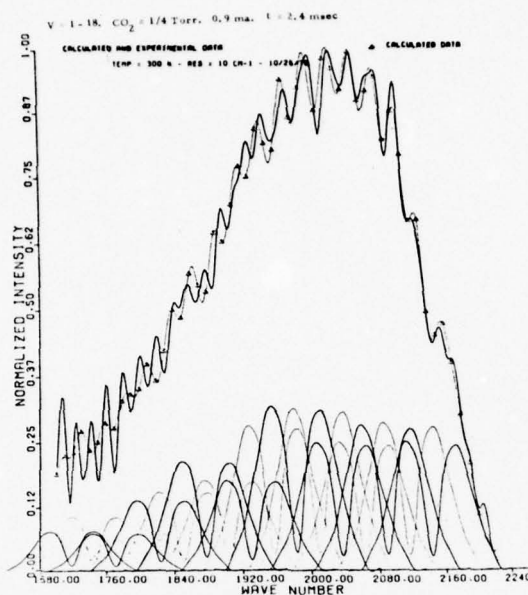


Figure 34. Synthetic and Measured Spectra at  $t = 2.4$  msec

The results for the time interval of 0-2.4 msec are shown in Figure 37. As can be seen vibrationally excited CO is created predominantly in the lower vibrational levels; however, there is a secondary peak in the rate distribution at level  $v = 6$  and the creation rate for  $v = 9$  is below those for neighboring levels. The rate for creation of  $v \approx 12$  cannot be accurately deduced from the data, given the lack of information on the populations of  $v = 13, 14$  and the uncertainty in  $R_{12}$ .

As a check on the analysis, the rates  $R_e(v)$  can be used in conjunction with Eq. (80) to compute the relative vibrational population time histories while the beam is on. Such calculations are shown, in comparison to the data, in Figures 38 and 39. The computed values for the first five vibrational levels are shown in Figure 38 and can be seen to be in excellent agreement with the data at times  $> 0.8$  msec. For times below 0.8 msec, the data for levels  $v = 3-5$  falls off more sharply than calculation; however, it is to be remembered that the data is highly inaccurate at short times (for example see Figure 32). The comparison for levels  $v = 6-11$  is shown in Figure 39 and once again the agreement between data and calculation is quite reasonable. (The Eqs. (80) were solved by taking the population of level 11 fixed by the data, with extrapolation to zero time as shown in Figure 39.)

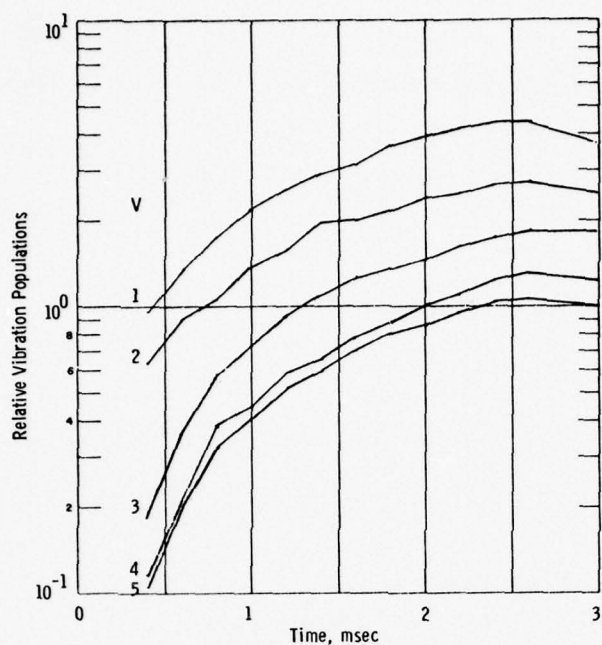


Figure 35. Deduced Time Histories of the Relative Populations of the First Five Levels of CO.  $P_{\text{CO}_2} = 1/4$  torr,  $I = 0.9$  mA beam on

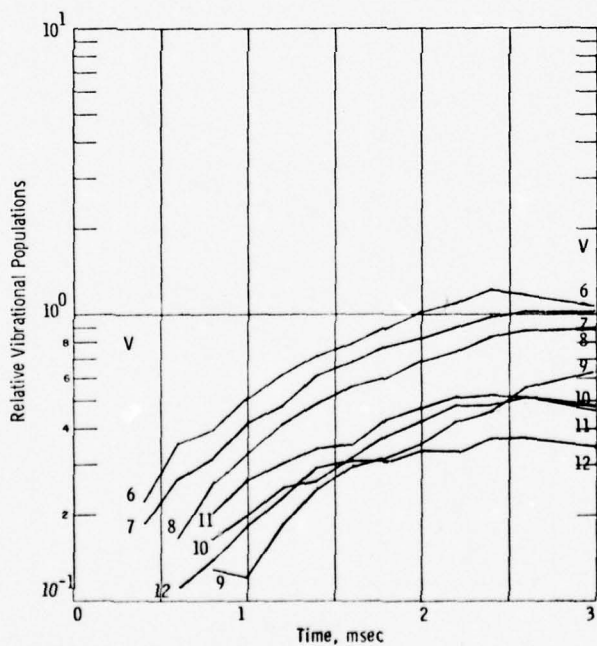


Figure 36. Deduced Time Histories of the Relative Populations of Levels  $v = 6-12$  of CO.  $P_{\text{CO}_2} = 1/4$  torr,  $I = 0.9$  mA beam on

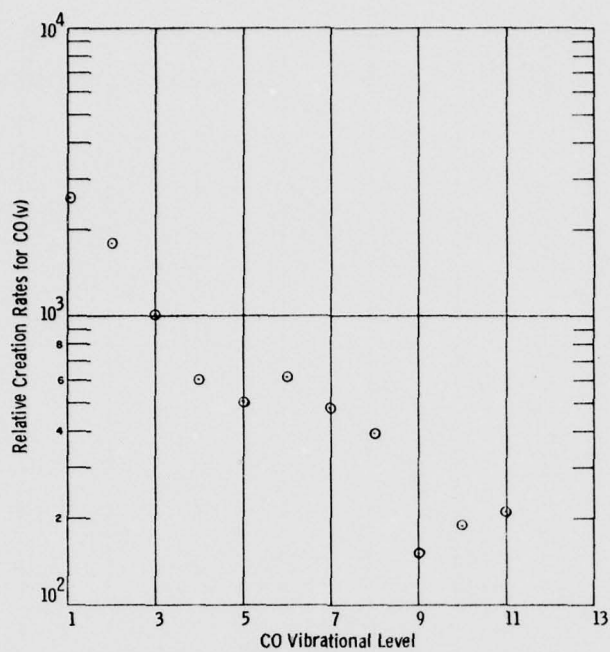


Figure 37. Relative Rates for Creation of Vibrationally Excited CO.  $P_{CO_2} = 1/4$  torr,  $I = 0.9$  mA

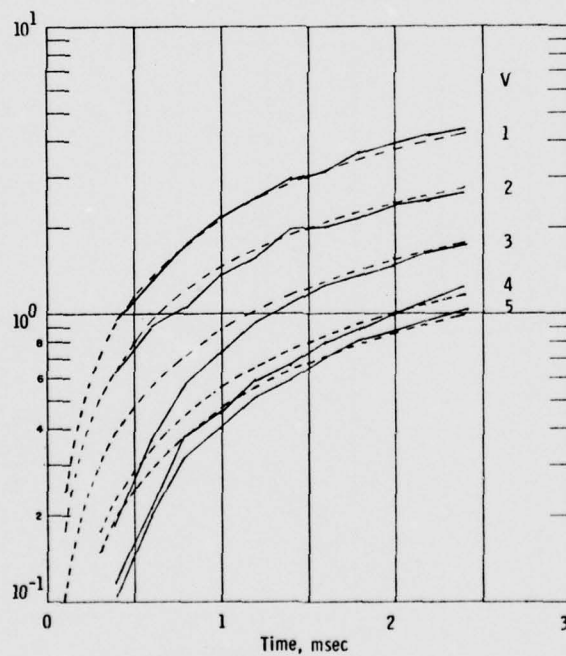


Figure 38. Comparison of Measured and Computed Vibrational Population Time Histories for  $v = 1-5$ . — data, --- prediction. Beam on



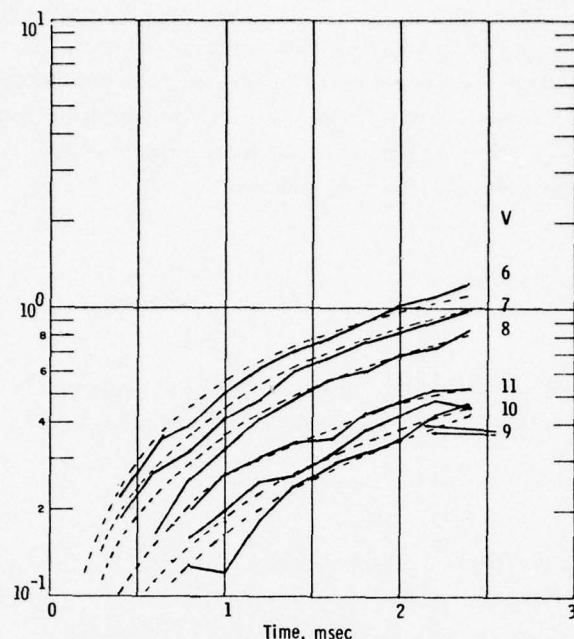


Figure 39. Comparison of Measured and Computed Vibrational Population Time Histories for  $v = 6-11$ . — data, --- prediction. Beam on

### 3.3 Data Interpretation

One data set for CO has been completely reduced and a set of rates for creation and deactivation of vibrationally excited CO have been determined. It would be valuable to reduce additional data sets in order to ascertain whether the present results would be consistent with observations taken under different experimental conditions. Such attempts have been unsuccessful during the present reporting period. In particular, strenuous efforts were made to develop CO vibrational population distributions from spectra taken at the conditions of  $I = 3.0$  mA and  $P_{\text{CO}_2} = 1/4$  and 1 torr. These efforts met with failure primarily because of the low signal to noise ratio of the spectra. Nonetheless, several salient features could be observed in the data base: (a) at both  $P_{\text{CO}_2} = 1/4$  and 1 torr the total fundamental band radiation scaled linearly with beam current for current of 0.9 and 0.3 mA, (b) the deactivation rates for high and low vibrational levels increased with increasing  $\text{CO}_2$  concentration between  $P_{\text{CO}_2} = 0.1-1$  torr, and (c) the peak CO intensity at beam termination, occurring at  $\approx v = 7-9$ , remained relatively constant over the  $\text{CO}_2$  pressure range of 0.1-1 torr. These observations are all consistent with the deactivation/excitation rates and mechanisms deduced in the present analysis.

It would be of value to specify the absolute CO concentrations and excitation rates in order to determine what portion of the electron energy is ultimately converted into CO vibrational energy. The absolute CO vibrational densities within the field of view,  $N_v$ , may be related to the total band intensity,  $I_T$ , specified in Watts/unit area/sterradian by the relationship

$$I_T = \frac{\sum N_v A_{v \rightarrow v-1} h\nu_{v \rightarrow v-1}}{4\pi A_f} \quad (82)$$

where  $A_f$  is the area of the field of view. The  $N_v$  are in turn linearly proportional to the relative CO number densities discussed above, that is,

$$N_v = A n_v, \quad (83)$$

and thus, given the relative vibrational populations and the total CO band intensity, the proportionality constant  $A$  may be readily determined. The total creation rate, within the field of view, for vibrationally excited CO may then be specified by

$$\dot{CO}^* = A \sum R_e(v) \quad (84)$$

Unfortunately, due to complications involving nonuniform detector response across the field of view, an absolute calibration cannot yet be provided. However, based upon the available information, it can be estimated to within an order of magnitude that there is one vibrationally excited CO molecule created per ion pair, that is,

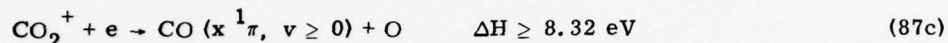
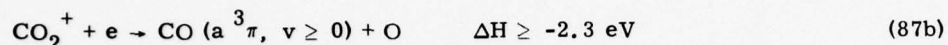
$$\dot{CO}^* \sim \dot{X}^+ = \frac{0.9 \rho I(\rho^{-1} dE/dX)l}{ew} = 1.9 \times 10^{17} \text{ sec}^{-1} \quad (85)$$

where  $l$  is the diameter of the field of view and 0.9 is the fraction of beam electrons which fall within the field of view over this length. Furthermore, the average number of quanta,  $\bar{v}$ , created per excited CO molecule may be defined by

$$\bar{v} = \frac{\sum v R_e(v)}{\sum R_e(v)} = 3.5 \quad (86)$$

Equations (85) and (86) may be used to estimate that approximately 3.5 percent of the beam energy deposited in the gas is converted to CO vibrational energy. It is to be emphasized that this estimate is only accurate to within an order of magnitude.

The actual kinetic mechanism by which this energy transfer occurs is not well defined. Reaction (26) is exothermic by 8.32 eV, assuming  $\text{CO}_2^+$  is in its ground vibrational state. This is sufficiently energetic so that the following reaction paths could occur



Gutcheck and Zipf<sup>34</sup> have studied the recombination of  $\text{CO}_2^+$  ions produced via charge exchange from  $\text{Ar}^+$ , as in the present system, and found that  $\approx 5$  percent of the recombining molecules formed the  $\text{CO}(A^1\pi)$  state. It was also found that the A state was formed in levels  $v = 0-3$  in approximately equal concentrations. (Note,  $v = 3$  was formed because the recombining ions were vibrationally excited. It is anticipated that this would not be the case in the present system.) The  $A^1\pi$  so created would radiatively decay to vibrationally excited ground state CO with a lifetime of  $\sim 10^{-8}$  sec.<sup>41</sup> The relative  $\text{CO}(v)$  creation rates resulting from  $\text{CO}(A^1\pi) \rightarrow \text{CO}(X^1\Sigma)$  transitions from equal populations of  $\text{CO}(A^1\pi, v = 0-2)$  and  $\text{CO}(A^1\pi, v = 0-3)$ , have been estimated from Franck-Condon factors presented in Schiffner and Klement<sup>40</sup> and are shown in Figure 40 in comparison with the measured excitation rates. As can be seen  $\text{CO}(v)$  creation by this process would exhibit a less steep dependence with vibrational level than observed. Of course, the existence of equal populations in the  $\text{CO}(A^1\pi)$  vibrational levels can only be conjectured at present.

$\text{CO}(a^3\pi)$  formation has also been observed in  $\text{CO}_2^+$  recombination. Wauchop and Broida<sup>42</sup> created  $\text{CO}_2^+$  through Penning ionization collisions with  $\text{He}(2^3S)$  metastables and found that 55 percent of the  $\text{CO}_2^+$  formed in this manner recombined to form  $\text{CO}(a^3\pi)$ . (Again, extrapolation of these results to the present conditions is questionable inasmuch as the ions produced in the experiment of Wauchop and Broida<sup>42</sup> could have been both electronically and vibrationally excited.) There is sufficient exothermicity in reaction (87b) to produce  $\text{CO}(a^3\pi)$  in vibrational states as high as  $v = 11$ ; however, states higher than  $v = 4$  will rapidly convert to the triplet states  $a^3\Sigma$ ,  $d^3\Delta$ , etc., through radiationless curve crossings, and these states will then radiatively cascade back to the  $a^3\pi$  state. The radiative

41. Krupenie, P. H. (1966) The Band Spectrum of Carbon Monoxide, NSRDS-NBS5.

42. Wauchop, T. S., and Broida, H. P. (1972) *J. Chem. Phys.* 56:330.

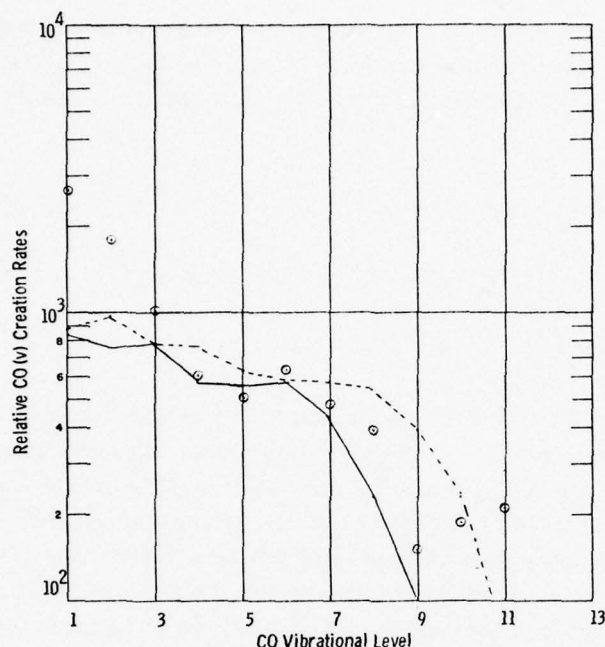
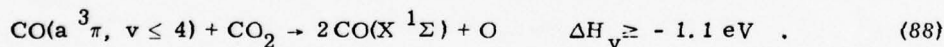


Figure 40. Estimated Relative CO(v) Creation Rates Due to CO(A  $1\pi$ )  $\rightarrow$  CO(X  $1\Sigma$ ) Transitions.  $\theta$ , measured creation rates  $R_e(v)$ , - CO(A  $1\pi$ ,  $v = 0-2$ ), --- CO(A  $1\pi$ ,  $v = 0-3$ )

lifetime for the  $a^3\pi$  state is several msec (Wauchop and Broida) but it can be rapidly quenched by collisions with CO<sub>2</sub>, that is,



Process (88) has a rate constant of  $1.7-3.8 \times 10^{-11} \text{ cm}^3/\text{sec}$ <sup>42, 43</sup> and thus for  $P_{\text{CO}_2} = 1/4 \text{ torr}$ , will have a characteristic quenching time of  $\sim 5 \mu\text{sec}$ . The exothermicity of reaction (88) is sufficient to produce ground state CO in levels  $v \leq 4$ , and thus this reaction alone is not sufficient to explain the present observations. It is interesting to note, however, that the measured CO(v) creation rates plateau at  $v = 4-5$ , with the dominant production occurring in the first four levels. Thus, it is possible that both the CO(A  $1\pi$ ) and CO( $a^3\pi$ ) states contribute to CO(v) creation in the present experiment. This conjecture could be tested by monitoring the VUV radiation occurring in the gas mixture while the beam is on.

43. Slanger, T.G., and Black, G. (1971) J. Chem. Phys. 55:2164.

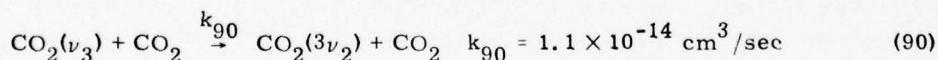
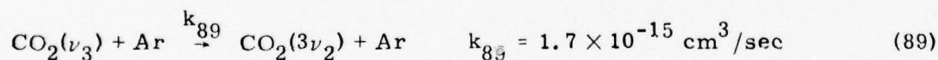


In conclusion, experimental studies (Krupenie,<sup>41</sup> and Wauchop and Broida<sup>42</sup>) have shown that  $\approx 60$  percent of  $\text{CO}_2^+$  recombinations lead to the formation of excited electronic states of CO. Although the ions in these studies were not necessarily in the same state as those in the present work, it has been shown that these electronic states can lead to the production of vibrationally excited ground state CO either by radiative decay or by collisional quenching.

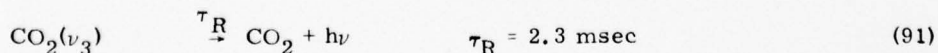
#### 4. $\text{CO}_2$ DATA ANALYSIS

Little has been said so far about the  $\text{CO}_2$  fluorescence data. It will be shown that the  $\text{CO}_2(\nu_3)$  band radiation is severely optically thick over the full range of experimental conditions. This effect precludes the determination of the absolute  $\text{CO}_2$  concentrations from data taken with the integrating sphere in, inasmuch as the transmission path length within this device is not well defined. The data discussed in Section 3, taken without the integrating sphere in, are amenable to reduction to absolute magnitude once the transmission losses are defined. In any event, the raw fluorescence data may be used to determine the deactivation mechanisms occurring within the gas after beam termination.

$\text{CO}_2(\nu_3)$  band fluorescence decay data have been taken at nominal  $\text{CO}_2$  pressures of 0, 0.1, 0.25, 0.5, and 1.0 torr. The zero pressure case corresponds to pure Ar with a minimal  $\text{CO}_2$  concentration resulting from wall out-gassing, and the  $\text{CO}_2(\nu_3)$  radiation in this case is optically thin. At all higher pressures, the radiation will be optically thick. The radiation decay in all cases is exponential, to first order, with characteristic decay time varying slightly with  $\text{CO}_2$  pressure. The dominant deactivation mechanisms in the gas are expected to be



and



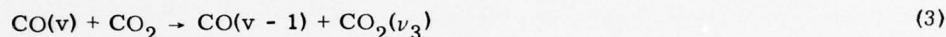
where the room temperature rate constants listed are from Yardley and Moore.<sup>44</sup> The characteristic decay time for  $\text{CO}_2(\nu_3)$  may then be defined as

44. Yardley, J.T., and Moore, C.B. (1967) *J. Chem. Phys.* **46**:4491.

$$\tau_{\nu_3} = (k_{89}[\text{Ar}] + k_{90}[\text{CO}_2] + \tau_R^{-1})^{-1}, \quad P_{\text{CO}_2} = 0 \quad (92a)$$

$$\tau_{\nu_3} = (k_{89}[\text{Ar}] + k_{90}[\text{CO}_2])^{-1}, \quad P_{\text{CO}_2} \geq 0 \quad (92b)$$

where the bracketed quantities represent the number densities of Ar and  $\text{CO}_2$ . The comparison between predicted and measured  $\text{CO}_2(\nu_3)$  decay times is shown in Figure 41 and can be seen to be quite good at the lower  $\text{CO}_2$  pressures. Note that the difference in observed relaxation times at  $\text{CO}_2$  pressures of 0.0 and 0.1 torr illustrate the effect of optical thickness. It can be seen that the measured relaxation time lags behind the predicted with increasing  $\text{CO}_2$  pressure. It is anticipated that this effect is due to vibrational pumping of  $\text{CO}_2(\nu_3)$  by CO, that is,



which becomes more pronounced with increasing  $\text{CO}_2$  pressure. This effect has not been modeled since the CO vibrational populations at the higher  $\text{CO}_2$  pressure have not been determined.

In general then, at the lower  $\text{CO}_2$  pressures the  $\text{CO}_2(\nu_3)$  fluorescence observations provide validation of the measured rate constant for reaction (89). Since the  $\text{CO}_2(\nu_3)$  deactivation phenomena is well understood, the  $\text{CO}_2(\nu_3)$  excitation rate may be determined from the data. It is expected that collisions with secondary electrons provide the relevant excitation mechanism, that is,



From Eqs. (92) and (93), it can be shown that the total  $\text{CO}_2(\nu_3)$  concentration within the field of view while the beam is on may be defined by

$$N_{\nu_3} = R_{\nu_3} \tau_{\nu_3} [1 - \exp(-t/\tau_{\nu_3})] \quad (94)$$

where  $R_{\nu_3}$  is the global excitation rate for reaction (93). Thus, if  $N_{\nu_3}$  can be determined, the absolute  $\text{CO}_2$  excitation rate and beam excitation rate and beam excitation efficiency may be specified.

It is, unfortunately, quite difficult to accurately define  $N_{\nu_3}$  from the experimental spectra. The  $\text{CO}_2(\nu_3)$  radiation with the chamber is dominantly doppler broadened and severely self absorbed. After the radiation leaves the chamber, it

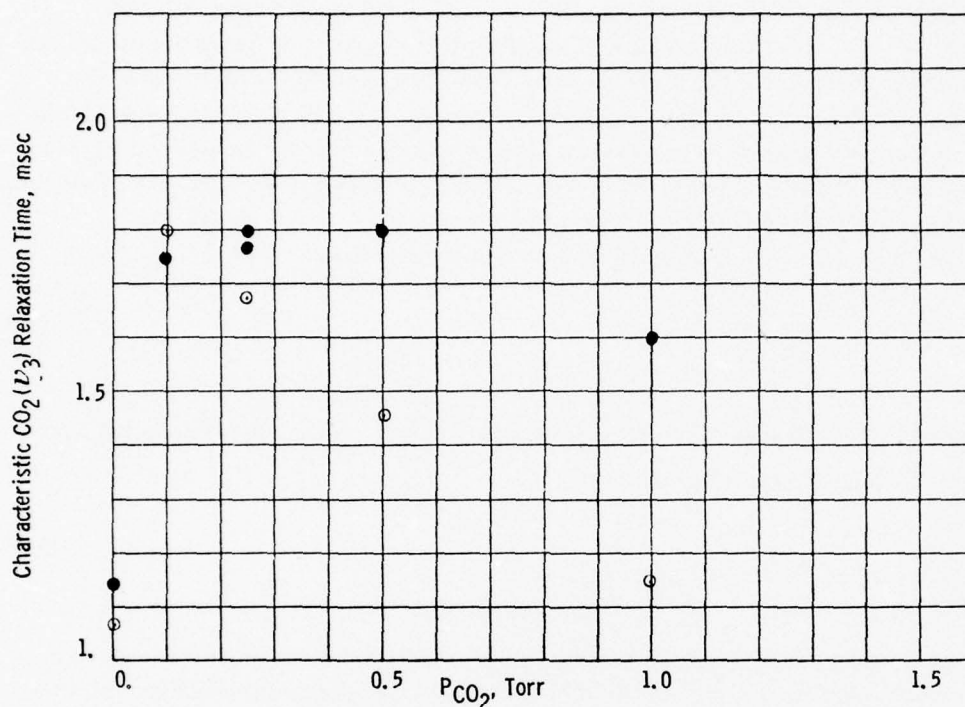


Figure 41. Comparison of Predicted and Observed  $CO_2(\nu_3)$  Relaxation Times.  $P_{Ar} = 9$  torr, ● - data, ○ - prediction from Eq. (92)

travels a length of 30-45 cm in ambient air before striking the detector and therefore undergoes additional absorption by Lorentz-broadened ambient  $CO_2$ . This latter effect has been rather cavalierly accounted for by application of a low resolution calibration correction. The justification for this step will be provided further in the text. The self absorption occurring within the chamber has been modeled in some detail as discussed below.

It was shown in Figure 15 that the radiating gas will be localized within the field of view. For purposes of calculating the transmittance, it has been assumed that the vibrationally hot gas is present only along the axis of the test chamber and propagates a distance of 11 cm through a room temperature, vibrationally equilibrated gas before leaving the chamber.

The fluorescent lines emitted by the excited  $CO_2$  molecules will have a doppler halfwidth at half maximum (HWHM) of  $9.4 \times 10^{-7} \nu$  (where  $\nu$  is the frequency of the transition in wavenumbers), or  $b_D \approx 2.2 \times 10^{-3} \text{ cm}^{-1}$  HWHM for the  $\nu_3$  transition

of  $\text{CO}_2$ . Collisional broadening of the spectral line by Ar results in a broadening of  $5.8 \times 10^{-4} \text{ cm}^{-1}$  HWHM for  $P_{\text{Ar}} = 9 \text{ torr}$ .  $\text{CO}_2$  self-broadening will add  $1.3 \times 10^{-5} - 1.3 \times 10^{-4} \text{ cm}^{-1}$  HWHM to the width of each line depending on amount present in the experiment (0.1-1 torr). Therefore, doppler broadening is the dominant mechanism for spectral line broadening, and will be considered first in the modeling to follow. The unexcited part of the gas mixture is taken to have the same temperature and pressure as the radiating molecules, and thus the absorption linewidths will be identical to the emitted ones.

A doppler lineshape may be described by the formula

$$k_{\nu}, \text{ cm}^2 = k_{\nu_{c_L}} e^{-\xi^2}, \quad (95)$$

where  $k_{\nu}$  is the absorption coefficient at frequency  $\nu$ .  $k_{\nu_{c_L}}$ , the absorption coefficient at line center, is defined by

$$k_{\nu_{c_L}} = \frac{S}{b_D} \sqrt{\ln 2 / \pi} \quad (96)$$

where  $S$  is the integrated linestrength for the single rotational transition in  $\text{cm}/\text{molecule}$ , that is,  $S = \int k_{\nu} d\nu$ ;  $\xi$ , which contains the lineshape behavior with frequency variation, is defined by

$$\xi = \frac{(\nu - \nu_{c_L})}{b_D} \sqrt{\ln 2}. \quad (97)$$

It is seen from these equations that  $k_{\nu} = \frac{1}{2} k_{\nu_{c_L}}$  when  $\nu - \nu_{c_L} = b_D$ . For an optically thin source, the radiation/unit length of an emitter with concentration  $N_R$  molecules/cc is

$$I_{\nu} = k_{\nu} N_R I_{\text{BB}} \quad \text{W/cm}^3\text{-sr-cm}^{-1} \quad (98)$$

where  $I_{\text{BB}}$  is the blackbody function. Attenuation of this radiation by doppler broadened lines over a distance  $L$  is given by

$$I'_{\nu} = k_{\nu} N_R I_{\text{BB}} \exp(-K N L) \quad (99)$$



where  $K$  is the total absorption coefficient due to all transitions (of  $\text{CO}_2$  or other species present) which overlap the emitted line, that is,

$$KN = \sum_i k_{\nu_i} N_i \quad (100)$$

The fractional transmission of a single doppler rotational line is then given by

$$\tau = \frac{\int_{-\infty}^{\infty} I_{\nu}' d\nu}{\int_{-\infty}^{\infty} I_{\nu} d\nu} = \frac{\int_{-\infty}^{\infty} I_{\text{BB}} e^{-\xi^2} \exp(-KNL) d\nu}{\int_{-\infty}^{\infty} I_{\text{BB}} e^{-\xi^2} d\nu} \quad (101)$$

Determination of the transmission function requires knowledge of all  $k_{\nu_i}$  at frequency intervals small compared to the linewidth  $b_D$  and evaluation of Eq. (101) at a large number of frequencies for each rotational transition. This approach is both time consuming and costly. If the assumption is made that the emission from a particular line is only significantly absorbed by the same transition in  $\text{CO}_2$  that gave rise to the radiation, a considerable simplification in Eqs. (100) and (101) occurs, that is,  $KN = k_{\nu} N_R$ . Since the blackbody function remains constant over the molecular linewidth, Eq. (101) then reduces to

$$\tau = \frac{\int_{-\infty}^{\infty} e^{-\xi^2} \exp \left\{ -k_{\nu} c_L N_R L e^{-\xi^2} \right\} d\nu}{\int_{-\infty}^{\infty} e^{-\xi^2} d\nu} \quad (102)$$

Equation (102) may be represented as a series expansion for small values of  $k_{\nu_{c_L}} N_R L$  (Mitchell and Zemansky<sup>45</sup>):

$$\tau = \sum_{n=0}^{\infty} (-1)^n \frac{\left(k_{\nu_{c_L}} N_R L\right)^n}{n! \sqrt{n+1}} \quad (103)$$

For large values of  $k_{\nu_{c_L}} N_R L$ , the above series involves small differences between large terms, and numerical evaluation of the integral is required. A plot of the fractional transmission given by Eq. (101) as a function  $k_{\nu_{c_L}} N_R L$ , is presented in Figure 42. Note that  $\tau$  approaches 0 and 1 for very strong and very weak lines respectively. The total fractional transmission of the entire spectrum is just the sum of the transmission of each rotational line in the band.

In order to estimate an upper limit for the effect of collisional broadening on the spectral lines, the fractional transmission of each rotational line was calculated assuming the spectral linewidth to be due entirely to collision broadening,

$$b_C = 0.0022 + 0.0007 = 0.0029 \text{ cm}^{-1} \text{ HWHM.}$$

The absorption coefficient over a single collision broadened rotational line is given by

$$k_{\nu} \text{ cm}^2 = k_{\nu_0} \frac{b_C^2}{(\nu - \nu_0)^2 + b_C^2} \quad (104)$$

where  $k_{\nu_0}$  is the absorption coefficient at the center of the homogeneous line defined by

$$k_{\nu_0} = \frac{S}{\pi b_C} \quad (105)$$

For the case of an optically thin Lorentzian source attenuated by Lorentzian absorbers, Eq. (101) becomes

45. Mitchell, A.C.G., and Zemansky, M.W. (1934) Resonance Radiation and Excited Atoms, Cambridge, London, p. 101.

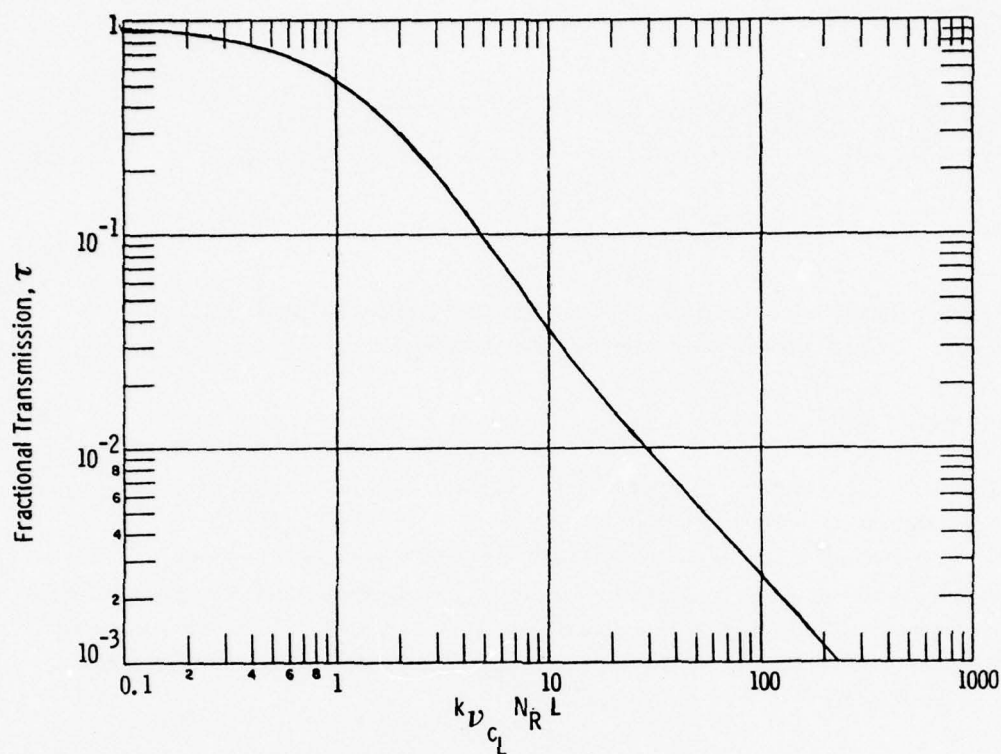


Figure 42. Fractional Transmission as a Function of Absorbing Gas Line Strength

$$\tau = \frac{\int_{-\infty}^{\infty} \frac{b_C}{(\nu - \nu_o)^2 + b_C^2} \frac{\pi}{\alpha} \exp \left\{ -k_{\nu_o i} N_i L \frac{b_C}{(\nu - \nu_o i)^2 + b_C^2} \right\} d\nu}{\int_{-\infty}^{\infty} \frac{b_C}{(\nu - \nu_o)^2 + b_C^2} d\nu} \quad (106)$$

If resonant self absorption is again taken to be the only attenuation mechanism (this assumption is somewhat more tenuous for Lorentzian lines with their more pronounced tails), then Eq. (106) reduces to

$$\tau = \frac{\int_{-\infty}^{\infty} \frac{b_C}{(\nu - \nu_0)^2 + b_C^2} \exp \left( -\frac{S}{\pi} N_R L \frac{b_C}{(\nu - \nu_0)^2 + b_C^2} \right) d\nu}{\int_{-\infty}^{\infty} \frac{b_C}{(\nu - \nu_0)^2 + b_C^2} d\nu} \quad (107)$$

With appropriate substitutions in Eq. (107), the transmission is found to be a function of the zeroth order imaginary Bessel function,  $I_0$ ,

$$\tau = e^{-\rho} I_0(\rho) \quad (108)$$

where  $\rho = SN_R L / 2\pi b_C$ .  $I_0$  may be approximated as a polynomial permitting analytical solution for  $\tau$  at every value of  $SN_R L$ .

Doppler and collision broadening are entirely independent processes. To describe a lineshape in which both significantly contribute, each infinitesimal frequency band of the collision broadened line may be viewed as being broadened by the doppler distribution. The resultant lineshape, referred to as a Voigt profile, is defined by Mitchell and Zemansky,<sup>45</sup> as

$$k_\nu = k_{\nu_{cL}} \frac{a}{\pi} \int_{-\infty}^{\infty} \frac{\exp(-y^2)}{a^2 + (\xi - y)^2} dy \quad (109)$$

where  $k_{\nu_{cL}}$  is defined by Eq. (96),  $\xi$  is defined by Eq. (97), and  $a$  is the ratio of the two halfwidths,

$$a = \frac{b_C}{b_D} \sqrt{\ln 2} \quad (110)$$

and

$$y = \frac{\sqrt{\ln 2}}{b_D} (\nu' - \nu_{cL}) \quad (111)$$

Integration over the dummy frequency,  $\nu'$ , is performed in order to include contributions from all doppler-shifted molecular transitions in the total absorption coefficient at  $(\nu - \nu_{cL})$ . For the present, experimental conditions  $a = 0.223 - 0.273$ . The lineshapes of a pure doppler transition and a Voigt profile with  $a = 0.25$  are



plotted in Figure 43 normalized to the peak of the doppler curve. The enhanced emission in the wings of the Voigt profile may result in a significantly different fractional transmission than for the doppler case. The fractional transmission of radiation from an optically thin Voigt broadened source attenuated by nonoverlapping Voigt absorbers is given by

$$\tau = \frac{\int_{-\infty}^{\infty} \left[ \int_{-\infty}^{\infty} \frac{e^{-y^2}}{a^2 + (\xi - y)^2} \exp \left( -k_{\nu} c_L N_R L \frac{A}{\pi} \frac{e^{-y^2}}{a^2 + (\xi - y)^2} \right) dy \right] d\nu}{\int_{-\infty}^{\infty} \left[ \int_{-\infty}^{\infty} \frac{e^{-y^2}}{a^2 + (\xi - y)^2} dy \right] d\nu} \quad (112)$$

A solution for Eq. (112) to permit determination of  $\tau$  as a function  $SN_R L$  is currently being developed. The function  $\tau$ , as determined from Eq. (112), will lie between the pure doppler and collision transmissions. Equations (102) and (108) have been used to evaluate the transmittance of the  $\text{CO}_2(\nu_3)$  band in the doppler and Lorentz line limits. The transition linestrengths,  $S$ , and frequencies were calculated for all rotational lines of the fundamental  $\nu_3$  asymmetric stretch of the

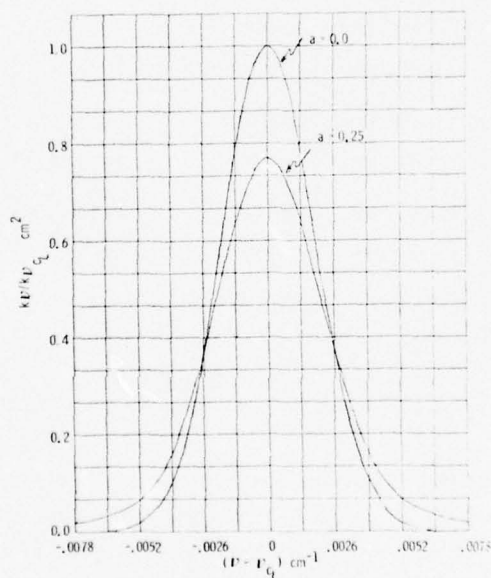


Figure 43. Voigt Lineshapes for  $a = 0$  and  $a = 0.25$

$O^{16}C^{12}O^{16}$  (626) molecule as well as for the  $\nu_3$  hot-band transitions, which involves molecules with thermally populated excited vibrational modes, and for all significant bands of the  $C^{13}O_2^{16}$ ,  $O^{16}C^{12}O^{18}$ , and  $O^{16}C^{12}O^{17}$  isotopes. The integrated band intensities,  $S_v$ , of the transitions included in the calculation are listed in Table 8 along with band center frequencies,  $\nu_{band}$ .

Table 8.  $CO_2(\nu_3)$  Spectral Properties

Isotope	Transition Ground State $\nu_1 \nu_2 \nu_3$	$S_v^*$ cm/molec.	$\nu_{band}^*$ cm <sup>-1</sup>	Branches	Rotational Levels J
626	00 <sup>0</sup> 0	9.598E-17	2349.146	P, R	even J only
626	01 <sup>1</sup> 0	7.66E-18	2336.637	P, Q, R	all J, c odd
636	00 <sup>0</sup> 0	9.602E-19	2283.490	P, R	even J
628	00 <sup>0</sup> 0	3.33E-19	2332.112	P, R	all J
626	02 <sup>2</sup> 0	3.08E-19	2324.148	P, Q, R	all J, c even
626	02 <sup>0</sup> 0	1.934E-19	2327.432	P, R	even J
626	10 <sup>0</sup> 0	1.183E-19	2326.594	P, R	even J
636	01 <sup>1</sup> 0	8.18E-20	2271.763	P, Q, R	all J, c odd
627	00 <sup>0</sup> 0	6.37E-20	2340.01	P, R	all J
628	01 <sup>1</sup> 0	2.58E-20	2324.148	P, Q, R	all J, c&d each
626	03 <sup>3</sup> 0	1.22E-20	2311.675	P, Q, R	all J, c odd
627	01 <sup>1</sup> 0	4.97E-21	2327.575	P, Q, R	all J, c&d each
636	02 <sup>2</sup> 0	3.46E-21	2260.045	P, Q, R	all J, c even
* From ref. 46					

All transitions observed in this spectral region involve  $\Delta\nu_3 = 1$ , and may have three branches labelled P, Q, and R for rotational quantum changes of -1, 0, and +1. Molecules with a center of symmetry (626, 636) have alternate rotational lines missing from all transitions. When no orbital angular momentum exists about the internuclear axis, as is the case for the fundamental transitions of all the isotopes, there is no Q branch evident in the spectra. When angular momentum,  $l$ , does

exist, each rotational level is split because of the coupling of rotation with the orbital angular momentum. The nearly degenerate components of the rotational level are labelled c and d.

The transition line center frequencies (in  $\text{cm}^{-1}$ ) involving each rotational level (including each of the nondegenerate parity doublets) are calculated relative to the band center frequency using the rotational constants given in McClatchey et al.<sup>46</sup> The total integrated bandstrength,  $S_V$ , is then divided among the allowed transitions, with the individual linestrengths,  $S$ , given by McClatchey et al, as

$$S = \frac{S_V S_J}{Q_{\text{rot}}} \exp - \left\{ \frac{J'(J' + 1)}{Q_{\text{rot}}} \right\} \frac{\nu_{cL}}{\nu_{\text{band}}} ; \quad (113)$$

$Q_{\text{rot}}$  is the rotational partition function and  $J'$  is the initial (upper) rotational level from which the transition originates.  $S_J$  are the linestrength factors given by the Hönl-London Formulae (Herzberg<sup>37</sup>) as

$$\begin{aligned} S_J^R &= (J' + \ell)(J' - \ell)/J' \\ S_J^Q &= (2J' + 1) \ell^2 / J'(J' + 1) \\ S_J^P &= (J' + 1 + \ell)(J' + 1 - \ell)/(J' + 1) \end{aligned} \quad (114)$$

which are very good approximations to the true rotational linestrength factors for this case where coupling between  $\ell$  and  $J$  is weak.

These linestrengths are then used to calculate the fractional transmission of each rotational line over the range of experimental  $\text{CO}_2$  pressures. In addition, the emitted intensity per molecule,  $I$ , for each rotational line is calculated by integrating Eq. (98)

$$\begin{aligned} I &= \int_{-\infty}^{\infty} \frac{I_{\nu}}{N_R} d\nu = \int_{-\infty}^{\infty} I_{BB} k_{\nu} d\nu \\ &= I_{BB} S(\text{W/molecule-sr}) \end{aligned} \quad (115)$$

46. McClatchey, R.A., Benedict, W.S., Clough, S.A., Burch, D.E., Calfee, R.F., Fox, K., Rothman, L.S. and Garing, J.S. (1973) AFCRL Atmospheric Absorption Line Parameters Compilation, A.F.S.C. Report AFCRL-TR-73-0096.

The total emitted intensity at each of the experimental CO<sub>2</sub> pressures was obtained as the sum of the values for each rotational line for both the pure doppler and collision broadened cases. The total transmitted intensity per molecule for all lines is plotted in Figure 44 as a function of CO<sub>2</sub> pressure for both approximations. (Note the predicted intensity is radiation per CO<sub>2</sub> molecule at a vibrational temperature of 300°K.) Because the Lorentzian lines spread more of the total linestrength into the wings of the line, transmission by the collision broadened lines is greater than for the doppler case for all CO<sub>2</sub> pressures, differing by a factor of five at 1 torr. In the limit of no attenuation ( $\tau = 1$ )

$$\sum_j \sum_i I_{ij} \tau_{ij} = \sum_j S_{V_j} I_{BB}(\nu_{\text{band}_j}) \quad (116)$$

where  $i$  is over all rotational lines and  $j$  is over all transitions. This equivalence is maintained to within 2 percent for both doppler and collision broadened cases.

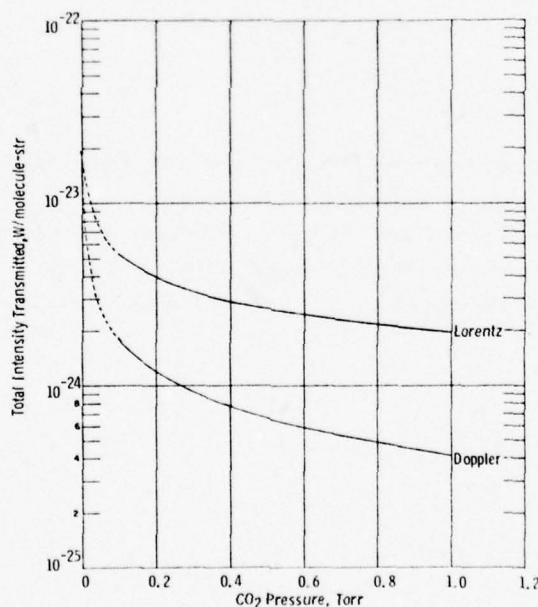


Figure 44. Total Transmitted Intensity as a Function of CO<sub>2</sub> Pressure for Doppler and Lorentz Broadened Lines.  $P_{Ar} = 9$  torr



The role of the hot bands and isotopes in the total transmitted intensity is clarified by Figures 45 and 46. In Figure 45, the fractional doppler transmission,  $\sum_i \tau_{ij}$  of each of the six strongest transitions in Table 8 is plotted as a function of  $\text{CO}_2$  pressure. Doppler radiation emitted by the 626 fundamental will be severely attenuated, so much so that, even though its integrated band strength is over twelve times greater than the hot band  $(01^10)$   $S_V$  value, the hot band radiation dominates the transmitted doppler radiation spectrum for all experimental  $\text{CO}_2$  pressures as shown in Figure 46. At pressures near 0.1 torr of  $\text{CO}_2$ , the  $01^10$  transition of the 626 isotope will account for nearly half to the total transmitted intensity. At pressures above 0.8 torr even the 636 fundamental, whose  $S_V$  is two orders of magnitude less, will contribute more intensity to the transmitted spectrum than the 626 fundamental. This behavior is expected when the exponential factor dominates Eq. (99). Also plotted in Figure 45 is the fractional transmission of the Lorentz broadened 626 fundamental. Self absorption for the Lorentz case is not nearly as severe and the 626 fundamental will dominate the transmitted radiation spectrum over the  $\text{CO}_2$  pressure range shown. These predictions are in good agreement with published values of the 626 fundamental transmission as shown in Table 9 (Bulos et al,<sup>47</sup> and Kumer et al<sup>48</sup>).

Table 9. Fractional Transmission of 626 Fundamental

	$P_{\text{CO}_2}$ 0.1 torr	1.0 torr
Doppler Limit - this work	$3.24 \times 10^{-2}$	--
- Bulos et al <sup>47</sup>	$3.09 \times 10^{-2}$	--
- Kumer et al <sup>48</sup> (225°K)	$3.5 \times 10^{-2}$	--
Lorentz Limit - this work	--	$6.5 \times 10^{-2}$
- Bulos et al <sup>47</sup>	--	$6.1 \times 10^{-2}$

47. Bulos, B.R., and Phelps, A.V. (1976) Phys. Rev. A 14:615.

48. Kumer, J.B., and James, T.C. (1974) J. Geophys. Res. 79:638.

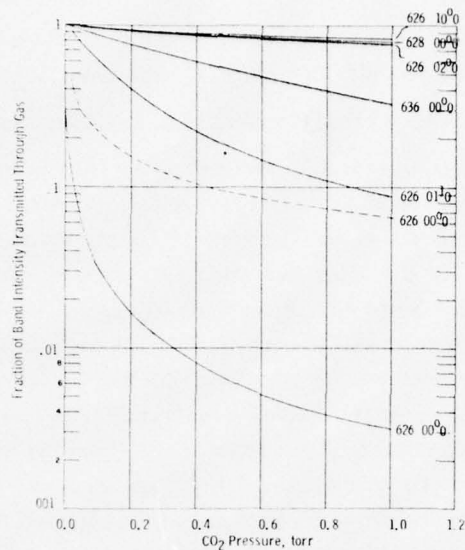


Figure 45. Fraction of Total Unattenuated Band Intensity Transmitted for the Six Strongest Transitions for Doppler Lines, and for the Lorentz Broadened 626 Fundamental as a Function of  $\text{CO}_2$  Pressure

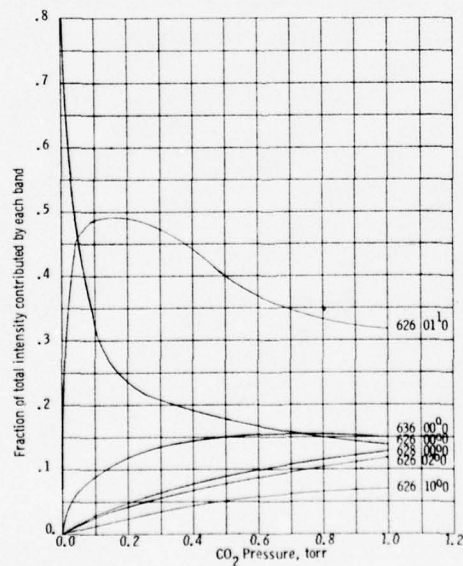


Figure 46. Relative Contributions of Individual Bands to the Total Transmitted Radiation as a Function of  $\text{CO}_2$  Pressure

It is to be noted that the predictions shown in Figure 46 may be used to justify the neglect of absorption by ambient  $\text{CO}_2$  in the modeling. This absorption will dominantly effect the radiation from the 626 fundamental band, which has the strongest bandstrength. However, as shown in Figure 46 this band provides only a small fraction of the total transmitted  $\text{CO}_2(\nu_3)$  radiation and thus a decrease in its transmissivity will not significantly effect the predicted  $\text{CO}_2(\nu_3)$  radiation levels. Carrying this point one step further, although it is expected that the use of a Voigt profile will increase the transmission of the 626 fundamental band, absorption by ambient  $\text{CO}_2$  will act in the opposite direction. Thus it may be that the use of a doppler profile provides a realistic estimate of the total transmitted radiation. The validity of this conjecture should be checked by more detailed modeling.

In order to permit comparison with the experimental spectra, the predicted transmitted line intensities must be convolved with the previously described sinc slit function of  $10 \text{ cm}^{-1}$  resolution (see Section 3.2). During convolution, the sinc slit function was truncated at the second zero crossing on each side of the center frequency. All the  $\tau_{ij}$  were sorted by frequency, summed in  $0.4 \text{ cm}^{-1}$  cells, and convolved with the sinc function to determine spectral intensity as a function of wavelength.

Experimental  $\text{CO}_2(\nu_3)$  spectra, corrected for atmospheric transmission and detector response, are displayed in Figures 47 and 48 for nominal  $\text{CO}_2$  pressures of 0.25 and 1 torr. The two spectra are quite similar, exhibiting a broad double peak in the region of maximum intensity and two secondary peaks at  $\approx 2270$  and  $2380 \text{ cm}^{-1}$ . A small bump at  $\approx 2360 \text{ cm}^{-1}$  is also observed in the data for  $P_{\text{CO}_2} = 1$  torr. Shown for comparison in Figures 49-53 are the predicted spectra of doppler broadened lines for  $P_{\text{CO}_2} = 0.0, 0.1, 0.25, 0.5$  and  $1.0$  torr respectively. The prediction of Figure 49 corresponds to unattenuated  $\text{CO}_2(\nu_3)$  radiation and can be seen to be quite different from the data. In particular the spectral width of the unattenuated band is much narrower, the double peaks in the region of maximum intensity occur at different wavenumbers than those of the data, the central minimum is much deeper, and no secondary peaks are in evidence. It is clear that the effects of self absorption on the data are quite severe. In contrast, both data and prediction, normalized to peak intensity, are shown in Figures 51 and 53 and the comparison is seen to be excellent, with the predictions duplicating all the dominant spectral features of the data.

It is evident from comparison of Figure 49 to Figures 50-53 that the effect of increasing  $\text{CO}_2$  pressure is to shift the spectral intensity to the red. This occurs because the hot band and isotopic band radiation increases relative to that of the fundamental band (see Figure 46). The predicted contribution of each of the dominant bands (the 626 fundamental band, the isotope bands and the hot bands) to the

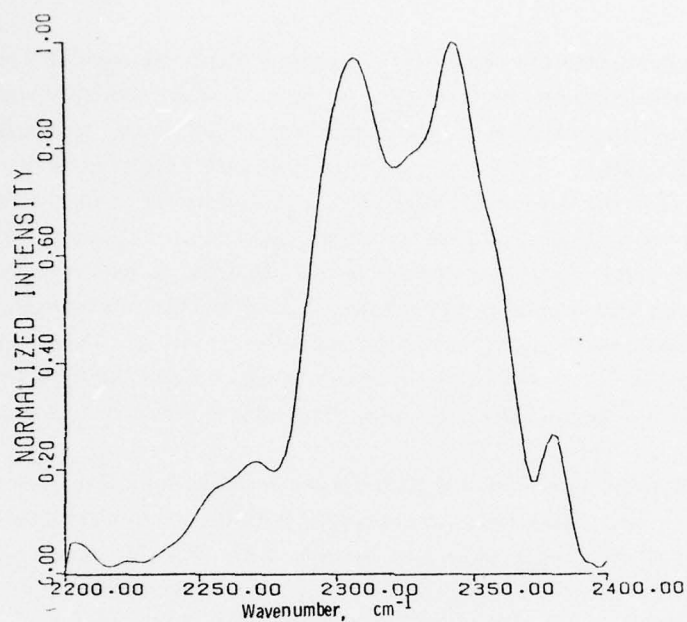


Figure 47. Normalized Experimental Spectrum at  $t = 2.6$  msec for  $P_{CO_2} = 0.25$  torr,  $I = 0.9$  mA,  $V = 30$  kV,  $P_{Ar} = 9$  torr

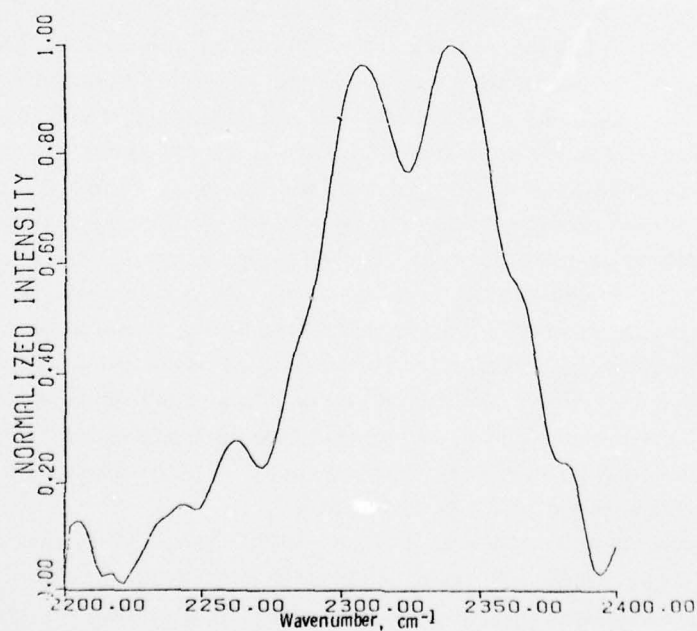


Figure 48. Normalized Experimental Spectrum at  $t = 2.6$  msec for  $P_{CO_2} = 1$  torr,  $I = 0.3$  mA,  $v = 30$  kV,  $P_{Ar} = 9$  torr



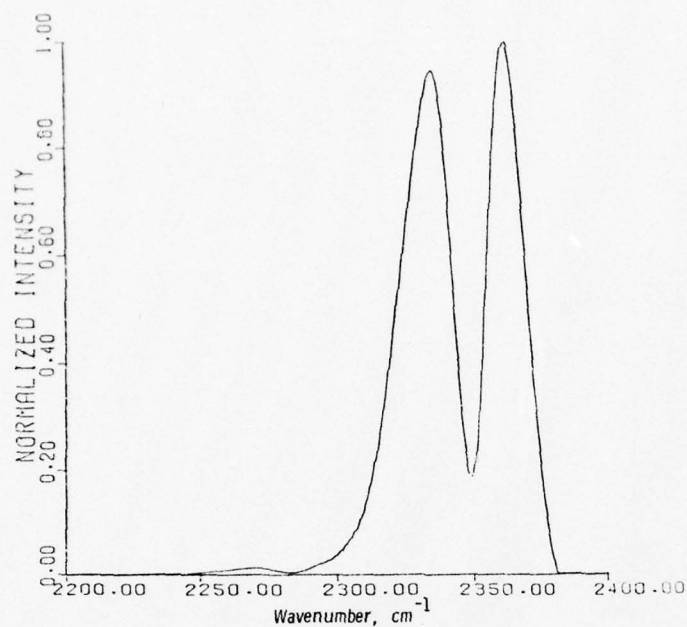


Figure 49. Predicted  $\text{CO}_2(\nu_3)$  Band Intensity. Doppler broadened lines. Resolution =  $10 \text{ cm}^{-1}$ .  $P_{\text{CO}_2} = 0.0 \text{ torr}$ , no attenuation. Maximum intensity =  $4.39 \times 10^{-25} \text{ W/molecule} \cdot \text{cm}^{-1}\text{-sr}$

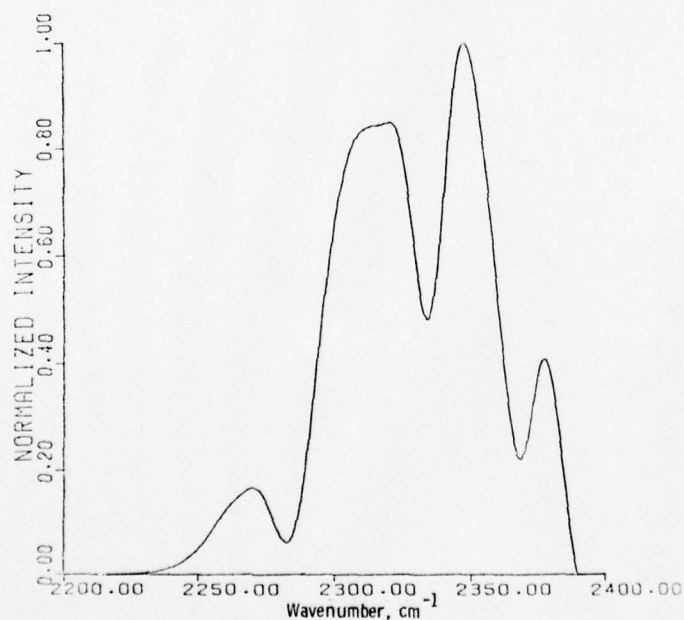


Figure 50. Predicted Transmitted  $\text{CO}_2(\nu_3)$  Band Intensity. Doppler Broadened lines. Resolution =  $10 \text{ cm}^{-1}$ .  $P_{\text{CO}_2} = 0.10 \text{ torr}$ . Maximum intensity =  $2.591 \times 10^{-26} \text{ W/molecule-sr-cm}^{-1}$

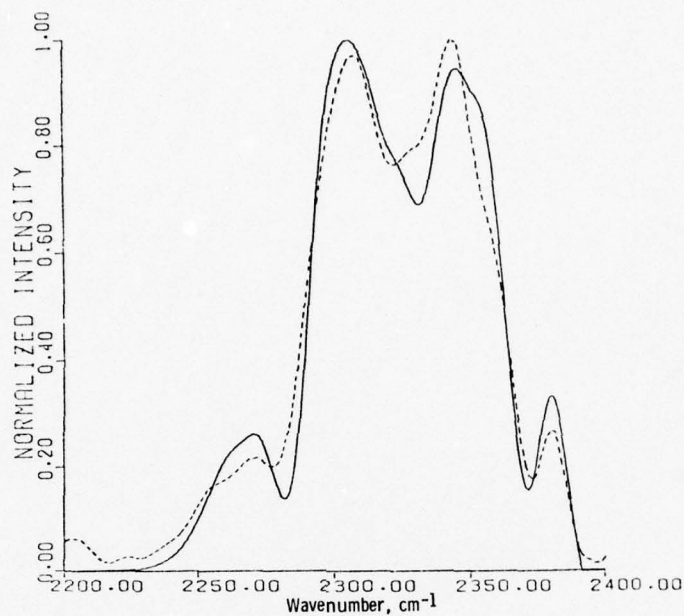


Figure 51. Predicted and Measured  $\text{CO}_2(\nu_3)$  Band Transmitted Intensity. Doppler broadened lines. Resolution =  $10 \text{ cm}^{-1}$ .  $P_{\text{CO}_2} = 0.25 \text{ torr}$ . Predicted maximum intensity =  $1.261 \times 10^{-26} \text{ W/molecule-sr-cm}^{-1}$ . — prediction, - - - - - data

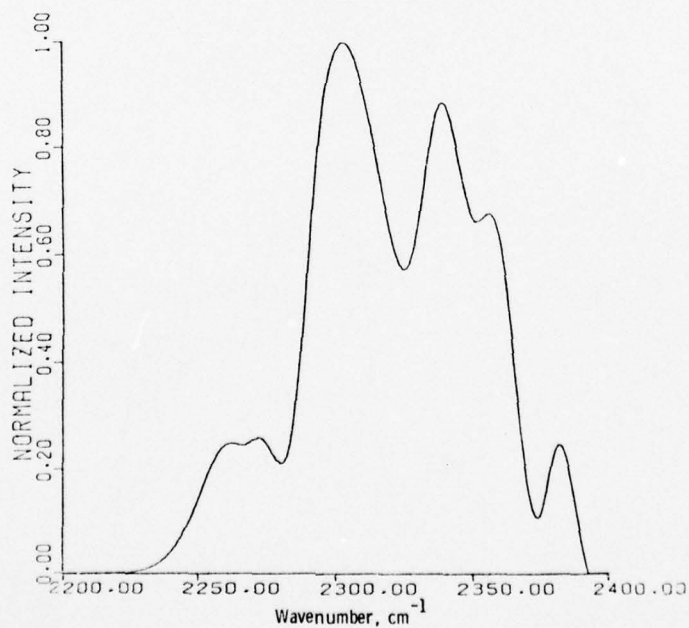


Figure 52. Predicted  $\text{CO}_2(\nu_3)$  Band Transmitted Intensity. Doppler broadened lines.  $P_{\text{CO}_2} = 0.50 \text{ torr}$ . Maximum intensity =  $8.383 \times 10^{-27} \text{ W/molecule-sr-cm}^{-1}$

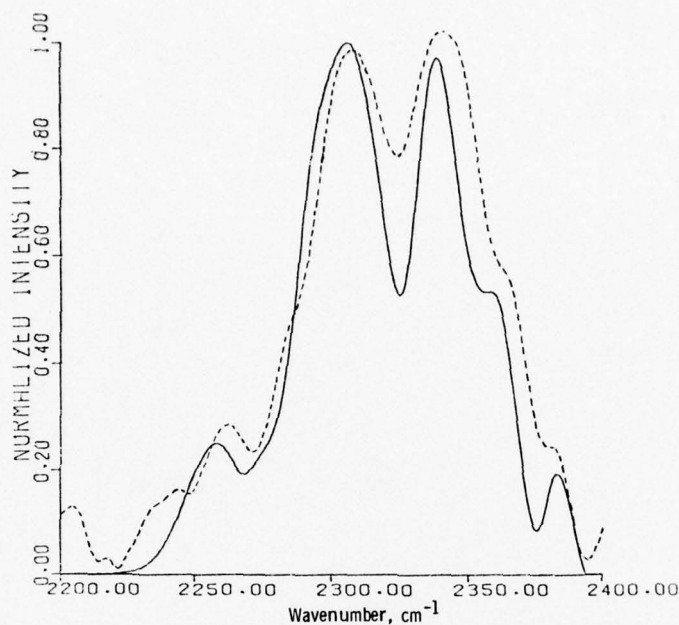


Figure 53. Predicted and Measured  $\text{CO}_2(\nu_3)$  Band Transmitted Intensity of Doppler Broadened Lines. All transactions included with self absorption only.  $P_{\text{CO}_2} = 1.00$  torr. Predicted maximum intensity =  $5.287 \times 10^{-27}$  W/molecule-sr-cm $^{-1}$ . — prediction, ----- data

total predicted spectra is shown in Figures 54 and 55 for  $\text{CO}_2$  pressures of 0.25 and 1.0 torr respectively. As can be seen the 626 fundamental bands provide a dominant contribution only to the secondary peak at  $2380 \text{ cm}^{-1}$ , while the isotopic fundamental bands are the source of the secondary peak at  $2270 \text{ cm}^{-1}$ . Finally, the primary source of radiation at band center is the 626 hot bands. The fact that all these spectral features, in approximately the same intensity ratios, are observed in the data to be taken as strong evidence that the present modeling provides a good approximation to the actual transmission phenomena. It should be noted that in Figure 54 the predicted 626 fundamental intensity at  $\approx 2380 \text{ cm}^{-1}$  is slightly larger than that for the total band intensity. This is an artifact introduced by the system slit function. The total unconvolved intensity in this wavenumber region is of course slightly greater than that due to the 626 fundamental alone; however, the effect of the negative side lobes in the system slit function is to decrease this intensity slightly relative to that of the 626 fundamental.

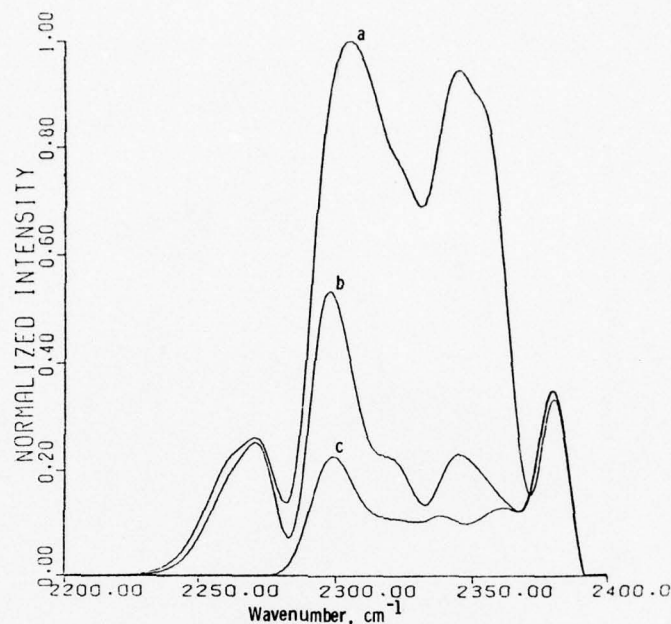


Figure 54. Comparison of Three Sets of Doppler Predictions for  $\text{CO}_2\nu_3$  Band Radiation at 0.25 torr  $\text{CO}_2$  With (a) All Transitions of Table 8 Included (Top Trace), (b) No Hot Bands, But All Isotopic Fundamentals Included (Middle Trace), and (c) Only 626 Isotope Fundamental Included (Lowest Trace). All three curves are normalized to peak of curve a. Maximum intensity =  $1.261 \times 10^{-26}$  W/molecule-sr-cm $^{-1}$

Finally a set of spectral transmission predictions for Lorentz broadened lines, including all  $\text{CO}_2(\nu_3)$  band transitions are presented in Figures 56-59 for  $\text{CO}_2$  pressures of 0.1, 0.25, 0.5 and 1.0 torr respectively. (The predicted unattenuated Lorentzian  $\text{CO}_2(\nu_3)$  spectrum is the same as that for doppler broadening shown in Figure 49). It can be seen that these predictions are in poor agreement with the data of Figures 47 and 48, thus adding further credence to the validity of the doppler approximation.

These transmission predictions may be used to provide an estimate of the total  $\text{CO}_2(\nu_3)$  concentration within the field of view. The total observed  $\text{CO}_2(\nu_3)$  radiation  $I_T$  in W/cm $^2$ -sr may be related to the  $\text{CO}_2(\nu_3)$  concentration by the relationship

$$I_T = \frac{N_{\nu_3}(h\nu)}{4\pi A_f \tau_R f} \quad (117)$$



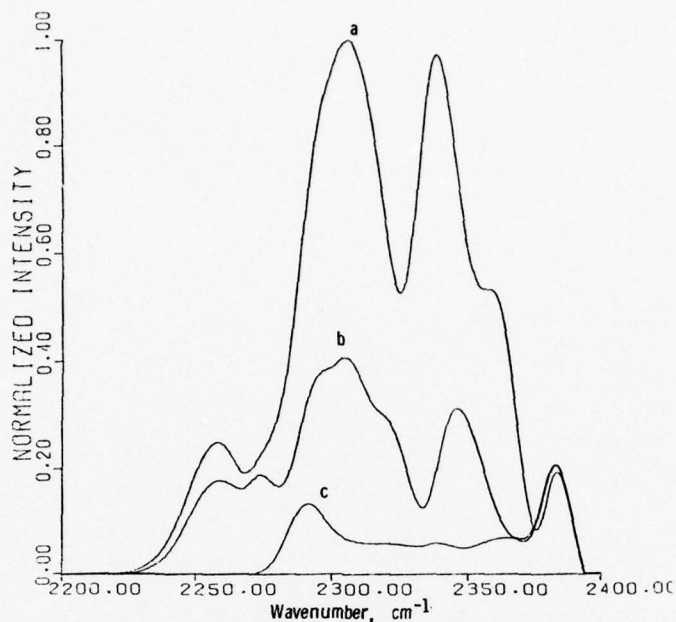


Figure 55. Comparison of Three Sets of Doppler Predictions for  $\text{CO}_2(\nu_3)$  Band Radiation at 1.00 Torr of  $\text{CO}_2$  With (a) All Transitions of Table 8 Included (Top Trace), (b) No Hot Bands, But all Isotopic Fundamentals Included (Middle Trace), and (c) Only 626 Isotope Fundamental Included (Lowest Trace). All three curves are normalized to peak of curve a. Maximum intensity =  $5.287 \times 10^{-27}$  W/molecule-sr-cm $^{-1}$

where  $h\nu$  is the vibrational energy of the  $\nu_3$  mode,  $4.6 \times 10^{-20}$  J,  $\tau_R$  is the radiative lifetime of 2.3 msec,  $A_f$  is the area of the field of view,  $52.8 \text{ cm}^2$ , and  $f$  is a correction factor for transmission losses which can be deduced from Figure 44. For the case  $P_{\text{CO}_2} = 1/4$  torr,  $I = 0.9$  mA, which was analyzed in Section 3, the actual  $\text{CO}_2$  pressure found to be 0.33 torr and thus, from Figure 44,  $f = 22$ . As mentioned earlier the data is not absolutely calibrated; however, an order of magnitude estimate of the  $\text{CO}_2(\nu_3)$  band intensity may be provided. Using this estimate, Eq. (117) and  $f = 22$ , it can be deduced that

$$N_{\nu_3} \approx 1.2 \times 10^{15} \text{ molecules} \quad (118)$$

at  $t = 2.4$  msec.

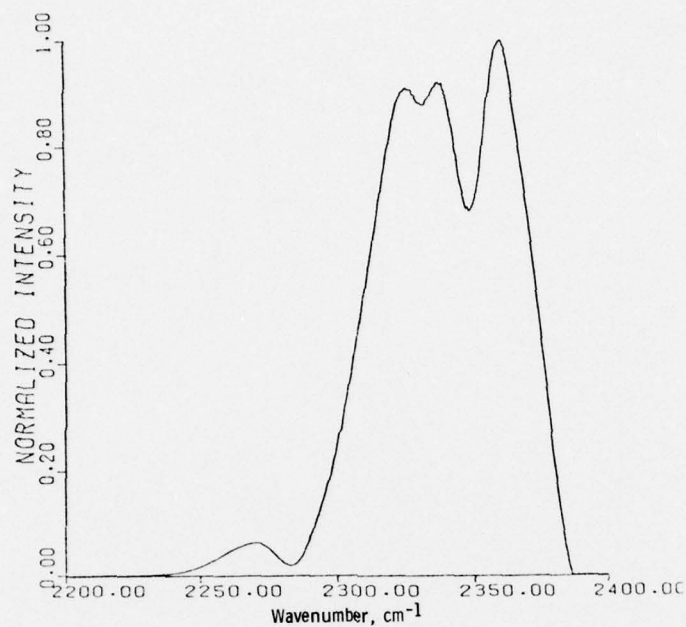


Figure 56. Predicted Transmitted Intensity of  $\text{CO}_2(\nu_3)$  Radiation for Lorentz Broadened Lines.  $P_{\text{CO}_2} = 0.10$  torr,  $P_{\text{Ar}} = 9$  torr. Maximum Intensity =  $7.689 \times 10^{-26}$  W/molecule-sr-cm $^{-1}$

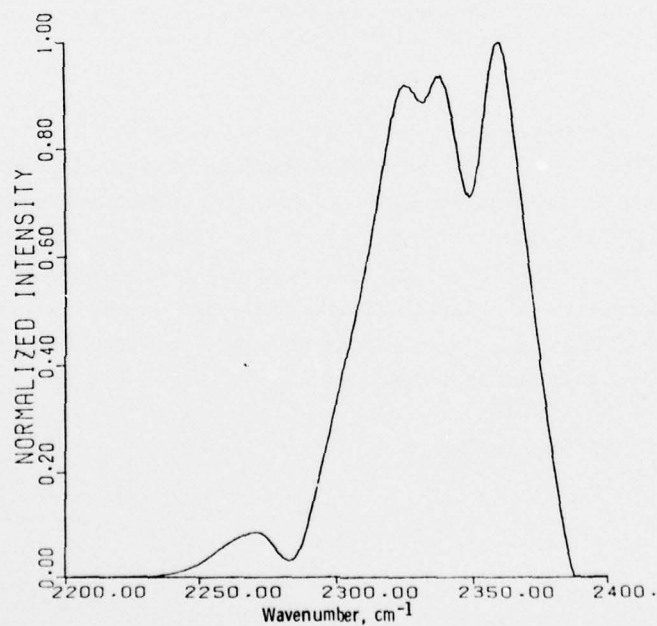


Figure 57. Predicted Transmitted Intensity of  $\text{CO}_2(\nu_3)$  Radiation for Lorentz Broadened Lines.  $P_{\text{CO}_2} = 0.25$  torr. Maximum intensity =  $5.126 \times 10^{-26}$  W/molecule-sr-cm $^{-1}$

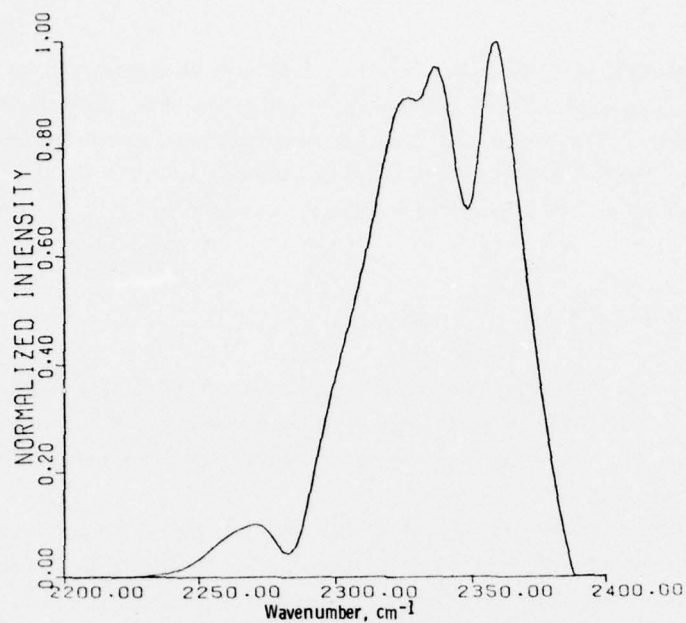


Figure 58. Predicted Transmitted Intensity of  $\text{CO}_2(\nu_3)$  Radiation for Lorentz Broadened Lines.  $P_{\text{CO}_2} = 0.50$  Torr. Maximum intensity =  $3.755 \times 10^{-26}$  W/molecule-sr-cm $^{-1}$

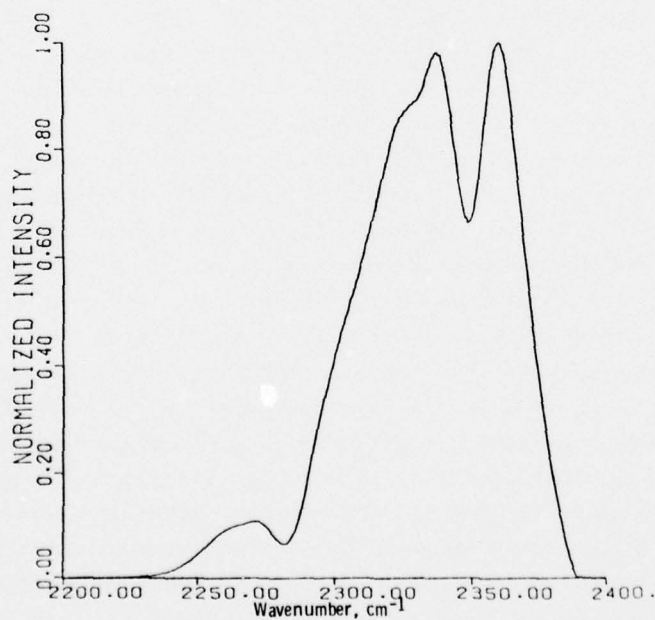


Figure 59. Predicted Transmitted Intensity of  $\text{CO}_2(\nu_3)$  Radiation for Lorentz Broadened Lines.  $P_{\text{CO}_2} = 1.00$  torr. Maximum intensity =  $2.703 \times 10^{-26}$  W/molecule-sr-cm $^{-1}$

The global  $\text{CO}_2(\nu_3)$  excitation rate  $R_{\nu_3}$  may now be deduced to be  $9.2 \times 10^{17}$  mol/sec from Eqs. (94), (118) and the observed value of  $\tau_{\nu_3}$  of  $1.76 \times 10^{-3}$  sec. Upon comparing this with the total ion pair creation rate within the field of view, as determined in Eq. (85), it can be seen that there are  $\sim 4.9$   $\text{CO}_2(\nu_3)$  excitations per ion pair created. The total beam power converted to  $\text{CO}_2(\nu_3)$  within the field of view is

$$\dot{P}_{\nu_3} = R_{\nu_3} (h\nu) \approx 4.3 \times 10^{-2} \text{ watts} , \quad (119)$$

as compared to the 0.8 W total beam power deposited within the field of view. Thus  $\sim 5.5$  percent of the beam energy deposited in the gas is converted to  $\text{CO}_2(\nu_3)$  vibrational energy. Once again these estimates are only accurate to within an order of magnitude.

The remaining cases,  $P_{\text{CO}_2} = 0.1, 0.5$  and  $1.0$  torr have not been studied in detail. However, a crude estimate of their relative peak  $\text{CO}_2(\nu_3)$  concentrations may be developed from the observed peak intensities. Since the observed  $\text{CO}_2(\nu_3)$  relaxation times are approximately the same between  $0.1$ - $1.0$  torr, the  $\text{CO}_2(\nu_3)$  populations will be roughly proportional to the peak  $\text{CO}_2(\nu_3)$  intensity multiplied by the predicted correction factor  $f$ . The measured peak  $\text{CO}_2(\nu_3)$  intensity and resulting estimated relative  $\text{CO}_2(\nu_3)$  populations are shown in Figure 60. As can be seen, the estimated  $\text{CO}_2(\nu_3)$  population increases only some 50 percent over a factor of ten change in  $\text{CO}_2$  pressure. The actual variation in secondary electron excitation of  $\text{CO}_2$  with  $\text{CO}_2$  pressure may be less than this, inasmuch as the effect of vibrational pumping by CO has not been taken into account.

It would appear then that the percentage of deposited beam energy which is transferred to the  $\text{CO}_2(\nu_3)$  state does not vary significantly between  $P_{\text{CO}_2} = 0.1$ - $1.0$  torr. This effect is most probably due to the preponderance of argon in the gas mix. The secondary electrons created by the beam will typically have a significant amount of kinetic energy which is subsequently lost by collisions with the gas molecules. Above electron energies of  $\approx 15$  eV, inelastic electron-neutral collision mechanisms in Ar will provide the dominant electron energy decay. However, there are no inelastic channels for electron-argon collisions at energies below  $\approx 15$  eV and  $\text{CO}_2$  - even strongly diluted in Ar - will provide the dominant electron energy dissipation for this energy range. Therefore, it is possible that a significantly larger percentage of beam energy might be channeled to the  $\text{CO}_2(\nu_3)$  state at higher  $\text{CO}_2$  partial pressures. Indeed it has been estimated by Sawada et al.<sup>49</sup> that in the case of a thick target of pure  $\text{CO}_2 \approx 20$  percent of the beam energy

49. Sawada, T., Strickland, D.J., and Green, A.E.S. (1972) *J. Geophys. Res.* 77:4812.



will be channeled to the  $\text{CO}_2(\nu_3)$  mode. It should be stressed that the estimates presented in Figure 60 are crude and that more detailed study is required.

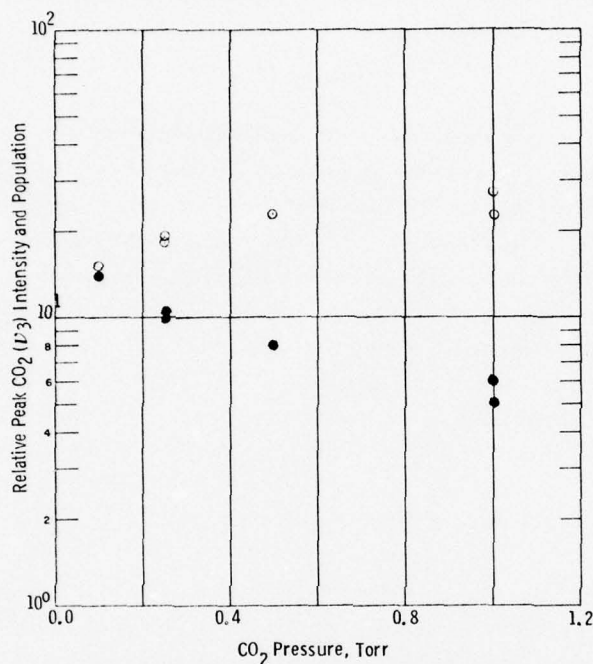


Figure 60. Relative Peak  $\text{CO}_2(\nu_3)$  Population and Intensity vs  $\text{CO}_2$  Pressure.  $P_{\text{Ar}} = 9$  torr.  
 ● - intensity, ○ - population

## 5. SUMMARY AND CONCLUSIONS

Both  $\text{CO}_2(\nu_3)$  and CO fundamental band radiation have been observed in electron irradiated mixtures of  $\text{CO}_2/\text{N}_2$ ,  $\text{CO}_2/\text{Ar}$  and  $\text{CO}_2/\text{He}$ . In all cases, the evident production mechanism for the vibrationally excited CO is the electron/ion recombination reaction



The CO spectra for one case, corresponding to beam conditions of  $V = 30$  kV,  $I = 0.9$  mA, and gas conditions of  $P_{\text{Ar}} = 9$  torr,  $P_{\text{CO}_2} \approx 1/4$  torr,  $T = 300^\circ\text{K}$ , has been reduced in some detail. The rate constants for the reaction



have been determined for CO levels  $v = 1-6$  and lower bounds have been provided for the rate constants for levels  $v = 7-12$ . The rate constants for reaction (3),  $v = 4-6$ , as determined in the present analysis, are a factor of 2-3 larger than those determined by Hancock and Smith.<sup>24</sup> The cause for this discrepancy is not clear.

The relative creation rates for CO( $v$ ) production during beam irradiation have also been determined. It has been suggested that this vibrationally excited CO is most probably created through the radiative decay or quenching of excited electronic states of CO which are known<sup>34, 42</sup> to be produced by reaction (26). Although an absolute calibration of the data was not available, it has been crudely (order of magnitude) estimated that one vibrationally excited CO molecule is created per ion pair. Such a production efficiency would imply that  $\sim 3.5$  percent of the electron energy transferred to the gas target is channeled to CO vibrational energy.

The CO<sub>2</sub>( $\nu_3$ ) fluorescence observed in the  $P_{\text{CO}_2} = 1/4$  torr case has also been examined. The dominant CO<sub>2</sub>( $\nu_3$ ) deactivation mechanism for this case is



and the rate constant for this process was determined to be  $1.7 \times 10^{-15} \text{ cm}^3/\text{sec}$  in agreement with previous measurements by Yardley and Moore.<sup>44</sup> The observed CO<sub>2</sub>( $\nu_3$ ) radiation was determined to be severely optically thick. It was found that the transmitted CO<sub>2</sub>( $\nu_3$ ) spectra could be well approximated by an absorption model assuming nonoverlapping doppler broadened absorption lines. Using this model it was crudely estimated that on the average there were  $\sim 4.9$  CO<sub>2</sub>( $\nu_3$ ) excitations per ion pair and that  $\sim 5.5$  percent of the electron energy deposited in the gas target was channeled to CO<sub>2</sub>( $\nu_3$ ) vibrational energy.

It must be stressed that these results are specific to only one set of data, which exhibited rather noisy spectra, and should be confirmed by analysis of additional data sets taken under different experimental conditions. A number of approximate techniques used in the analysis should also be examined in greater detail. For example, the effect of Voigt line shapes on the CO<sub>2</sub>( $\nu_3$ ) band transmission function should be determined and a technique for absolutely calibrating the data should be developed.

## References

1. Cook, F.H., and Murphy, R.E. (1976) A Synchronous Signal Processing Technique for Repetitive Arbitrary Waveforms, AFCRL-TR-76-0035.
2. Murphy, R.E., Cook, F.H., and Sakai, H. (1975) J. Opt. Soc. Amer. 65:600.
3. Rapp, D., and Englander-Golden, P. (1965) J. Chem. Phys. 43:1464.
4. Rapp, D., Englander-Golden, P. and Briglia, D. (1965) J. Chem. Phys. 42:4081.
5. Crowe, A., and McConkey, J.W. (1974) J. Phys. B7:349.
6. Winters, H.F. (1966) J. Chem. Phys. 44:1472.
7. Fehsenfeld, F.C., Schmeltekopf, A.L., Dunkin, D.B., and Ferguson, F.E. (1969) Compilation of Reaction Rate Constants Measured in the ESSA Flowing Afterglow System to August 1969, ESSA Technical Report ERL 135-AL3.
8. Ferguson, E.E. (1973) Atom. Dat. and Nucl. Dat. Tables 12:159.
9. Good, A. (1975) Chem. Rev. 75:561.
10. Berger, M.J., and Seltzer, S.M. (1964) Tables of Energy Losses and Ranges of Electrons and Positrons, NASA SP-3012.
11. Whyte, G.N. (1963) Radiation Res. 18:255.
12. Cohn, A., and Caledonia, G. (1970) J. Appl. Phys. 41:3767.
13. Garvin, D., and Hampson, R.F., editors (1974) Chemical kinetics data survey VII, Tables of Rate and Photochemical Data for Modeling at the Stratosphere (Revised), NBSIR 74-430.
14. Inn, E.C.Y. (1974) J. Chem. Phys. 61:1589.
15. Slanger, T.G., Wood, B.J., and Black, G. (1972) J. Chem. Phys. 57:233.
16. Rawlins, W.T., and Kaufman, F. (1976) J. Chem. Phys. 64:1128.
17. Green, W.H., and Hancock, J.K. (1973) IEEE J. Quantum Electr. QE-9:50.

18. Starr, D.F., Hancock, J.K., and Green, W.H. (1974) J. Chem. Phys. 61: 5421.
19. Zittel, P.F., and Moore, C.B. (1972) Appl. Phys. Letters 21:81.
20. Rosser, W.A., Jr., Sharma, R.D., and Gerry, E.T. (1971) J. Chem. Phys. 54:1196.
21. Stephenson, J.C., and Moore, C.B. (1972) J. Chem. Phys. 56:1295.
22. Miller, D.J., and Millikan, R.C. (1974) Chem. Phys. 6:317.
23. Starr, D.F., and Hancock, J.K. (1975) J. Chem. Phys. 63:4730.
24. Hancock, G., and Smith, I.W.M. (1971) Appl. Opt. 10:1827.
25. Miller, D.J., and Millikan, R.C. (1970) J. Chem. Phys. 53:3384.
26. Center, R.E., and Caledonia, G.E. (1971) Appl. Opt. 10:1795.
27. Schwartz, R.N., Slawsky, Z., and Herzfeld, K.F. (1952) J. Chem. Phys. 20:1591.
28. Liu, Y.S., McFarlane, R.A., and Wolga, G.J. (1975) J. Chem. Phys. 63:228.
29. Fushiki, Y., and Tsuchiya, S. (1974) Jap. J. Appl. Phys. 13:1043.
30. Miller, D.J., and Millikan, R.C. (1974) Chem. Phys. Letters 27:10.
31. Center, R.E. (1973) J. Chem. Phys. 58:5230.
32. Center, R.E. (1970) Phys. Fluids 13:79.
33. Weller, C.S., and Biondi, M.A. (1967) Phys. Rev. Letters 19:59.
34. Gutcheck, R.A., and Zipf, E.C. (1973) J. Geophys. Res. 78:5429.
35. Suhre, D.R., and Verdeyen, J.T. (1976) J. Appl. Phys. 47:4484.
36. Elliot, C.J., and Greene, A.E. (1976) J. Appl. Phys. 47:2946.
37. Herzberg, G. (1951) Molecular Spectra and Molecular Structure I. Spectra of Diatomic Molecules, 2nd edition, D. Van Nostrand Co., New York.
38. Young, L.A., and Eachus, W.J. (1966) J. Chem. Phys. 44:4195.
39. Docking, K.K. (1976) Unpublished results.
40. Schiffner, G., and Klement, E. (1975) Appl. Phys. 6:199.
41. Krupenie, P.H. (1966) The Band Spectrum of Carbon Monoxide, NSRDS-NBS 5.
42. Wauchop, T.S., and Broida, H.P. (1972) J. Chem. Phys. 56:330.
43. Slinger, T.G., and Black, G. (1971) J. Chem. Phys. 55:2164.
44. Yardley, J.T., and Moore, C.B. (1967) J. Chem. Phys. 46:4491.
45. Mitchell, A.C.G., and Zemansky, M.W. (1934) Resonance Radiation and Excited Atoms, Cambridge, London, p. 101.
46. McClatchey, R.A., Benedict, W.S., Clough, S.A., Burch, D.E., Calfee, R.F., Fox, K., Rothman, L.S. and Garing, J.S. (1973) AFCRL Atmospheric Absorption Line Parameters Compilation, A.F.S.C. Report AFCRL-TR-73-0096.
47. Bulos, B.R., and Phelps, A.V. (1976) Phys. Rev. A 14:615.
48. Kumer, J.B., and James, T.C. (1974) J. Geophys. Res. 79:638.
49. Sawada, T., Strickland, D.J., and Green, A.E.S. (1972) J. Geophys. Res. 77:4812.